12-2019

Development of a COMSOL Microdialysis Model, Towards Creation of Microdialysis on a Chip with Improved Geometries and Recovery

Patrick Pysz
University of Arkansas, Fayetteville

Citation

Pysz, P. (2019). Development of a COMSOL Microdialysis Model, Towards Creation of Microdialysis on a Chip with Improved Geometries and Recovery. *Graduate Theses and Dissertations* Retrieved from https://scholarworks.uark.edu/etd/3496

Development of a COMSOL Microdialysis Model, Towards Creation of Microdialysis on a Chip with Improved Geometries and Recovery

A thesis submitted in partial fulfillment
of the requirements for the degree of
Master of Science in Microelectronics-Photonics

by

Patrick Pysz
University of Arkansas
Bachelor of Science in Biochemistry, 2016

December 2019
University of Arkansas

This thesis is approved for recommendation to the Graduate Council.

Julie Stenken, Ph.D.
Thesis Director

Robert Coridan, Ph.D.
Committee Member

D. Keith Roper, Ph.D.
Committee Member

Rick Wise, Ph.D.
Ex-Officio Member

The following signatories attest that all software used in this thesis was legally licensed for use by Patrick Michael Pysz for research purposes and publication.

Mr. Patrick Michael Pysz, Student

Dr. Julie Stenken, Thesis Director

This thesis was submitted to http://www.turnitin.com for plagiarism review by the TurnItIn company’s software. The signatories have examined the report on this thesis that was returned by TurnItIn and attest that, in their opinion, the items highlighted by the software are incidental to common usage and are not plagiarized material.

Dr. Rick Wise, Program Director

Dr. Julie Stenken, Thesis Director

Abstract

Microdialysis (µD) sampling is a diffusion-limited sampling method that has been widely used in different biomedical fields for greater than 35 years. Device calibration for in vivo studies is difficult for current non-steady state analytes of interest correlated with both inflammatory response and microbial signaling molecules (QS); which exist in low ng/mL to pg/mL with molecular weights over a wide range of 170 Da to 70 kDa. The primary performance metric, relative recovery (RR), relating the collected sample to the extracellular space concentration varies from 10% to 60% per analyte even under controlled bench-top conditions. Innovations in microdialysis device design have not deviated or improved upon the commercially-available cylindrical geometry for over 35 years. COMSOL Multiphysics finite element method (FEM) software was used to iteratively model and refine microfluidic-based (µF) µD device designs with the primary focus on optimizing channel geometry for improved RR. The primary focus was to improve fluid to membrane perimeter (P) to fluid cross-sectional area (A) and alter the concentration boundary layer (CBL) using passive µF mixing; which are not possible to fabricate using cylindrical geometries. The current µF µD design uses a simple asymmetric linear-looped (LL) geometry optimized with a P/A of 20 vs. 16.4 for a commercial CMA 20 µD probe with an equal 10 mm length. The simulated LL µF µD achieves a 16.1% relative increase in RR vs. experimental data at a 1.0 µL/min inlet flow rate using a 10 kDa FITC-labeled dextran as the analyte. Mixing was implemented and simulated using a modified herringbone geometry (HBM) and compared to an equivalent linear channel (LC). The HBM is shown to shift the CBL and increase diffusive flux at the membrane-fluid interface resulting in a 16.9 ± 0.7% relative increase in RR for 7 flow rates ranging from 0.125 to 2.0 µL/min vs. the LC. The combination of these changes is shown to increase RR above what is currently

commercially available.

Acknowledgements

To be here today is a strong argument for luck. I am lucky to be surrounded by an exceedingly intelligent group of individuals providing an incredible amount of guidance and interest in my personal success. These individuals have a expressed a vested interest in both my personal and professional development far above anything I deserve. It might be common sense that the company you keep has a profound impact on the events in your life, but the true long-term results of such a fact is blurry at best. The experience graduate school provides has taught me how important it is to be surrounded by people better than you are; and I have been luckily gifted by such an environment. I have learned from everyone in a significant way and become a person I never thought possible. Even at the start of my graduate research career, the idea of achieving a master's degree was unimaginable. Accordingly, and first and foremost, I have been gifted to have Dr. Julie Stenken as an adviser. She saw something in me during her analytical chemistry lecture and gave me the opportunity to work in her lab as an undergraduate researcher the following summer. She has provided me with the opportunity to further my education and earn my master's degree. There is no way to compensate her for the guidance as the experience is invaluable. I look forward to continuing as a Ph.D. student. Working in Dr. Stenken's lab has introduced me to several amazing individuals and I thank the Stenken group for everything they have done. Dr. Randy Espinal Cabrera, thank you for introducing me to the world of microfluidics and mentoring me on continuing your project, which I present here in this thesis. My life would have a very different path otherwise as microfluidics is a strong interest of mine now. Dr. Thaddeus Vasicek, thank you for both your mentorship and friendship. I cannot express the significance of the impact you have had on my development as a person and a researcher. You have guided me and introduced me to new ways of problem solving. Other than Dr.

Stenken, there is no single person with a greater impact on my graduate career. I deeply appreciate and miss our long discussions about everything from research to personal life. You single handedly accelerated my research much further than I could accomplish on my own. Alda Diaz Perez, thank you for being my analytical TA and a great friend. You introduced me to research and helped give me the opportunity to become a graduate researcher. I appreciate our collaboration on many projects and always listening when I needed personal counsel. You encouraged me when I needed it the most. You have listened when I needed it. Victoria Hunter, thank you for being an amazing friend. You have been more than generous with your time and help. I cannot thank you enough for everything you have done over the years. Both you and Alda have treated me like family I consider you both my sisters. Thank you again Dr. Stenken and everyone in the Stenken group. I have progressed further in my life than I ever thought possible thanks to everyone.

Dedication

This Thesis is dedicated to my two beautiful children, Paxton Michael and Lylah Grace. They are the reason I strive to be a better person.

Table of Contents

List of Figures

List of Tables

Variables

Symbol	Description
β	Average Linear Velocity for the Localized Péclet Number
μ	Dynamic Viscosity
ϕ_e	External Sample Medium Volume Fraction
δ	Correction Factor Constant for the Localized Péclet Number
ϕ_m	Membrane Volume Fraction
ρ	Density
$\phi\widetilde{M}_2$	Solvent Dependent Constant by Molecular Weight of Solvent
A	Cross-sectional Area
$C_{\infty ESM}$	External Sample Medium Concentration
C_A	Fluid Cross-sectional Area
C_{inlet}	Inlet Concentration
C_{outlet}	Outlet Concentration
c_{art}	Correction Factor for the Localized Péclet Number
C, C_n	Concentration
C_A	Fluid Cross-sectional Area
c	Concentration
c	Diffusion coefficient for the Localized Péclet Number
D_H	Hydraulic Diameter
D_{aq}	Aqueous Diffusion Coefficient
D_d	Dialysate Diffusion Coefficient
D_e	External Sample Medium Diffusion Coefficient
D_m	Membrane Diffusion Coefficient
D_{meff}	Effective Membrane Diffusion Coefficient
D	Diffusion Coefficient
EE	Extraction Efficiency
g_i	Groove Index
g_o	Groove Offset
g	Groove

H_c	Length of Herringbone Half-cycle
h	Characteristic Length for the Localized Péclet Number
N_i, J	Flux
K_H	Air-liquid Partition Coefficient
k_b	Boltzmann Constant
L_c	Length of Channel
L	Membrane or Channel Length
M_P	Membrane Perimeter from Membrane Surface Area
M_P	Membrane Perimeter
m_a	Mass of Single-Molecule
MR	Mass Recovery
N	Avogadro's Number
Pe_L	Localized Péclet Number
Pe	Péclet Number
p	Pressure
Q	Volumetric Flow Rate
r_h	Hydrodynamic Radius
r_o	Cylindrical Geometry Outer Cannula Radius
R	Reaction Term
RR	Relative Recovery
Re	Reynolds Number
r_α	Cylindrical Geometry Inner Membrane Radius
r_β	Cylindrical Geometry Outer Membrane Radius
t_c	Thickness of Channel
t_g	Thickness of Herringbone Groove
t_m	Thickness of Membrane
T	Temperature
u, U	Linear Velocity
$\bar{V}_1^{0.6}$	Molar Volume
V	Volume

v, v_n	Fluid Linear Velocity
w_c	Channel Width

Abbreviations

μD	Microdialysis (μD)
μF	Microfluidic
APTES	3-aminopropyltriethoxysilane
C4-HSL, AHL-4	N-butyryl-L-Homoserine lactone (C4-HSL, AHL-4)
CBL	Concentration Boundary Layer
DLL	Dual Membrane Linear-Looped
DMAc	N,N-dimethylacetamide
ESM	External Sample Medium
FITC	Fluorescein-isothiocyanate (FITC)
FITC-10	FITC Dextran 10,000 (FITC-10)
FITC-20	FITC Dextran 20,000 (FITC-20)
FITC-4	FITC Dextran 10,000 (FITC-4)
HB	Herringbone
HBM	Herringbone Mixer
IFN-γ	Interferon gamma (IFN-γ)
IL-2	Interleukin 2 (IL-2)
IL-4	Interleukin 4 (IL-4)
IL-5	Interleukin 5 (IL-5)
LC	Linear Channel
LL	Linear-Looped
LL350	Linear-Looped Device with 250 μm inlet and 350 μm outlet
LL450	Linear-Looped Device with 350 μm inlet and 450 μm outlet
MCP-1	Monocyte Chemoattractant Protein 1 (MCP-1)
MO	Methyl Orange (MO)
MWCO	Molecular Weight Cutoff (MWCO)
PDMS	Polydimethylsiloxane
PES	Polyethersulfone
PVP	Polyvinylpyrrolidone
SGM	Single Groove Model
SLL	Single Membrane Linear-Looped

TNF-α	Tumor Necrosis Factor alpha (TNF-α)

Chapter 1. Introduction to Microdialysis Sampling

1.1 Microdialysis Sampling Overview

Microdialysis (μD) is a biological sampling method that is minimally-invasive and used to collect representative samples in situ from a sample medium such as tissue.[1] These samples possess low (ng/mL to pg/mL) concentrations of proteins and other interferents allowing for direct quantitation of the dialysate. Conceptually, the sampling technique is straightforward, consisting of inlet and outlet tubing (Figure 1.1) along with a semi-permeable dialysis membrane with diffusive transport primarily restricted by the manufacturer defined molecular weight cutoff (MWCO) in kDa. The inlet flow (perfusate) moves tangentially to the membrane where the passive-diffusion of analyte is driven by a concentration difference (concentration gradient) between the outer part of the membrane and the fluid passing through the inner part of the membrane lumen. The resulting outlet flow (dialysate) leaves the probe containing a fraction of the targeted analyte concentration relative to the sample medium. The term extraction efficiency (EE) is frequently used to define the performance of microdialysis sampling. Simply, EE is the concentration of analyte in the dialysate relative to the external sample medium (ESM). Equations 1.1 and 1.2 define EE as the ratio of differences in analyte concentration at the inlet (C_{inlet}), outlet (C_{outlet}), and ESM ($C_{\infty ESM}$).[2]

$$EE = \frac{C_{outlet} - C_{inlet}}{C_{\infty ESM} - C_{inlet}} \qquad \text{(Equation 1.1)}$$

$$EE = 1 - \exp\left(-\frac{1}{Q(R_d + R_m + R_e)}\right) \qquad \text{(Equation 1.2)}$$

When C_{inlet} is zero, EE reduces to relative recovery (RR) in Equation 1.3. Bungay et al.

derived EE to reflect the domain dependent mass transport resistances affecting RR during steady-state microdialysis sampling in Equation 1.3.[3] The mass transport resistances are defined for the dialysate (R_d), membrane (R_m), and the external sample medium, or tissue space (R_e), where the volumetric flow rate of the perfusate is Q in µL/min. Each resistance is defined in Equations 1.4, 1.5, and 1.6 where D_d, D_m, and D_e are diffusivities for the dialysate, membrane, and tissue space, respectively.

$$RR\% = \frac{C_{outlet}}{C_{\infty ECM}}(100\%) \qquad \text{(Equation 1.3)}$$

$$R_d = \frac{13(r_\beta - r_\alpha)}{70\pi L r_\beta D_d} \qquad \text{(Equation 1.4)}$$

$$R_m = \frac{\ln{(r_\alpha/r_\beta)}}{2\pi L D_m \phi_m} \qquad \text{(Equation 1.5)}$$

$$R_e = \frac{(K_0/K_1)\Gamma}{2\pi r_0 L D_e \phi_e} \qquad \text{(Equation 1.6)}$$

Radii $r_0,\ r_\alpha$, and r_β are coordinates of domain boundaries relative to the center of a cylindrical µD probe as shown in Figure 1.1. The red and orange arrows represent the diffusive transport across the membrane. The blue arrows represent the fluid as it passes down the inlet cannula and up along the inner lumen of the membrane and exits. L is the membrane length, and ϕ_m, and ϕ_e are the volume fractions available for diffusion in the membrane and external sample medium, respectively.

In Equation 1.6, K_0 and K_1 are Bessel functions, and Γ is a composite function representing rate constants for analyte generation and uptake kinetics in the external sample medium.[4] For this research, the focus is applied to altering R_d and R_m which are directly related to device design. The extracellular space resistance (R_e) is analyte- and tissue-dependent and cannot be altered (or is fixed in value). For this thesis, RR will be used as the primary performance metric as the sample medium ($C_{\infty ECM}$) resistance is not considered, and there is no C_{inlet}.

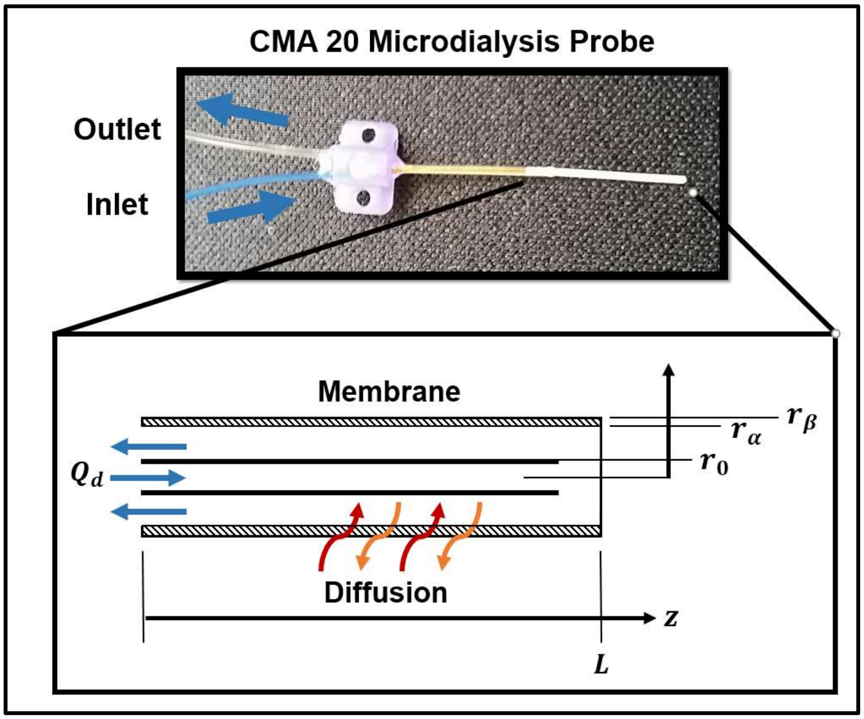

Figure 1.1. Depiction of a CMA 20 Microdialysis Probe with zoomed geometric representation of length scale variables from Equations 1.4, 1.5, and 1.6.

1.2 Microdialysis Calibration and Sampling Challenges

In vivo µD calibration presents a difficult problem due to diffusion-limited transport and the complex processes that affect analyte equilibria within the tissue space. In vitro comparisons, where the sample medium concentration is known, cannot be used to determine the concentrations in vivo, and tissue or tissue conditions cannot easily be replicated in vitro.

Common methods for calibrating μD in vivo include no net flux, variable flow rate, and internal standards.[2] While calibration cannot be eliminated, the requirement can be reduced by increasing RR as the dialysate collected would more closely match the sample medium. Each method attempts to create a reference point in which $C_{\infty ECM}$ can be determined.

1.2.1 No-net flux

No-net flux is a technique used to determine an unknown concentration of a sample by perfusing a C_{inlet} of higher and lower concentrations. The resulting difference from the C_{inlet} and C_{oulet} is plotted versus C_{inlet}). Figure 1.2 A shows a conceptual graph of the no-net flux method for determination of equilibrium sample medium concentration. Figure 1.2 B conceptual graph of the no-net flux method being applied under non-steady-state conditions. The red circles represent measurements where concentrations were perfused (C_{inlet}). In graph A, the blue diamond represents the concentration external to the probe ($C_{\infty ECM}$ = 100 μM) as determined by the linear plot due to steady-state conditions. Graph B depicts how each known concentration is actually variable in comparison with the perfused concentrations due to non-steady-state conditions. Here, the blue diamonds also represent $C_{\infty ECM}$, but there is no linear relationship as the analyte is not steady-state.

In order for this plot to be linear, the analyte being measured must have a steady-state concentration (concentration does not change over time). However, analytes such as cytokines, signaling proteins linked to inflammatory response, never reach this steady-state, as they readily bind with other proteins in the sample medium.[5,6] Accordingly, perfusion of cytokines will shift the sample medium concentration and void calibration causing unknown changes or unwanted biological effects to local. Figure 1.2 B conceptually depicts how the resulting difference in

C_{inlet} and C_{oulet} when perfusing a cytokine can cause a time-dependent and inflammation-dependent change in concentration.

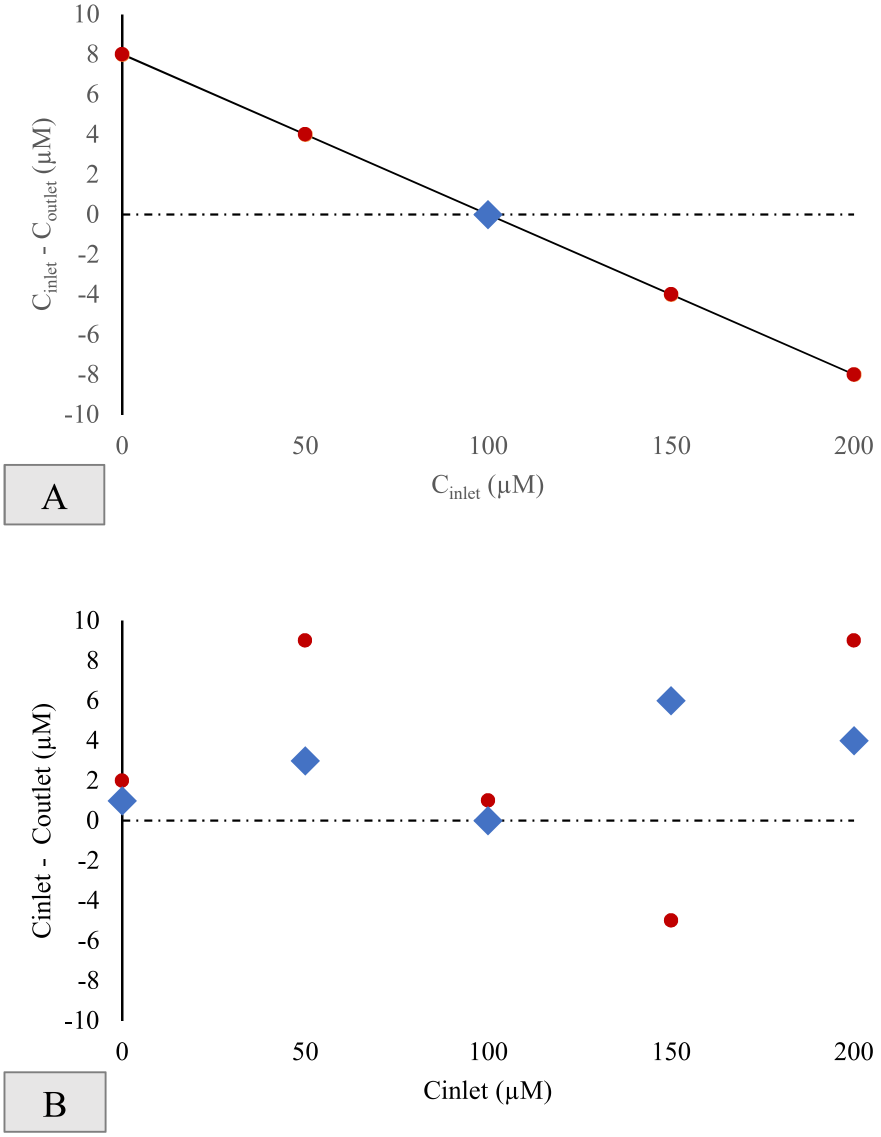

Figure 1.2. Conceptual comparison of the no-net flux method under steady-state (A) and non-steady-state conditions (B).

1.2.2 Multiple Flow Rates Approach to Zero Flow

The multiple flow rates method uses experimentally determined RR data for a range of flow rates to predict RR outside of this range using Equation 1.2. There are two downsides to this method. The first, variable flow rate requires a considerable amount of time due to the need for multiple flow rates and additional analysis time for each sample. For example, the calibration using a five-point curve requires five different flow rates. Using a sample volume requirement of 50 μL for a detection assay, and perfusing at 0.5, 1.0, 2.0, 3.0, and 4.0 μL/min, then 4 hours 44 minutes is needed to calibrate. The second, for any molecule that does not reach steady-state, the collection exhibits the same calibration problem discussed in Section 1.2.1 with the no-net flux method. Figure 1.3 plots the predicted RR vs. Q for methyl orange (MO), Fluorescein-isothiocyanate dextran 10,000 (FITC-10), and monocyte chemoattractant protein 1 (MCP-1) using the multiple flow rates method.

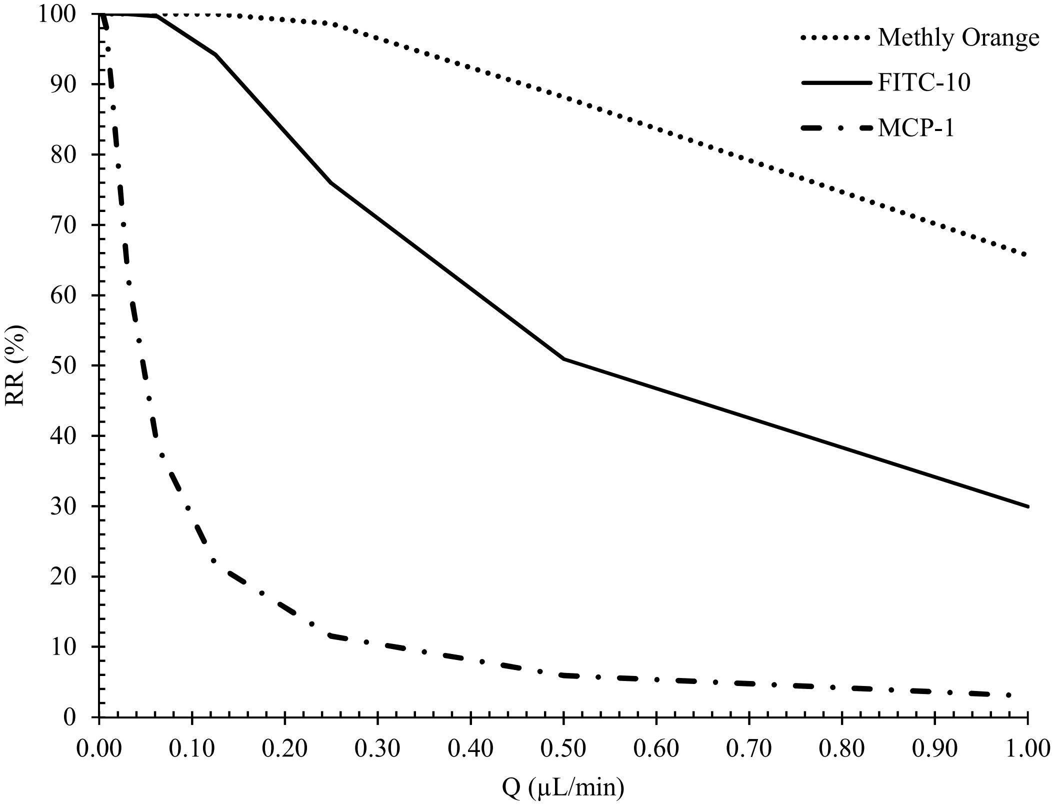

Figure 1.3. Projected RR using multiple flow rates method.

The effects of different D_{aq} and D_m can be seen as the flow rate increases. Notably, MCP-1 has a high membrane resistance quantified by a slow $D_m = 2.17 \cdot 10^{-7}$ cm^2/s while MO and FITC-10 are both faster with D_m equal to $6.7 \cdot 10^{-7}$ cm^2/s to $2.5 \cdot 10^{-7}$ cm^2/s, respectively. The RR data in Figure 1.3 was obtained using Equation 1.2 and setting R_e to zero. As flow rate decreased, RR increased to a maximum at 100% giving a reverse sigmoidal shaped function. The calculation-based specifics of this method will be discussed in Section 2.2 where it was used to obtain the membrane diffusivity D_m from experimental and theoretical data for use in simulations.

1.2.3 Internal Standards

The use of an internal standard involves a delivery-based method where C_{inlet} from Equation 1.1 is a known quantity along with the mass transfer properties of the device. [2,7–10] The internal standard is perfused from the inlet and the differences in concentration are measured at the outlet. Ideally, the internal standard has mass transfer properties identical to the analyte being studied, allowing the assumption that the analyte lost is proportional to the analyte gained. Consequently, the use of isotope-labeled analytes is preferable.

1.3 Enhancing Relative Recovery

Affinity agents, vacuum ultrafiltration, and open-flow devices have been used to increase analyte RR or decrease the mass transport resistance caused by the device membrane. Affinity agents increase the concentration gradient, vacuum ultrafiltration or push-pull devices add fluid advection across the membrane to assist diffusion, and open flow devices operate similarly to push-pull devices, but remove the membrane entirely allowing for direct sampling of the external sample medium.

1.3.1 Affinity Agents

One of the primary methods of enhancing RR in this research was altering the concentration boundary layer. The simplest form of Flux J is given by Equation 1.7 where the concentration gradient is defined as the concentration difference from C_0 to C_1 over a distance l governed by the diffusivity D. If C_0 is considered to be the concentration external to the probe, and C_1 the concentration inside the probe, then decreasing C_1 will increase J and ultimately RR as the diffusive flux through the membrane will be higher.

$$J = \frac{D}{l}(C_0 - \mathrm{C}_1) \qquad \text{(Equation 1.7)}$$

In the Stenken group, affinity agents have been used to alter the concentration gradient as governed by Equation 1.7 to collect cytokines. Affinity agents work by binding an analyte and decreasing C_1. There are different types of affinity agents from different modified beads,[11] nanoparticles,[12] antibody-coated microspheres,[13] cyclodextrins,[14] and device surface modifications.[15]

1.3.2 Push-Pull and Vacuum Ultrafiltration

Figure 1.4 gives graphical depictions of push (A), push-pull (B), and pull (C) microdialysis sampling methods. The red and blue arrows represent diffusion, and the green arrows represent advective flux at the membrane surface (dashed line). The gray arrows are the inlet and outlet advection vectors. The size and quantity of the arrows presents a qualitative representation of the typical magnitude of these vectors for in vitro experiments using a CMA 20 μD probe. Push-pull μD (Figure 1.4 B) is when a pressure differential is applied to the inlet and outlet of the probe using the normal inlet pump with the addition of a vacuum pump at the outlet.

This allows for tuning of the transmembrane pressure and, consequently, can control fluid flow across membrane bidirectionally. This method is required in commercial devices for µD probes with MWCOs that are greater than 1 million Da (1 MDa) as the pores are naturally larger to allow for larger molecules to pass and, without a vacuum source at the outlet, there would be significant inlet fluid loss through the membrane with no dialysate collected. Vacuum ultrafiltration (Pull) (Figure 1.4 C) is similar except there is no inlet flow source, and fluid is pulled through the membrane (ultrafiltrate). This method cannot be used in vivo as the fluid available for collection is not replenished quickly enough (data not shown).

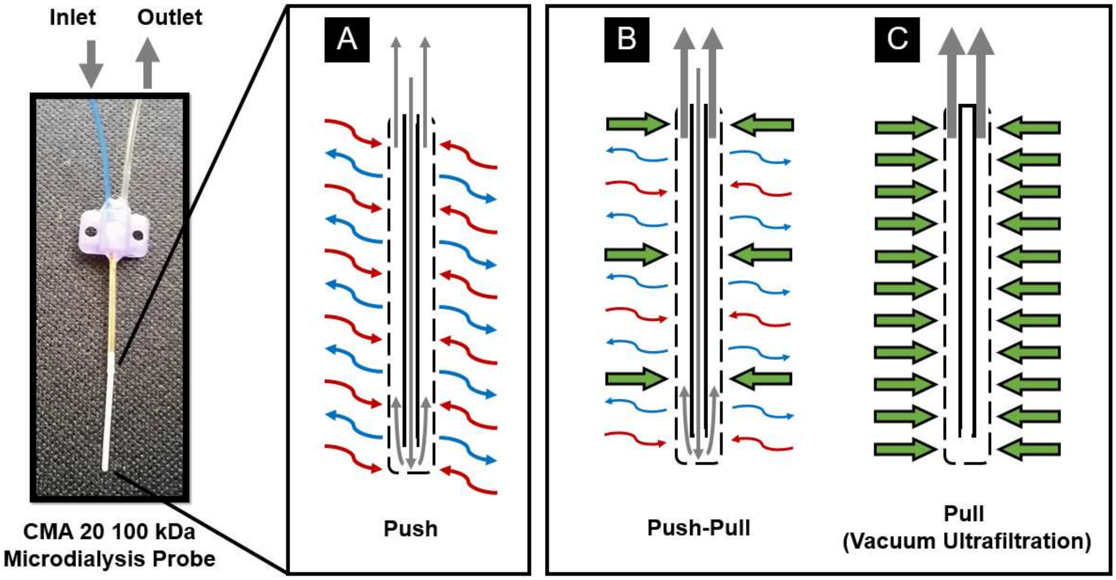

Figure 1.4. Visual comparison of diffusion and flow vectors for Push (A), Push-Pull (B), and Pull (C) µD sampling methods.

1.3.3 Open-Flow Devices

Open flow devices have incorporated aspects of push-pull and pull methods have been explored by both Shippy[16,17] and Kennedy[18] groups, but in-vivo flow rates are limited to 50 nL/min. This limits the sample size and lowers the temporal resolution by 20x for cytokine detection assays used in the Stenken lab where the minimum sample size is 50 µL and typically collected at 1.0 µL/min in vivo. Open flow devices involve two capillaries acting as an inlet to deliver fluid and outlet pulling fluid from the sample medium, respectively. There is no membrane in these devices removing any molecular weight restrictions. Again, the main disadvantage is the flow 50 nL/min flow rate which is caused by the inability of the tissue to replenish fluid. This is also the main disadvantage for using commercial µD probes in a push-pull configuration.

1.4 Short Introduction to Microfluidics

Microfluidics consists of microfabricated devices used to manipulate fluid on the scale of 1 µm to 1000 µm (characteristic lengths). At these length scales, fluid tends to behave as if it is weightless (effectively momentum-less, low-inertia). This relationship is given by the Reynolds number (Re) in Equation 1.8; where the product of the density ρ, average velocity U, and characteristic length L is taken as a ratio with the fluid viscosity μ.

$$Re = \frac{\rho U L}{\mu} \qquad \text{(Equation 1.8)}$$

This can be considered a ratio of momentum diffusion over viscous diffusion. In microfluidic devices, Re is typically less than 100 with many devices closer to 1. Flow is considered laminar for $Re < 2300$. Laminar flow consists of a parabolic velocity profile without any turbulent properties (vortexing). The dominance of viscosity and low fluid momentum allows fluid flows to move and conform to channel shapes instantaneously without altering the velocity profile from its parabolic nature. Imagine the table cloth magic trick pulling the cup of water with it, and the cup of water remaining undisturbed and on the same position on the table cloth in the end.

There are other gradient/force ratios (non-dimensional numbers) to consider in microfluidics, but the Reynolds number is the most prevalent in describing the impact of forces for small (micrometer scale) systems.[19–21] In this research, the Péclet number (Pe) is also important as it describes the ratio or competition of linear velocity and diffusivity D over a characteristic length as given in Equation 1.9.

$$Pe = \frac{UL}{D} \qquad \text{(Equation 1.9)}$$

A secondary, but not lesser, concept to understand is that microfluidic devices have high surface area to volume ratios. This increases the amount of surface tension forces. While a bucket of water will spill out everywhere if the bucket is removed. A single raindrop will hold its shape.

Microfluidics presents unique solutions to complex problems such as limited sample sizes/volumes, or the possibility of small-scale, low-cost portable devices that can be used in the field. The entire field of microfluidics fabrication piggy backs on the semiconductor revolution with the use of photolithography techniques for fabrication with the first microfluidic device made in 1989.[22]

These fabrication tools are highly refined, ubiquitously used to mass produce products used in daily life, and can allow for fast high-volume production of microfluidic designs. Mark and Sackmann et al. stated microfluidics advantages to be portability, throughput, cost, disposable, variety of analysis for a single sample, low reagent consumption, high functionality, precise, and programmable (Table 1.1).[23,24]

The cornerstone of microfluidics is to manipulate molecules and their containing fluids towards an end goal. At the small volumes (µL to pL) and dilute concentrations encountered (µM to fM) in microfluidics, limitations can be reached where there is not enough analyte to satisfy the detection limits of available assays.[25] However, given enough time and sample volume, the required number of molecules can be collected. The solution then is to preconcentrate the collected volume to obtain the required concentrations.

Table 1.1. Examples of applications and fields in microfluidics.

In-vitro diagnostics	Ecology
Point-of-care testing	Agriculture
Drug discovery	Homeland security
Massively parallel analysis	Cellular assays
Biotechnology	Biosynthesis

Common variables and themes in microfluidics (µF) will be discussed in detail throughout this thesis. Most importantly, Chapter 3 and Chapter 4 will discuss the importance of characteristic lengths, rates, boundary layers, and optimizing device geometry towards controlling the effects of these concepts.

1.5 Thesis Research Flow and Goals

The goal of this research was the design and fabrication of a microfluidic (µF) microdialysis device capable of improved RR in attempt improve µD calibration as discussed previously in Section 1.2. It was known that such a task would require multiple revisions at different development stages in order to arrive at a device with the desired specifications. The basic process included a design, simulation, fabrication, and characterization steps (Figure 1.5). Both the simulation and characterization steps could result in revision steps reverting the process back to the design stage of development where the data obtained was examined toward improving device performance.

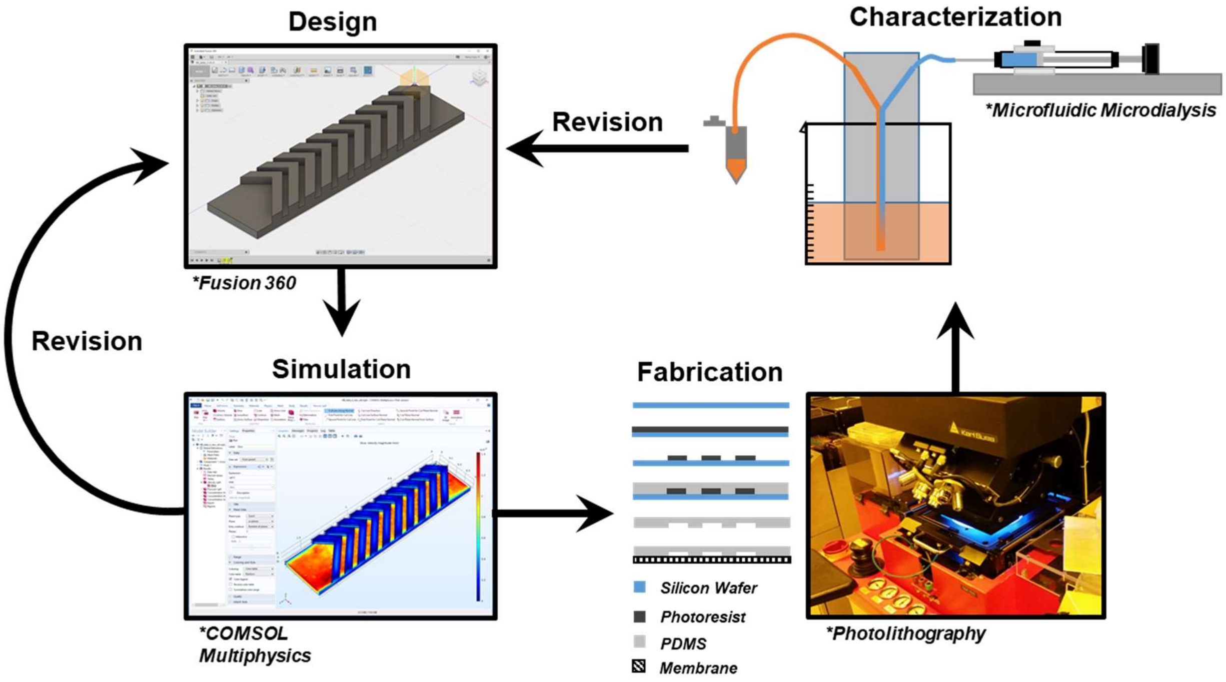

Figure 1.5. Depiction of process flow used to complete this research. Fusion 360 is a 3D CAD program produced by AutoCAD. COMSOL Multiphysics is a partial differential equations solver program.

It should be noted that the ultimate goal of this project did not include optimizing the device geometry and materials for use in vivo. The focus was demonstrating the potential efficacy of increasing diffusive transport with appropriate mathematical modeling. Final device fabrication and material methods were considered future work. The primary focus of this research was the alteration of device geometry from the common cylindrical geometries available commercially. These cylindrical geometries did not differ from each other in any way other than changes to radii (r_o, r_B, and r_a in Figure 1.1).

The membranes of these devices are fabricated using extrusion phase inversion, and devices are assembled using commonly available tubing.[26] Fabrication of unique cylindrical geometries with sub 100-micron sized features is difficult. Accordingly, soft-lithography presents a simple and readily available fabrication process which allows for the fabrication of novel geometries using a layer-by-layer approach that is well defined and ubiquitous in the Lab-on-a-Chip and μF community.[27–29] Soft-lithography uses tools pioneered by the microchip industry, but is limited to Cartesian-based channels. This research shows comparisons of cylindrical, simple Cartesian, complex Cartesian geometries in effort to increase RR compared to commercial devices.

Ultimately, in mass transport terms, RR is a function of the concentration gradient with can be altered using different μF geometries. Many microfluidic devices do this already in which research was motivated due to the non-turbulent non-mixing properties of fluids on a micron-scale by rotating and folding fluids.[30–33] One geometry of interest is known as the herringbone mixer which continuously rotates and folds fluid in on itself in a spiral as it moves down the length of the μF channel.[34–38] The advantage of herringbone geometry is the ability to sweep diffusing molecules away from the membrane in μF μD device, therefore increasing the concentration gradient and RR; this process is also known as collapsing the concentration gradient. Due to the complexity of the geometry and fluid flow, there is no analytical solution for predicting device performance with complex geometries. COMSOL Multiphysics simulation software (Burlington, MA) allows for the modeling and prediction of RR for these complex geometries. It also allows the user to visualize different gradients toward understanding how a system works when it would otherwise be impossible experimentally. COMSOL also allows for rapid iterative design changes without investing in physical fabrication and characterization.

Chapter 2 will give and overview of COMSOL along with experimental vs. simulated RR for commercial μD devices. Chapter 3 will discuss design and optimization of a μF-based μD device to include important mass transport variables and considerations from a geometry only perspective. Chapter 4 will overview the fabrication and characterization of optimized linear-looped μF μD devices. Chapter 5 will discuss herringbone-based μF μD geometries with included COMSOL simulations.

Chapter 2. COMSOL Simulation of Commercial Microdialysis Devices

2.1 Introduction to COMSOL Multiphysics Software

COMSOL simulations of commercial microdialysis devices were developed and compared with experimental data. The short-term goal was to provide a baseline simulated physics implementation which could be geometrically modified toward improving RR using a microfluidic platform. COMSOL's advantage is the ability to develop a fully functional mathematical representation of a physical system without the need for repetitive and high cost fabrication and time-consuming characterization steps. This allows for multiple design iterations to be completed at a significantly lower cost. COMSOL promotes this ability using Application Builder functionality which wraps a prebuilt COMSOL simulation in an app format allowing the user to change variables and see simulation results without having to edit the model directly.[39]

COMSOL Multiphysics is a software program capable of numerically solving partial differential equations using the Finite Element Method (FEM); otherwise known as Finite Element Analysis (FEA). COMSOL allows for complex physics models to be solved in cases where the analytical solution is either impossible or does not have a numerical solution currently. COMSOL's primary strength as an FEA solver is the ability to couple multiple types of physics into a single simulation. Examples include combinations of advection, diffusion, porous media flow, heat transfer, chemical reactions and kinetics, fluid-structure interactions, electrochemistry, and many more which can be found on the COMSOL website. When the desired physics subset is not predefined, COMSOL offers the ability to implement new physics based on the types using a templating method; which uses predefined forms of differential equations that COMSOL can solve. Each of these physics types is editable through what are called modules.

COMSOL organizes each simulation into what is called the model tree. This is split into four sections: global definitions, components, studies, and results. The global definitions contain a user-defined parameter list which can contain various constants and equations; along with a material list containing both built-in and user-definable material properties. All global definition values can be referenced in all other sections of the model tree. This is incredibly powerful as it allows for the change of a single parameter to automatically affect multiple parts of a model. It also can prevent user error in the sense that the same value might be repeated several times throughout the model and editing this value, if not in the parameter list, can easily result in user error if one is missed.

The component section consists of the geometry, physics, and mesh. Here, the user can build the physical layout of the model and choose the types of physics or even define physics that present into COMSOL. The study section consists of settings for COMSOL's FEA solver where you can choose to split the solving process into multiple steps, set the level of error tolerance, or choose different solvers based on available computational resources. Additionally, the study section gives the ability to perform a parametric sweep where you can list ranges of geometry variables, initial conditions, and boundary conditions for which COMSOL will automatically attempt to solve for all versions of the model. The results section contains multiple forms of data processing abilities to include multidimensional graphing, calculations, animations, and coordinate-based data selection tools.

Each domain is described by built-in physics types of Laminar Flow and Transport of Dilute Species. COMSOL simultaneously solves the stationary incompressible form of the Naiver-Stokes and mass conservation equations (Equations 2.1 and 2.2) for Laminar Flow physics, and the advection-diffusion and mass conservation equations (Equations 2.3 and 2.4) for

Transport of Dilute Species physics.

$$\rho(u \cdot \nabla)u = \nabla \cdot [-pI + \mu(\nabla u + (\nabla u)^T] + F$$ (Equation 2.1)

$$\rho\nabla \cdot (u) = 0$$ (Equation 2.2)

$$N_i = -D_i\nabla \mathrm{c_i} + c_i u$$ (Equation 2.3)

$$\nabla \cdot (-D_i\nabla \mathrm{c_i}) + u \cdot \nabla c_i = R_i$$ (Equation 2.4)

For Equations 2.1 and 2.2, ρ is the density, u is the linear velocity along a streamline, p is the pressure, μ is the dynamic viscosity, T is the temperature, and F is the external force applied to the fluid. For Equations 2.3 and 2.4, N_i is the diffusive flux, D_i is the diffusion coefficient, c_i is the concentration, and R_i is a reaction term. Figure 2.1 depicts the boundary and domain conditions governed by Equations 2.1, 2.2, 2.3, and 2.4 as follows.

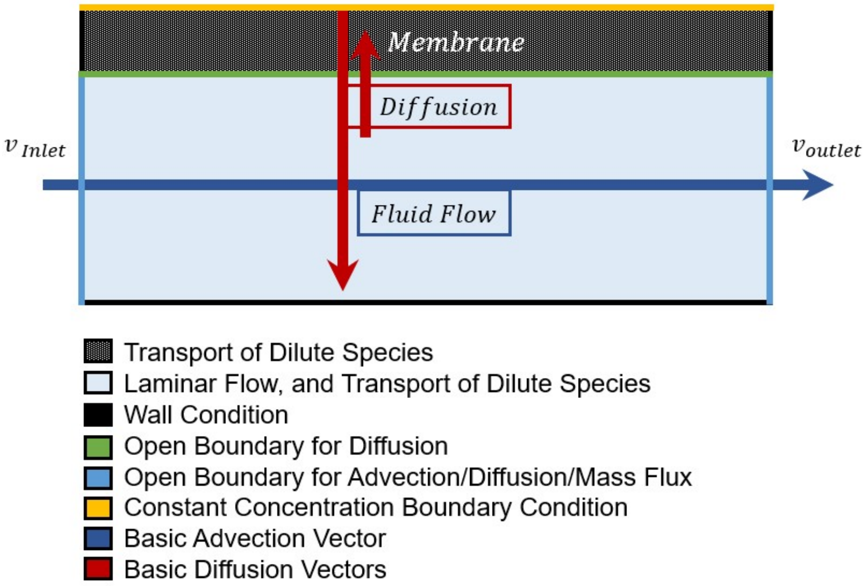

Figure 2.1. Basic physics domains, boundary conditions, and domains for all COMSOL models used in this research.

The yellow line is a constant concentration source boundary condition. This is used to represent a pseudo-infinitely large sample medium which is being stirred, and as a result the analyte mass available for diffusion into the device is never depleted. This is equivalent to setting the length term L in R_e (Equation 1.6) to infinite making R_e= 0, mathematically. The white and black dashed region represents the microdialysis membrane where analyte diffusion is allowed to occur, but fluid flux through the pores is assumed to be zero. The green line is an open boundary for diffusion only preventing fluid flux as previously described. The red lines across the green diffusion boundary represent the assumed magnitude of diffusion in both directions. The light blue domain allows for both diffusion and laminar flow. The dark blue lines are the inlet and outlet conditions for laminar flow.

2.2 Model Constants for both 2D Axisymmetric and 3D CMA 20 and CMA 12 Models

Modeling any device requires a full description of geometry and a full understanding of how the device works. This includes all characteristic lengths, rates, and boundary conditions. Table 2.1 gives the general model constants used for the CMA 20 and CMA 12 µD probe models. The diffusion coefficients are generic and are set on an analyte by analyte basis. Aqueous and membrane diffusion coefficients are given in Section 2.2.1 along with their determination methods and sources. The radii r_o, r_B, and r_a and membrane length L_m differ in Table 2.1 depending on device model (CMA 20 or CMA 12) as described in Table 2.2. Standard values of water for density ρ, and dynamic viscosity μ at 25 °C were used (Table 2.1).[40] Temperature was not altered from standard conditions, but it is known that for any in vivo simulation, there would be an assumed value of 37 °C and all diffusivities would increase according to Equation 2.5 and 2.6 given later in Section 2.2.1, the Stokes-Einstein and Wilke-Chang equations, respectively. All CMA models in this research used an additional geometry variable that is in COMSOL only, Lpostm.

Table 2.1. CMA microdialysis probe constants used in their respective COMSOL models.

Variable	COMSOL Parameter	Value [units]	Description
D_d	Dd	1e-6 [cm^2/s]	Dialysate Diffusivity (Placeholder)*
D_m	Dm	1e-6 [cm^2/s]	Membrane Diffusivity (Placeholder)*
r_o	r0	250 [µm]	Outer Membrane Radius**
r_b	rb	200 [µm]	Inner Membrane Radius**
r_a	ra	125 [um]	Outer Cannula Radius**
r_m	rm	r0-rb	Thickness Membrane**
r_c	rc	50 [um]	Inner Cannula Radius
Q	Q	0.5e-6 [L/min]	Volumetric Flow Rate (Placeholder)*
L_m	Lm	10 [mm]	Length Membrane
NA	Lpostm	1000 [um]	Length of channel after membrane
ρ	rho	1000 [kg/m^3]	Water Density
μ	mu	8.9e-4 [Pa*s]	Dynamic Viscosity of Water
C_{esm}	Cesm	100e-6 [M]	Sample Medium Concentration

*These values will change when parametrically sweeping the model in COMSOL.
**Values only apply to the CMA 20 100 kDa µD probe.

Table 2.2. Individual CMA microdialysis probe constants.

Geometry Constant	COMSOL Parameter	CMA 20 (2015, 2016-2018)	CMA 20 (2006)	CMA 12*
r_a (μm)	ra	175	175	125
r_b (μm)	rb	200	210	200
r_0 (μm)	r0	250	250	250
L_m (mm)	Lm	10	10	4

*The CMA 12 probe consists of different inner cannula geometry later defined in Section 2.2.

This variable simply describes a length extension of the fluid flow channel only past the membrane (no membrane boundary condition exists in this section of the channel). This was done as initial simulations (not shown) gave RR results inconsistent with experimental data and sometimes even negative, suggesting COMSOL solver encountered a discontinuity. Extending the end of the channel past the membrane resolved this problem giving consistent RR. All of these variables could be altered as constants on-demand using COMSOL's parametric sweep feature previously discussed in Section 2.1. Accordingly, Q is typically swept for RR between 0.5 and 5.0 μL/min for CMA μD devices.

2.2.1 Aqueous Diffusion Coefficient Calculation Methods

The aqueous diffusion coefficient (D_{aq}) of small molecules (dilute solutes) with radii five times larger than the solvent (buffered water for this research) could be estimated using the Stokes-Einstein relationship in Equation 2.5 below.[20] When the analyte was similar in size to the solvent, water, then the Wilke-Chang Equation 2.6 was used.[20,41] For this research, Equation 2.7 applied as the generic diffusion coefficient D is equal to both the dialysate D_d and aqueous D_{aq} diffusion coefficients.

$$D_{aq} = \frac{k_b T}{6\pi\mu r_h} \qquad \text{(Equation 2.5)}$$

$$D_{aq} = \frac{7.4 * 10^{-8}(\phi \widetilde{M}_2)T}{\mu \bar{V}_1^{0.6}} \qquad \text{(Equation 2.6)}$$

$$D = D_d = D_{aq} \qquad \text{(Equation 2.7)}$$

Equation 2.5 is defined by the following variables: the Boltzmann constant (k_b), temperature (T), dynamic viscosity (μ) of the fluid for which the analyte is diffusion, and hydrodynamic radius (r_h). The Stokes-Einstein relationship contains friction terms $6\pi\mu r_h$ showing how the radius of the molecule and solution viscosity decrease the diffusion coefficient for larger molecules. The primary limitation is that molecules in increasing sizes are not always spherical (analogous to a smart car vs. freight truck aerodynamically). For the purposes of this research, Equation 2.5 was used to estimate D unless a measured literature value is given.

In the event that r_h was not available, a calculation using Equation 2.11 with density ρ, molecular weight MW, and the equation for volume of a sphere could be used to estimate r_h. The volume of a sphere, Equation 2.8 is rearranged into Equation 2.11 solving for $r = r_h$. This was accomplished by obtaining the mass m_a of a single molecule from the MW, and Avogadro's number N in Equation 2.9; which was plugged into Equation 2.11 along with the density ρ in the form of Equation 2.10 and finally substituted into Equation 2.11. Table 2.3 lists all aqueous diffusion coefficients and corresponding sources.

$$V = \frac{4}{3}\pi r^3 \qquad \text{(Equation 2.8)}$$

$$m_a = \frac{\text{MW}}{N} \qquad \text{(Equation 2.9)}$$

$$V = \frac{m_a}{\rho} \qquad \text{(Equation 2.10)}$$

$$r_h = r = \left(\frac{3}{4\pi}V\right)^{\frac{1}{3}} = \left(\frac{3}{4\pi}\frac{m_a}{\rho}\right)^{\frac{1}{3}} \qquad \text{(Equation 2.11)}$$

Table 2.3. Aqueous diffusion coefficients.

Analyte	Abbreviation	MW (Da)	r_h (Å)	r_h Source	D_d (10^{-6} cm^2/s)	D_d Source
Model/Test Analytes						
Methyl Orange	MO	327.33			6.87	❋
			4.45	†	3.43	❋
Vitamin B-12 (Cobalamin)	B-12	1360			4.11	Stenken[42]
Caffeine		194.19			7.04	Niesner[40]

Table 2.3. (Cont.)

Analyte	Abbreviation	MW (Da)	r_h (Å)	r_h Source	D_d (10^{-6} cm^2/s)	D_d Source
Quorum Sensing/Biofilm						
N-butyryl-L-Homoserine lactone	C4-HSL	171.2		†	6.15	
Cytokines						
Monocyte Chemoattractant Protein 1	MCP-1				1.15	
Tumor Necrosis Factor alpha	TNF-α				0.82	Xiaoping[43]
Interferon gamma	IFN-γ				0.82	Xiaoping[43]
Interleukin 5	IL-5				0.94	Xiaoping[43]
Interleukin 4	IL-4				1.23	Xiaoping[43]
Interleukin 2	IL-2				0.96	Xiaoping[43]
Dextran						
Dextran 4,000	FITC-4	4000	14	Sigma	1.97	⁕
					1.20	
Dextran 10,000	FITC-10	10,000	29 ± 7	††	0.75 ± 0.03	Arrio-Dupont[44]
			23		13 +/- 4	Ross[45]
					0.14	Ross[45]
			23	Sigma	1.69	⁕
Dextran 20,000	FITC-20	20,000	29 ± 1	††	0.64 ± 0.02	Arrio-Dupont[44]
			33	Sigma	0.94	⁕
					1.01	
Dextran 40,000	FITC-40	40,000	49 ± 6	††	0.44 ± 0.05	Arrio-Dupont[44]
			45		0.074 ± 0.03	Ross[45]
					0.07	Ross[45]
			45	Sigma	0.61	⁕
Dextran 70,000	FITC-70	70,000	60	Sigma	0.46	⁕
Dextran 150,000	FITC-150	150,000	85	Sigma	0.32	⁕

† r_h determined using MW and ρ in Equation 2.8, 2.11, and then Equation 2.5

†† r_h determined using D_d and Equation 2.5

⁕ D_d determined using r_h and Equation 2.5

2.2.2 Membrane Diffusion Coefficient Determination

As previously described in Section 2.2, the membrane diffusion coefficient D_m is required to model µD probes. D_m is similar to a mass transport coefficient in the sense that it is an average rate, but over a domain (membrane) and not a system such as multiple devices in series as the performance of the system can be measured, but not the individual devices.[46] However, the two constants can be used interchangeably depending on the mathematical requirement. Determining the D_m for a µD device requires an in vitro where flow rate is varied and RR is measured under stirred conditions. The analyte aqueous diffusivity D_{aq} is required along with Equations 1.4, 1.5, 2.12, and 2.13. Equation 2.12 are the sum of all mass transport resistances R_d, R_m, and R_e in the µD probe. Equation 2.13 is derived from Equation 1.2 under stirred conditions to create a constant concentration at the surface of the membrane by setting R_e = 0 and making D_m the only unknown. The required D_{aq} can be determined through calculations using Equations 2.5 and 2.6 or referenced from literature.

$$R_t = R_d + R_m + R_e \qquad \text{(Equation 2.12)}$$

$$\ln(1 - RR) = \frac{1}{R_t}\frac{1}{Q} \qquad \text{(Equation 2.13)}$$

Equation 2.1 is plotted with the left-hand-side on the y-axis and right-hand-side on the x-axis where R_t^{-1} is the slope; otherwise known as the permeability of the µD probe in units s·cm^{-3}. The permeability here should not be confused with the fluid permeability of units m^{3}cm^{-3} commonly used in membrane fabrication and characterization literature to describe resistance to fluid movement (usually water) through a membrane or other porous media as originally described by Darcy.[20] It should be noted that if the experiment is done quiescently (not stirred), then the D_m obtained from 2.13 will account for the mass transport resistance given by R_e. The resulting COMSOL model will give corresponding RR results and, subsequently, the D_m behaves like a mass transport coefficient. Table 2.4 gives both aqueous and membrane diffusion coefficient along with sources used for modeling CMA µD devices. All D_m in Table 2.4 were calculated using experimental RR and 2.13. All D_d were calculated using the Stokes-Einstein equation from the hydrodynamic radius r_h, obtained from literature, or calculated based on molecular weight as described in Section 2.2.1. Specific values used to calculate D_d were given previously in Table 2.3.

Table 2.4. Aqueous and membrane diffusion coefficients.

Analyte	D_d 10^{-6} cm^2/s	D_m 10^{-7} cm^2/s	CMA Probe (Year)
MO	6.870	6.71	20 (2016-2018)
		4.48	20 (2016-2018)
		4.55	20 (2016-2018)
C4-HSL	6.160	5.04	20 (2016-2018)
FITC-4	1.970	14.80	20 (2016-2018)
FITC-10	0.750	2.55	20 (2015)
		1.31	20 (2016-2018)
	1.200	1.65	12 (2015)
FITC-20	1.010	1.56	20 (2016-2018)
MCP-1	1.150	0.217	20 (2016-2018)
MCP-1*		0.179	20 (2016-2018)
TNF-α	0.820	0.282	20 (2006)
IFN-γ	0.823	0.0522	20 (2006)
IL-5	0.939	0.0273	20 (2006)
IL-4	1.230	0.465	20 (2006)
IL-2	0.956	0.150	20 (2006)
B-12	4.110	3.00	20 (2016-2018)

*Probe had Vibrio Harvey Biofilm

2.3 General CMA Device Model Simplifications and Assumptions

Physically, the CMA 20 and CMA 12 both contain an inner-cannula with different designs. The CMA 20 uses a polyurethane needle as the inner-cannula that extends into a glue tip at the base of the membrane. The needle is chamfered at a 45-degree angle to a point where some of the tubing outlet is available for fluid flow. The exact outlet diameter exposed is unknown and will vary between devices as each cannula is manually inserted into the probe according to the manufacturer. Considering that the flow rate is volumetric, the linear velocity at any point in the probe is governed by the cross-sectional area, and the linear velocity inside the inner-cannula and at the base of the inner-cannula does not affect the linear velocity in the annulus where diffusion is occurring. Accordingly, the radial model was simplified to just a flat tube (Figure 2.2). The distance from the tip of the inner-cannula was assumed to be the same as the annulus depth or 75 µm. Lower distances were initially simulated with no difference in RR found (not shown). The CMA 12 uses a steel needle that extends to the probe glue tip but has a laser-drilled hole at an arbitrary point towards the end of the membrane.

This results in two outlets from the inner-cannula to the annulus for fluid flow. Using the same volumetric flow rate to linear velocity relationship, the diameter of the laser-drilled hole is only relevant to not exceed the diameter of the inner cannula itself and does not affect the linear velocity in the annulus. The diameter of the laser-drilled hole was assumed to be equal to the diameter of the inner-cannula inner-radius or 100 µm. Using the same reasoning as given for the inner-cannula offset in the CMA 20, the offset to the center of the laser-drilled whole is the sum of the hole radius and annulus channel depth, or 125 µm.

2.4 2D Axisymmetric CMA 20 Model and CMA 12 Models

The 2D Axisymmetric CMA 20 and CMA 12 models follow the model description as shown in Figure 2.1. Initial modeling was conducted by simplifying the µD probe geometry to a

2D axisymmetric geometry matching the analytical model developed by Bungay et al.[3] This assumes the concentration and velocity gradients along r are equal for every angle θ when rotated around z as shown in Figure 2.2 below. The reason this reduction in dimensions is possible is fully described in Section 3.2. The primary advantage of modeling in 2D is purely simulation time-based. For example, solving for 9 different flow rates using a fine mesh density took 1 minute 51 seconds with a 2D model compared to 19 minutes 10 seconds with the 3D model for 5 different flow rates; which normalized to 12.3 seconds and 127.7 seconds per flow rate, respectively; or approximately 90% simulation time reduction.

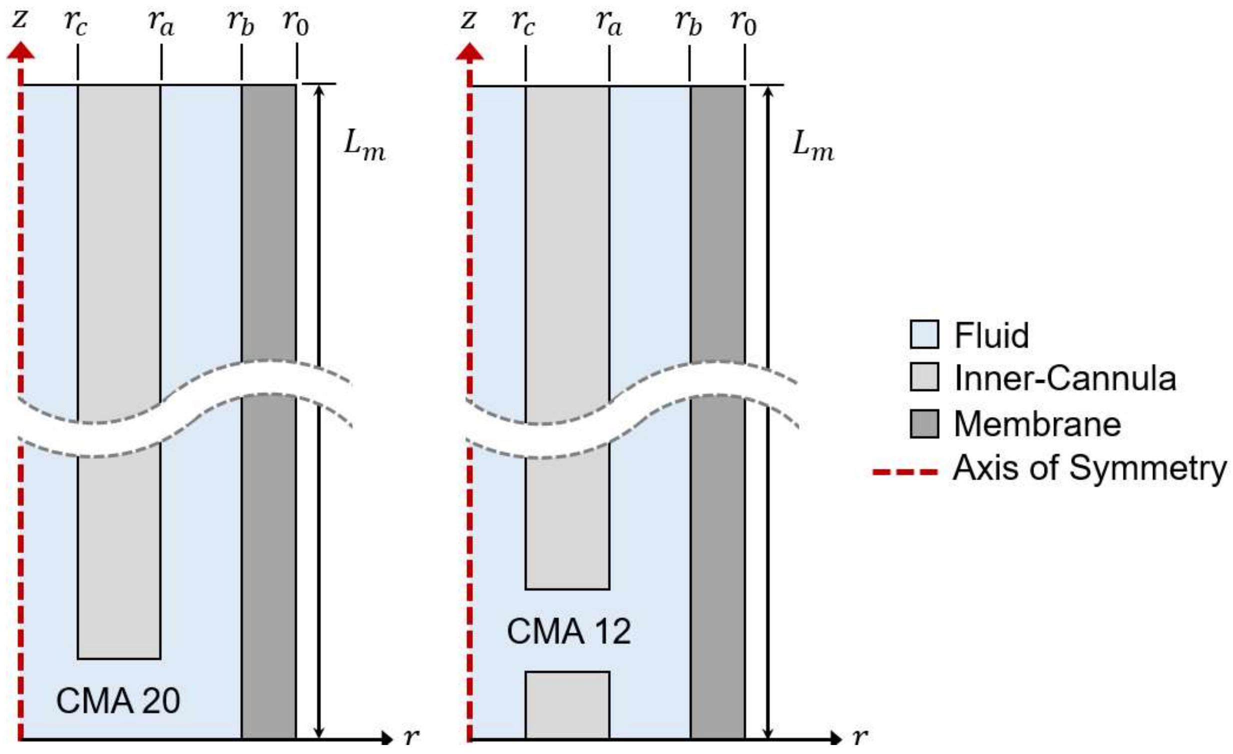

Figure 2.2. Depiction of 2D axisymmetric CMA 20 and 12 device geometry used in COMSOL.

For the CMA 12 model as shown in Figure 2.2, the actual physical set of holes is known to not fully circle the device in a ring as suggested. However, in order to allow for the model to remain axisymmetric, the hole was placed on the wall of the inner cannula and allowed to circle around the z-axis creating a ring-like gap. This assumption was allowed for the same volumetric flow rate to linear velocity assumptions described in Section 2.3.

2.5 3D CMA 20 and CMA 12 Models

A 3D model was constructed for the purpose of extending the µD model into geometries too complex to allow simplification into 2D or 2D axisymmetric models. It was possible to apply symmetry in 3D such as cutting the model in half down the length of the membrane but attempts to do so resulted in RR not matching experimental data. Figure 2.3 shows a cut view lateral cross-section of the 3D COMSOL model geometry for a CMA 20 µD probe.

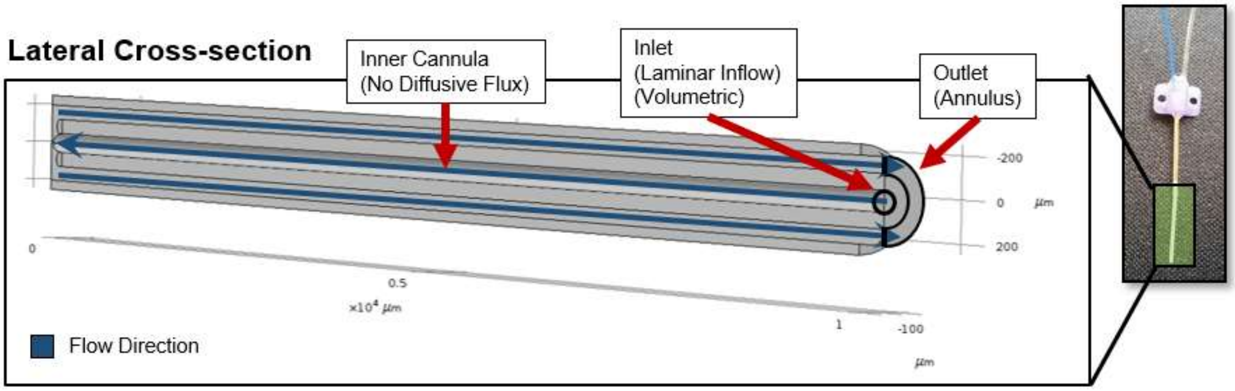

Figure 2.3. Depiction of commercial CMA 20 microdialysis device geometry.

This corresponds with the initial description from Figure 1.1 and dimensional variables as given by Table 2.1. All simplifications were used as described in Section 2.3

2.5.1 Inner-cannula Stabilization Problem

Initial simulations for the 3D CMA 20 and 12 models were found to fail at flow rates higher than 2.0 μL/min. It was initially suspected that the flow around the tip of the inner-cannula due to the sharp geometry features, changes in fluid linear velocity and direction, and subsequent changes in mesh density, was causing the simulation to fail. Different geometries were attempted (Filleted and Needled, Figure 2.4).

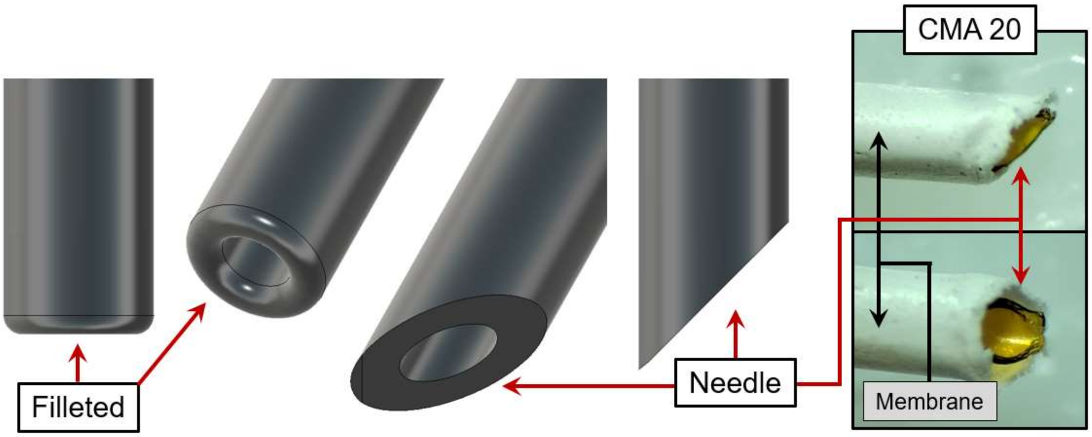

Figure 2.4. Depiction of simulated CMA 20 inner-cannula geometries simulated vs. actual.

The Filleted geometry was thought to remove the sharp edges and related mesh density problem which only added a curve while keeping the rest of the inner-cannula geometry the same. The Needled geometry matches what is seen in a commercial CMA 20 μD device as shown on the right side of Figure 2.4. Figure 2.5 shows no improvement in simulation success for the Needled geometry, and the Filleted geometry allowed for simulating up to 3.0 μL/min before failing. The improvement with Filleted geometry hinted that this was a fluid flow related problem. Subsequently, advection and diffusion physics were decoupled and solved separately to find that the model only failed when diffusion was enabled but solved when only laminar flow was enabled. It was found that applying a no-flux condition for the inner cannula allowed for simulations of flow rates higher than 2.0 μL/min for all geometries. It is believed COMSOL was attempting to calculate the diffusion against flow, where the linear velocity was the highest in a CMA 20 due to a 9.75x smaller cross-sectional area (0.008 mm^2) than the annulus (0.077 mm^2) at a constant inlet flow rate. The same problem occurs in smaller linear channel-based devices. COMSOL's solution to this problem and verification of this assumption are explained in Section 2.5.2.

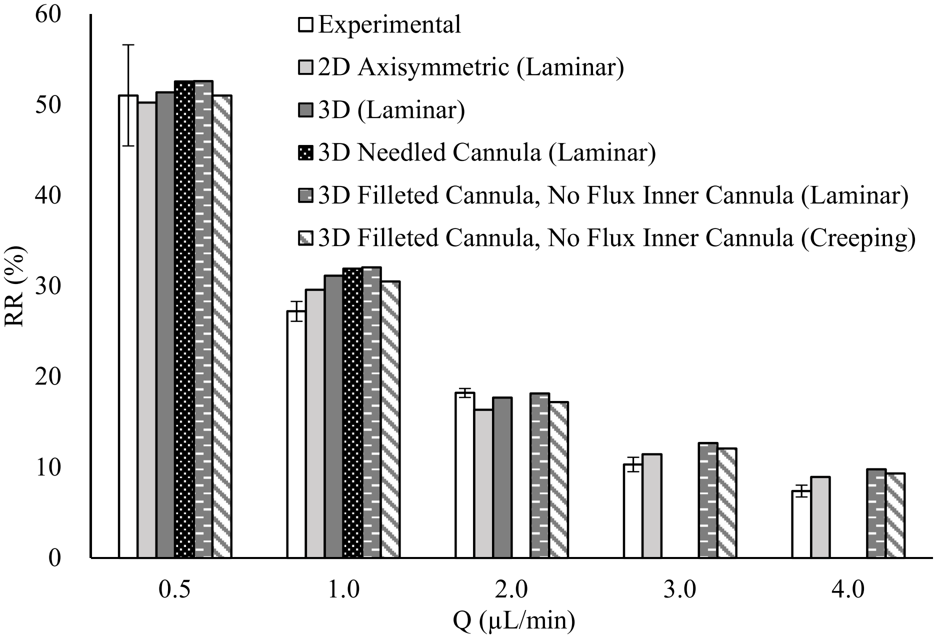

Figure 2.5. FITC-10 RR% results for a 3D CMA 20 using different inner cannula geometries.

2.5.2 Inconsistent Stabilization in COMSOL

An alternative method of preventing COMSOL solution failures under conditions where there is diffusion against the inlet flow is using the inconsistent stabilization for isotropic diffusion feature. COMSOL documentation states that if the localized Péclet number (Pe_L) is greater than 1, the solution can fail or become inaccurate.[47] In this case, COMSOL defines the Pe_L in Equation 2.14 for a single calculation step h as the characteristic length of a single mesh element, average linear velocity β, and diffusivity c. Figure 2.6 relates COMSOL's localized mesh Pe_L vs. flow rate at the minimum mesh element size of h = 0.0797 µm for the CMA 20 model and the h step size needed to adjust the Pe_L to 1.

$$Pe_L = \frac{\beta h}{2c} \qquad \text{(Equation 2.14)}$$

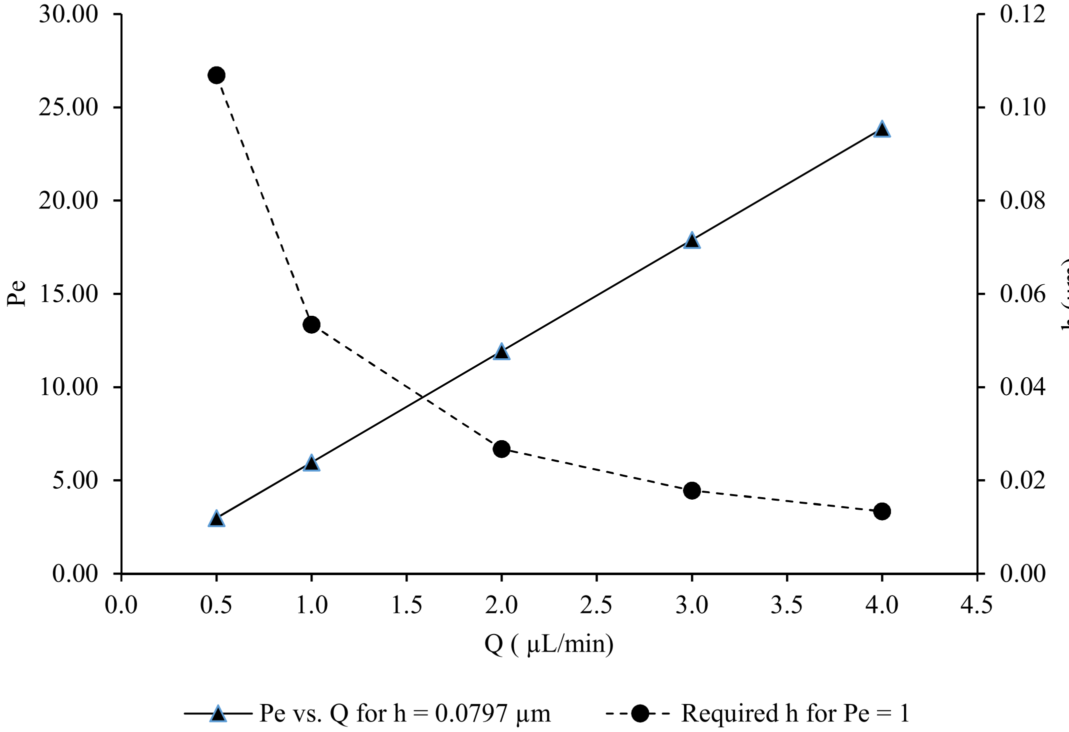

Figure 2.6. Plot of the relationship between COMSOL's localized mesh Pe_L vs. flow rate.

This is an example where the flow rate was increased and solutions failed above 2.0 µL/min without removing from diffusion completely from parts of the model where the average linear velocity was highest (up to 11.2 mm/s at 4.0 µL/min vs. 1.4 mm/s at 0.5 µL/min). COMSOL's solution is the addition of a correction factor $c_{art} = \delta\beta h$ that artificially increases diffusion; which is controlled by the constant δ to give a ratio of the average velocity and the step size (Equation 2.15). The inconsistent stabilization method is required for the linear looped devices discussed in Section 3.5 as there is no inner-cannula type structure where diffusion can be neglected as it only acts as a channel to direct fluid flow to the bottom of the probe prior to coming in contact with the membrane.

$$Pe_L = \frac{\beta h}{2(c + c_{art})} \qquad \text{(Equation 2.15)}$$

In the linear looped devices, the entire laminar flow domain is adjacent to a membrane, and therefore subjected to a diffusive boundary condition. The removal of diffusion in the channel would result in no RR. It should be noted that this method is not required when using a mesh of sufficient density (varies by model geometry). However, it is documented that mesh density increases memory and computational requirements quadratically.[48] This will be discussed in detail in Sections 3.5 and Chapter 4 for both Linear-Looped and Herringbone device geometries.

2.6 COMSOL Simulation vs. Experimental vs. Analytical Results

CMA 20 μD probe-based models were simulated vs. experimental data for FITC-10, FITC-20, C4-HSL, MCP-1, MCP-1 under biofilm conditions, TNF-α, IFN-γ, IL-5, IL-4, IL-2, vitamin B-12, and caffeine. Analyte names, abbreviations, molecular weight in Daltons, and RR experimental data sources are listed in Table 2.5. References and probes used by year are denoted in superscript. For this research. biofilm conditions are defined as a microdialysis probe with a *Vibrio harveyi* biofilm grown on the membrane surface. A biofilm is a type of bacterial colony that provides the bacteria protection from antibiotics and inflammatory response. The physical structure of this biofilm increases the membrane resistance by covering the membrane surface decreasing surface area available for diffusion.

Table 2.5. Simulated analyte abbreviations and general properties.

Abbreviation	Full Name	MW (kDa), Structure	RR Source
TNF-α	Tumor Necrosis Factor alpha	17.3, Monomer	Xiaoping^{43,A}
IFN-γ	Interferon gamma	15.9, Homodimer	Xiaoping^{43,A}
IL-5	Interleukin 5	21.7, Monomer	Xiaoping^{43,A}
IL-4	Interleukin 4	13.6, Monomer	Xiaoping^{43,A}
IL-2	Interleukin 2	17.2, Monomer	Xiaoping^{43,A}
MCP-1	Monocyte Chemoattractant Protein 1	13.1, Homodimer	Experimental
FITC-4	FITC Dextran 4,000	4, Rod	Experimental^{C}
FITC-10	FITC Dextran 10,000	10, Coiled	Experimental ^{B,C}
FITC-20	FITC Dextran 20,000	20, Highly Branched	Experimental^{C}
C4-HSL	N-butyryl-L-Homoserine lactone	171.2 Da	Experimental^{C}
MO	Methyl Orange	327.3 Da	Experimental^{B,C}
B-12	Cobalamin	1.3	Experimental^{C}
None	Caffeine	194.2 Da	Experimental^{C}

^{A} CMA 20 (2005)
^{B} CMA 20 (2015)
^{C} CMA 20 (2016-2018)

RR was also calculated using Bungay's analytical model given by Equation 1.2. This was done to show that the analytical model is applicable to the CMA device geometries when it is used to determine the membrane diffusivity for stirred conditions. It is important to understand that the analytical model only applies to the cylindrical geometry (CMA 12, CMA 20) devices. The analytical calculations are presented in comparison with the simulation and experimental data to ensure confidence in the precision of the simulated results prior to altering the geometry within COMSOL. It should be noted that this calculation was just a verification that the method of determining the D_m using Equation 2.13 was valid. The calculation did nothing more than use the calculated D_m to calculate RR.

2.6.1 Materials and Methods

A solution of 10 mM phosphate buffered saline (PBS) pH 7.4 containing 137 mM sodium chloride, 2.7 mM potassium chloride, 10 mM dibasic sodium phosphate, 1.5 mM, and monobasic potassium phosphate in HPLC water (Fisher Scientific) was used as the perfusate. The same PBS was used to make stock solutions of 100 µM Methyl Orange (327 Da), fluorescein isothiocyanate-dextran (FITC) 4000, 10000, and 20000 with each number corresponding the molecular weight of the dextran in kDa units (FITC-4, FITC-10, and FITC-20 respectively). All compounds were obtained from Sigma-Aldrich (St. Louis, MO) unless otherwise stated. Triplicate µD probes were placed in 2 mL centrifuge tubes containing the stock solutions listed previously using 3D printed probe mounting assemblies shown in Figure 2.7.

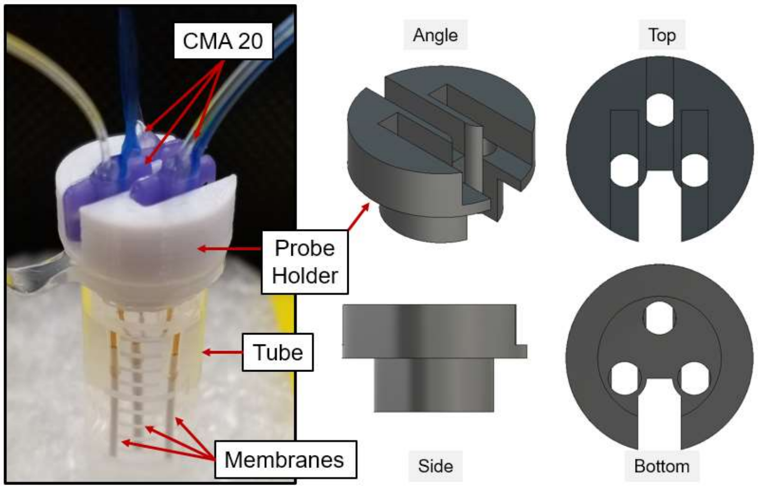

Figure 2.7. 3D printed µD probe holder for 2 mL centrifuge tubes.

Using this assembly, probes were held evenly spaced 3 mm from the center at 120° angles to minimize any possible concentration gradient interference between probes or blocking of the membranes due to physical contact between the probes. The probes were firmly held in place preventing accidental removal and damage by pulling on the inlet and outlet tubing. Additionally, the probe holder minimizes sample medium volume required for three probes from 4.5 mL split between three separate sample mediums for each probe to 1.9 mL in a single sample medium for all three probes. The μD probes were connected to a BASi syringe pump (model MD-1001) where PBS was perfused and subsequent dialysate samples were collected for pump settings ranging from 0.1 to 5.0 μL/min (see individual figures for exact flow rates). Dialysate samples were analyzed for FITC-dextran for absorbance on a Thermo-Scientific Nanodrop 2000c UV-Vis spectrophotometer. This methods and material section applies to all of the following experimental sections unless otherwise specified. MCP-1 was quantified using a BD OptEIA Rat MCP-1 Enzyme Linked Immunosorbent Assay (ELISA) Kit and TECAN M200 UV-Vis plate reader.

2.6.2 Results

COMSOL simulations for CMA 20 and CMA 12 μD devices using 2D axisymmetric and 3D models were compared with experimental and analytically calculated $RR\%$ using Equation 1.3. For all experimental data, the error bars represent the standard deviation of the average for n = 3 probes. Figure 2.9 to Figure 2.22 give simulated 2D axisymmetric, 3D, and analytical RR results vs. experimental for FITC-4, FITC-10, FITC-20, C4-HSL, MCP-1, TNF-α, IFN-γ, IL-5, IL-4, IL-2, B-12, MO, and caffeine. Figure 2.8 gives the minimum and maximum absolute error in $RR\%$ for all 2D asymmetric and 3D COMSOL simulations from Figure 2.9 to Figure 2.22. Absolute error did not change significantly as RR decreased with higher flow rates; however, relative error did increase since the absolute error is more or less an offset in comparison with the experimental value.

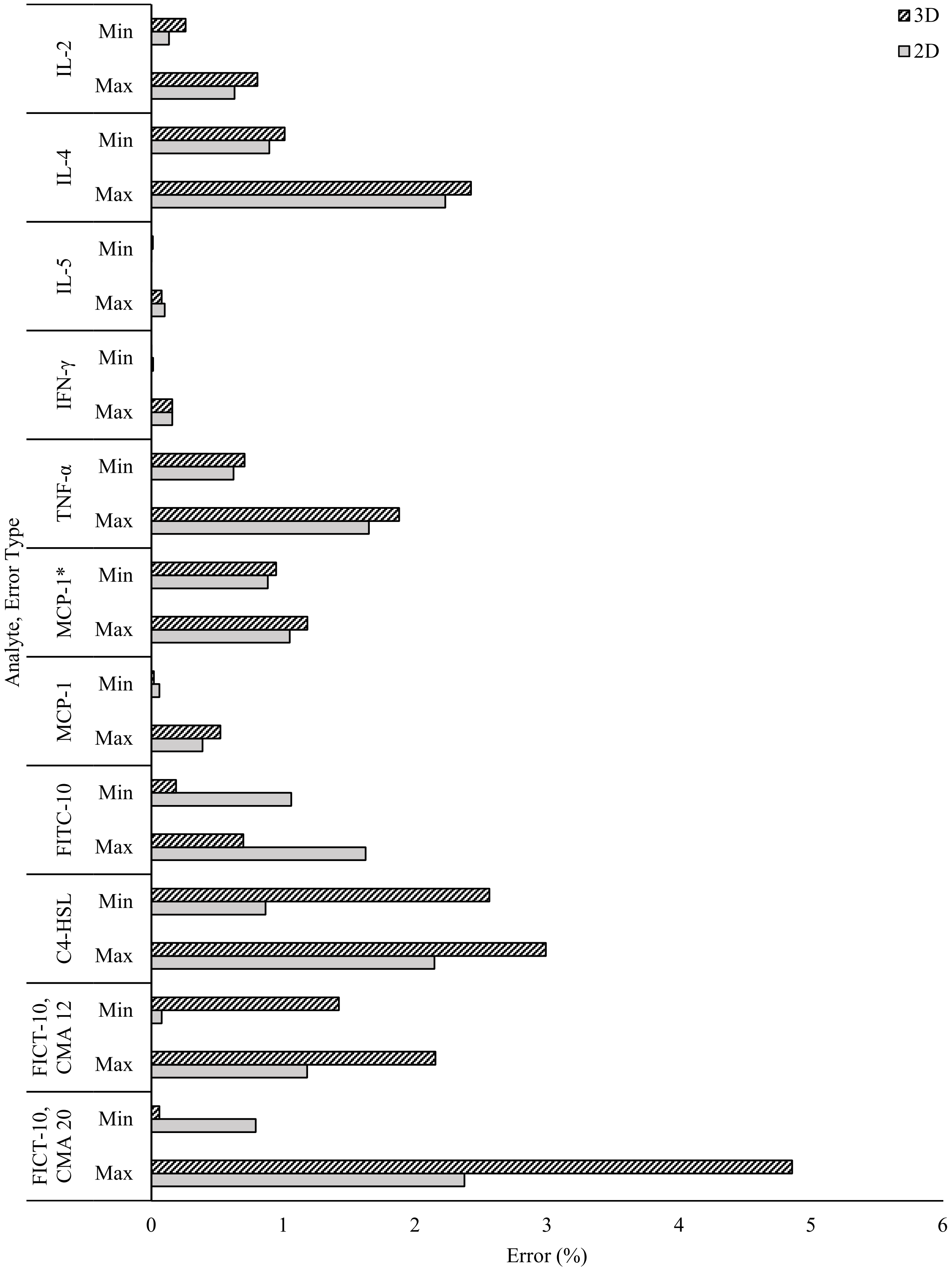

Figure 2.8. Absolute error (min and max) in *RR*% for all CMA device COMSOL simulations.

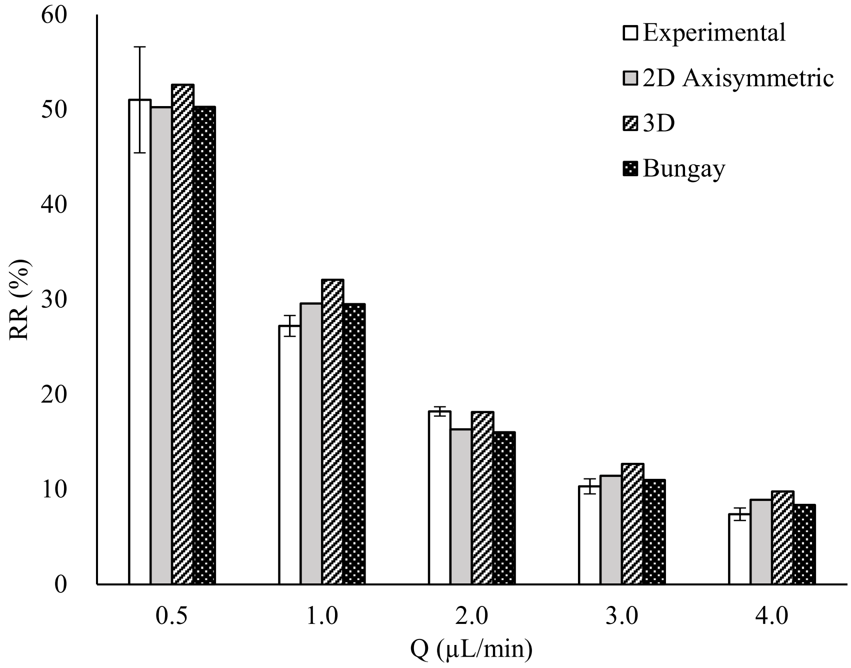

Figure 2.9. FITC-10 COMSOL vs. experimental *RR*% for 2015 CMA 20 microdialysis probe.

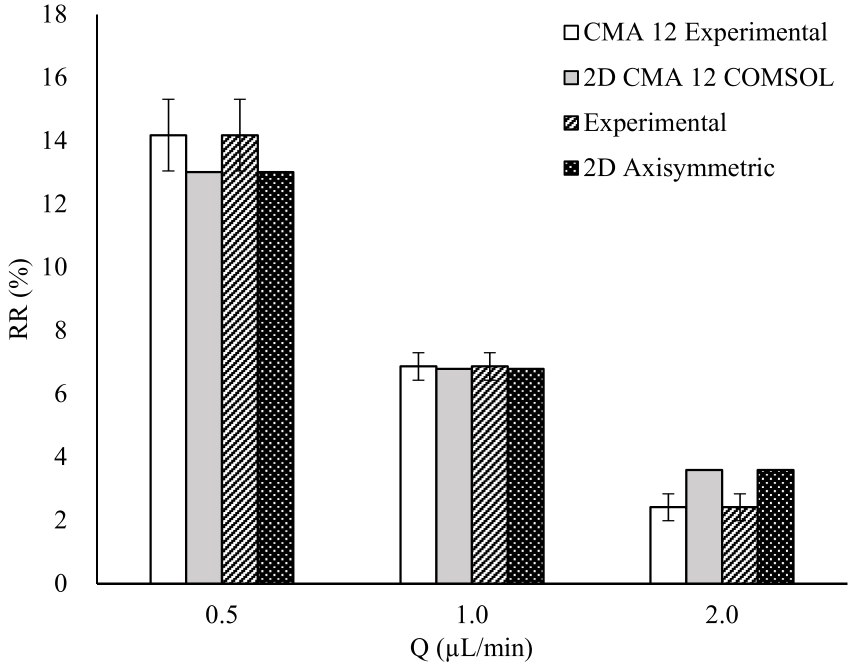

Figure 2.10. FITC-10 COMSOL vs. experimental *RR*% for 2015 CMA 12 microdialysis probe.

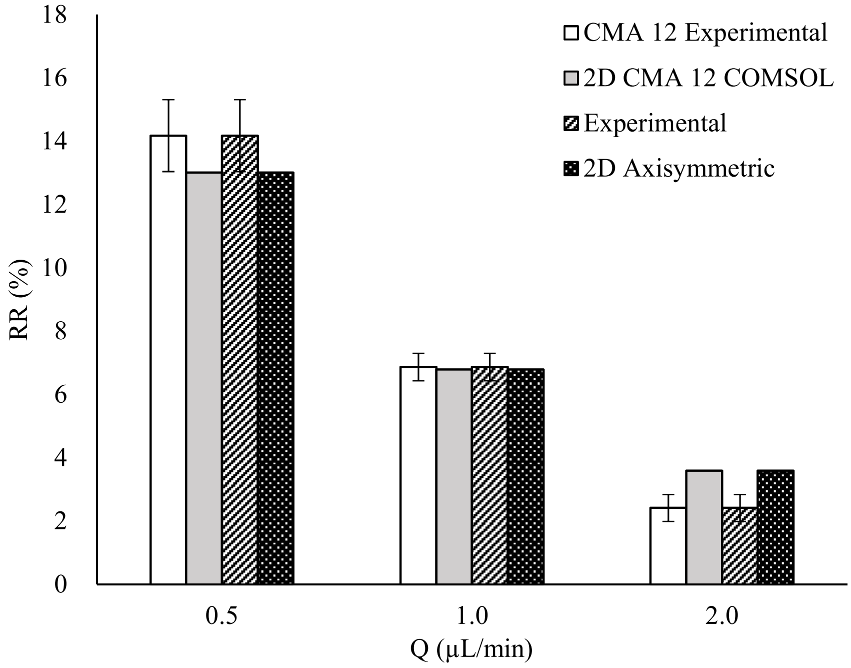

Figure 2.11. FITC-4 COMSOL vs. experimental *RR*% for 2016-2018 CMA 20 microdialysis probe.

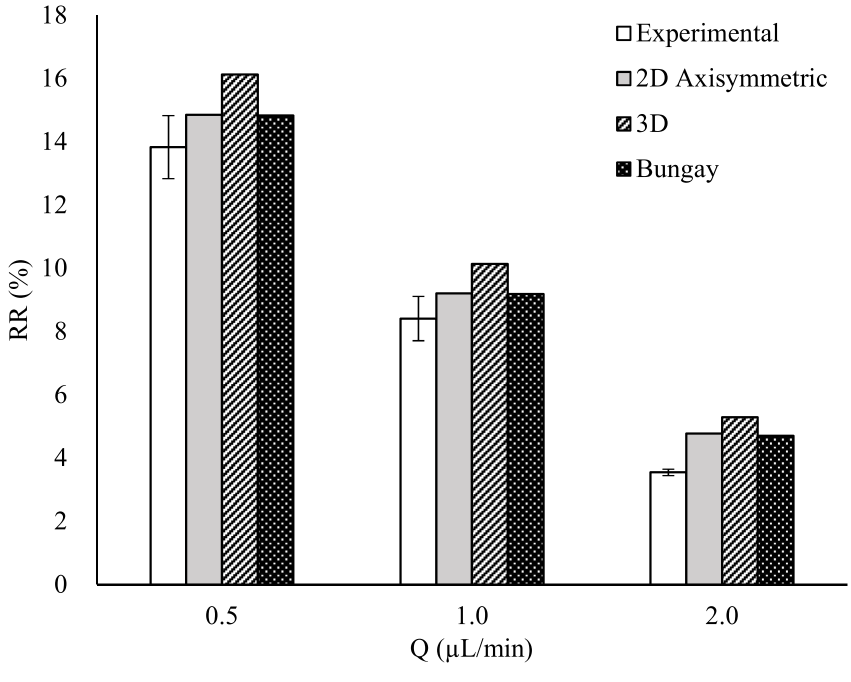

Figure 2.12. FITC-20 COMSOL vs. experimental *RR*% for 2016-2018 CMA 20 microdialysis probe.

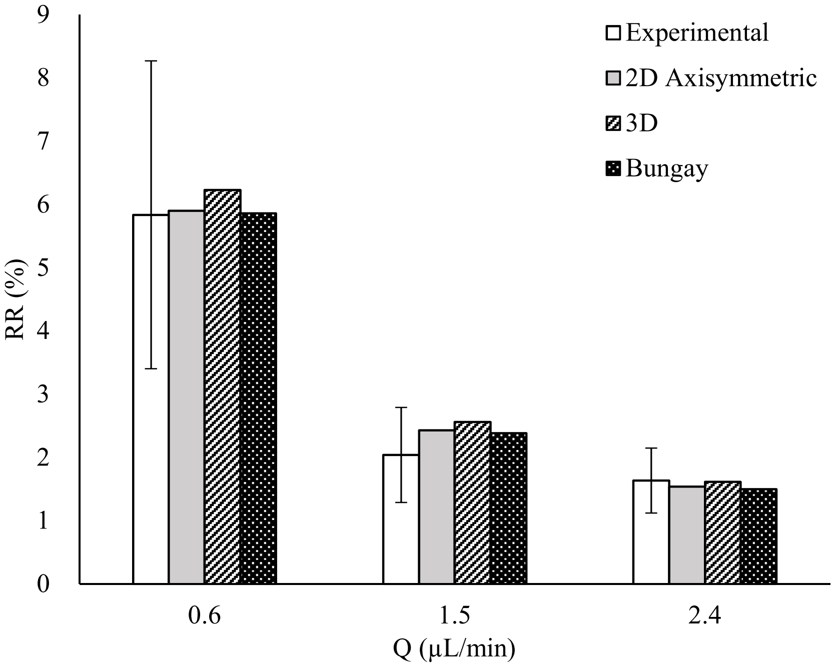

Figure 2.13. MCP-1 COMSOL vs. experimental *RR*% for 2016-2018 CMA 20 microdialysis probe.

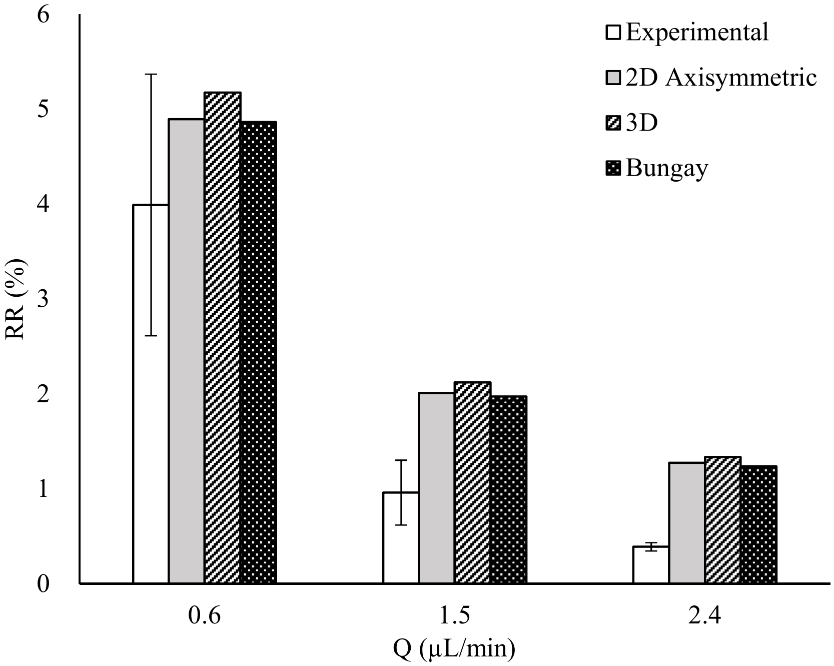

Figure 2.14. MCP-1 COMSOL vs. experimental *RR*% for a 2016-2018 CMA 20 microdialysis probe with biofilm.

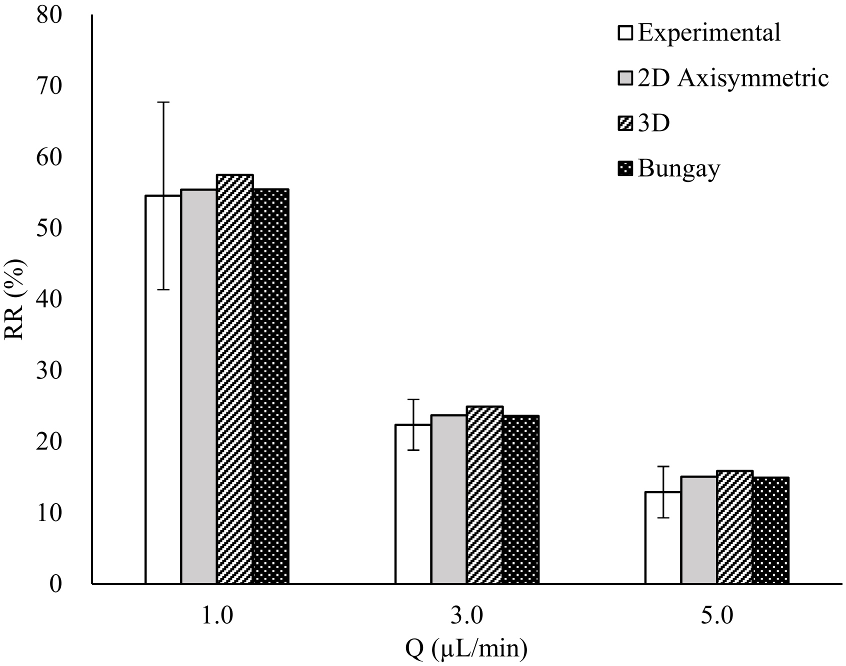

Figure 2.15. C4-HSL COMSOL vs. experimental *RR*% for a 2016-2018 CMA 20 microdialysis probe.

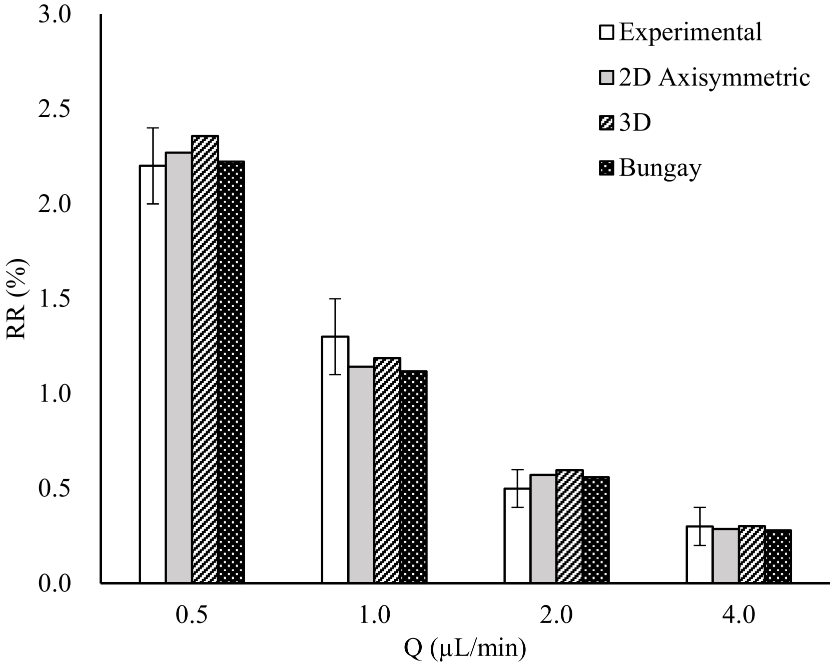

Figure 2.16. IFN-γ COMSOL vs. experimental *RR*% for a 2006 CMA 20 microdialysis probe.

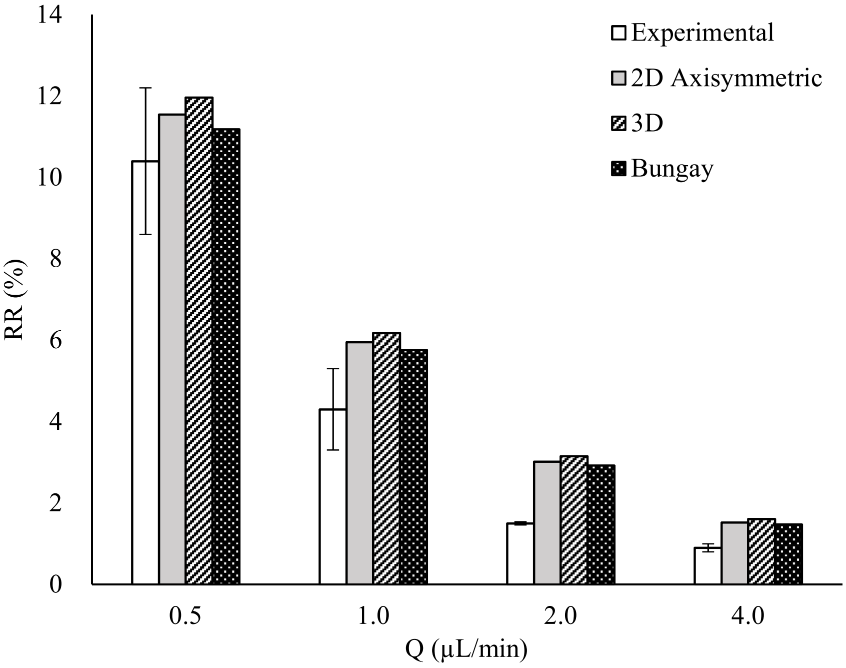

Figure 2.17. TNF-α COMSOL vs. experimental *RR*% for a 2006 CMA 20 microdialysis probe.

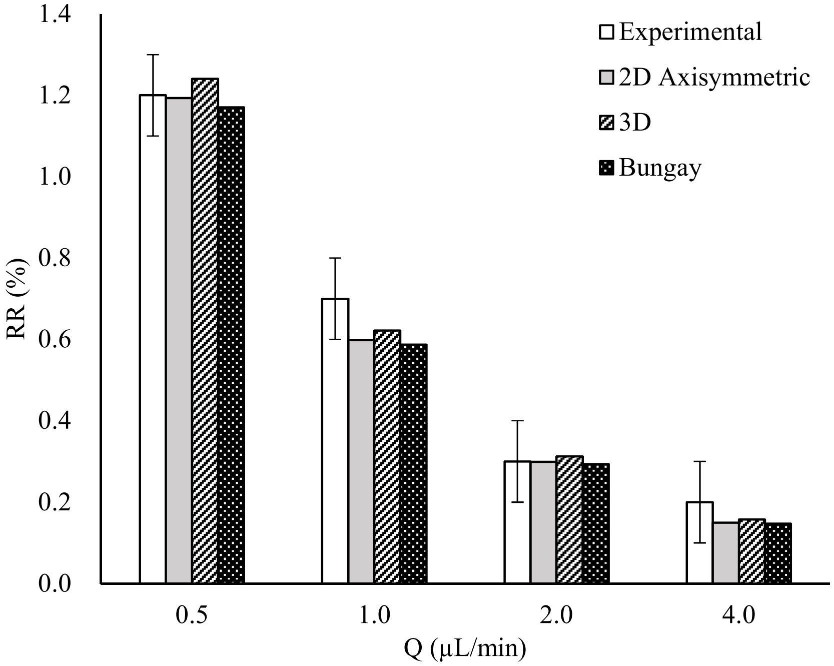

Figure 2.18. IL-5 COMSOL vs. experimental *RR*% for a 2006 CMA 20 microdialysis probe.

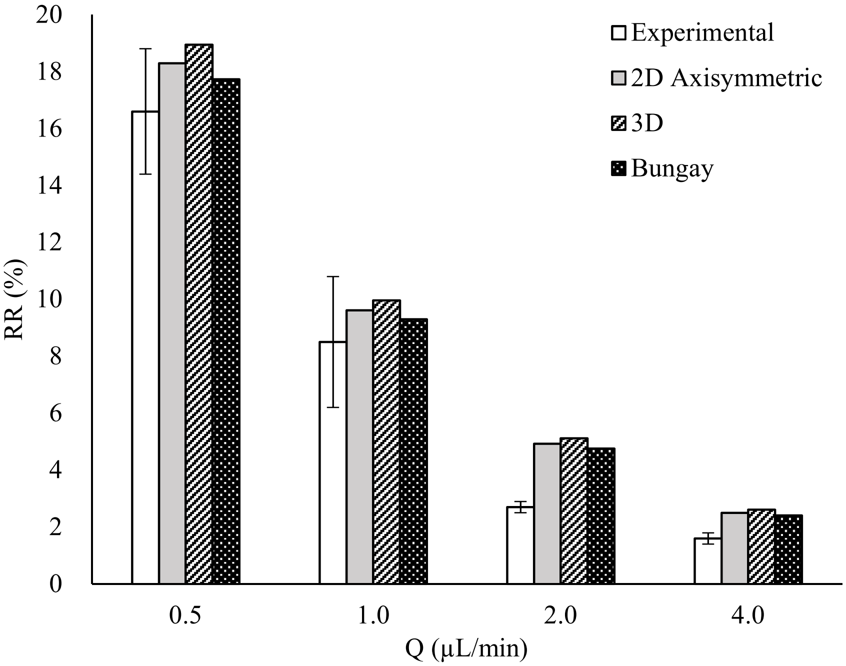

Figure 2.19. IL-4 COMSOL vs. experimental *RR*% for a 2006 CMA 20 microdialysis probe.

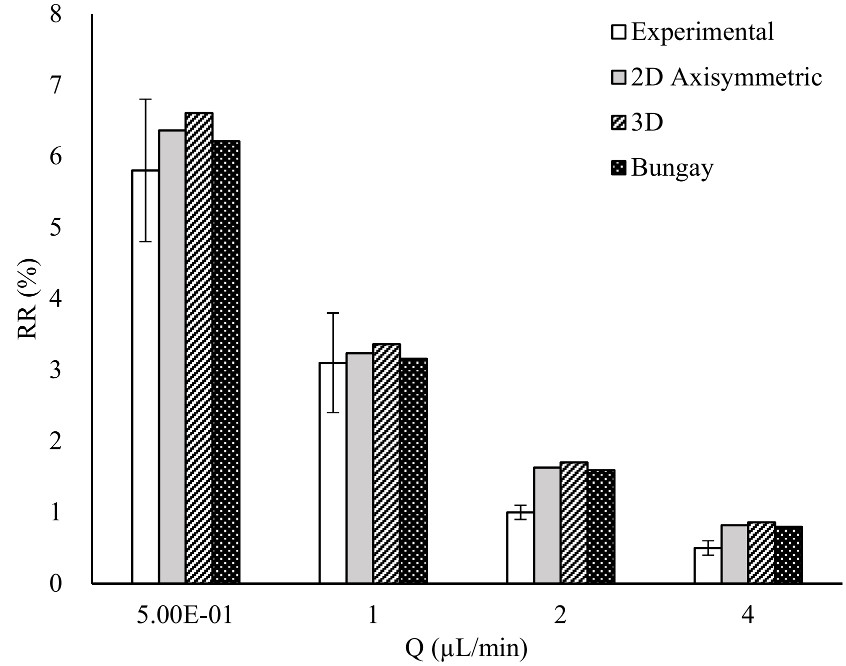

Figure 2.20. IL-2 COMSOL vs. experimental *RR*% for a 2006 CMA 20 microdialysis probe.

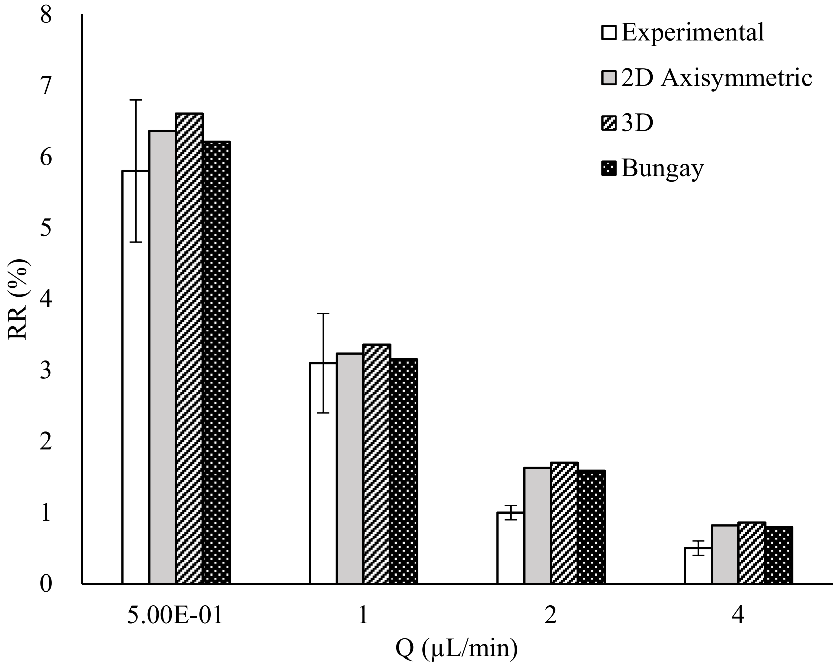

Figure 2.21. B-12 COMSOL vs. experimental RR% for a 2016-2018 CMA 20 microdialysis probe.

It was not a valid comparison to say the model was inaccurate when the relative error was greater than 50% at 5.0 μL/min, but less than 5% at 1.0 μL/min when the average absolute difference was approximately 1% RR. Both Figure 2.13 and Figure 2.14 give RR for MCP-1 with the difference being *Vibrio harveyi* biofilm grown on the membrane. This showed that Bungay's analytical model could be used to determine a membrane diffusivity that could account for a reduction in diffusive mass transport compared to a probe without a biofilm, and that COMSOL could replicate those results. Data collected in Figure 2.13 and Figure 2.14 was done using a similar probe holder design to Figure 2.7, but modified for a 5 mL centrifuge tube.

Experimental RR TNF-α, IFN-γ, IL-5, IL-4, IL-2 was thought to be obtained under quiescent conditions (not-stirred), but it is not specifically stated due to a recovery table comparing TNF RR (10% quiescent and 30% stirred) for a different experiment.[43] The D_m used gave accurate RR as it represents the diffusivity of both the sample medium and the membrane; in other words, the sum of the total diffusive mass transport resistance. This allowed for a well-stirred simulation to simulate quiescent conditions as it essentially averaged the two domains into a single constant.

2.6.3 Membrane Diffusivity Estimation in COMSOL

The simulation of caffeine (Figure 2.22) deviated from the experimental results as flow rate increased with a maximum absolute error of 9.91% or 29.9% relative error. Different error correction mechanisms were investigated in attempt to understand if COMSOL was calculating RR incorrectly, or if the problem was related to initial conditions such diffusion coefficients (D_d, D_m). Alterations to different error correction mechanisms (Table 2.6) did not change RR by more than 0.20% absolute difference with the exception of inconsistent stabilization (2.09%; which was designed to add artificial diffusion to the simulation).

Table 2.6. COMSOL caffeine relative recovery using different error correction mechanisms.

Simulation Conditions	Q (μL/min)	0.5	1.0	2.0	3.0	4.0
Mesh = Normal	RR (%)	98.94	89.83	68.36	53.80	44.17
Mesh = Extremely Fine		98.92	89.71	68.17	53.60	43.97
ICS = 0.25*		99.05	90.72	70.33	55.98	46.26
Crosswind Diffusion = Codina*		98.94	89.82	68.35	53.77	44.12
Full Residual*		98.94	89.83	68.36	53.80	44.17
Quadratic Discretization*		98.94	89.82	68.34	53.76	44.11
No Streamline Diffusion*		98.94	89.84	68.37	53.81	44.18

*Normal Mesh Size

These different error correction mechanisms (also known as stabilization mechanisms) are specific to the finite element method used by COMSOL, and are discussed in detail on their website.[47] Table 2.7 gives notes and descriptions of the error correction mechanism settings used in the simulations introduced by Table 2.6

Table 2.7. COMSOL error correction mechanism parameters notes and descriptions.

Model Parameter	Description and Notes
Normal Mesh	Deceases RR as expected for parabolic flows based on simulation experience with changing mesh densities on linear looped devices compared to HB devices (Chapter 4).
Extremely Fine Mesh	Increases RR
ICS = 0.25*	Default is Do Carmo and Galeao
Crosswind Diffusion = Codina*	Enables extra calculations typically ignored by the solver as they do no change the results, but will slow down the simulation
Full Residual*	Solver setting, no apparent change
Quadratic Discretization*	Discretization method, Linear is default
No Streamline Diffusion*	Streamline diffusion disabled (diffusion along the fluid streamlines, essentially longitudinal diffusion)

*Normal Mesh Size

Section 2.5.2 discussed the use of inconsistent stabilization in this research. It is believed COMSOL was predicting recovery correctly as COMSOL relies on a correct D_m and D_d to predeict RR vs. experimental data. The D_d for caffeine was found in literature, and the calculated value from density and MW (Section 2.2.1) was only 1% different ($6.97 \cdot 10^{-6}$ cm^2/s calculated vs. $7.04 \cdot 10^{-6}$ cm^2/s literature).[40] When plugging in the D_m back into Equation 1.2, the RR matched COMSOL. It is believed that the D_m was incorrect, and Bungay's analytical model was overestimating the D_m as derived using the method discussed in Section 2.2.2. This could be due to the high D_d and high RR at higher flow rates. Specifically, the concentration boundary layer had not completely collapsed at flow rates above 3.0 µL/min (discussed in Chapter 4). Figure

2.22 shows a parametric sweep of decreasing ratios (1.0x to 0.5x) of D_m from the overestimated Bungay D_m. Sweeping fractions of Bungay's D_m ($1.54 \cdot 10^{-6}$ cm^2/s) allowed for a model that reduced the maximum absolute error to 6.44% RR for and the relative error was reduced to 10% at 2.0 µL/min using a $D_m = 1.07 \cdot 10^{-6}$ cm^2/s. The previous relative error of 29% was reduced to 1% at 4.0 µL/min.

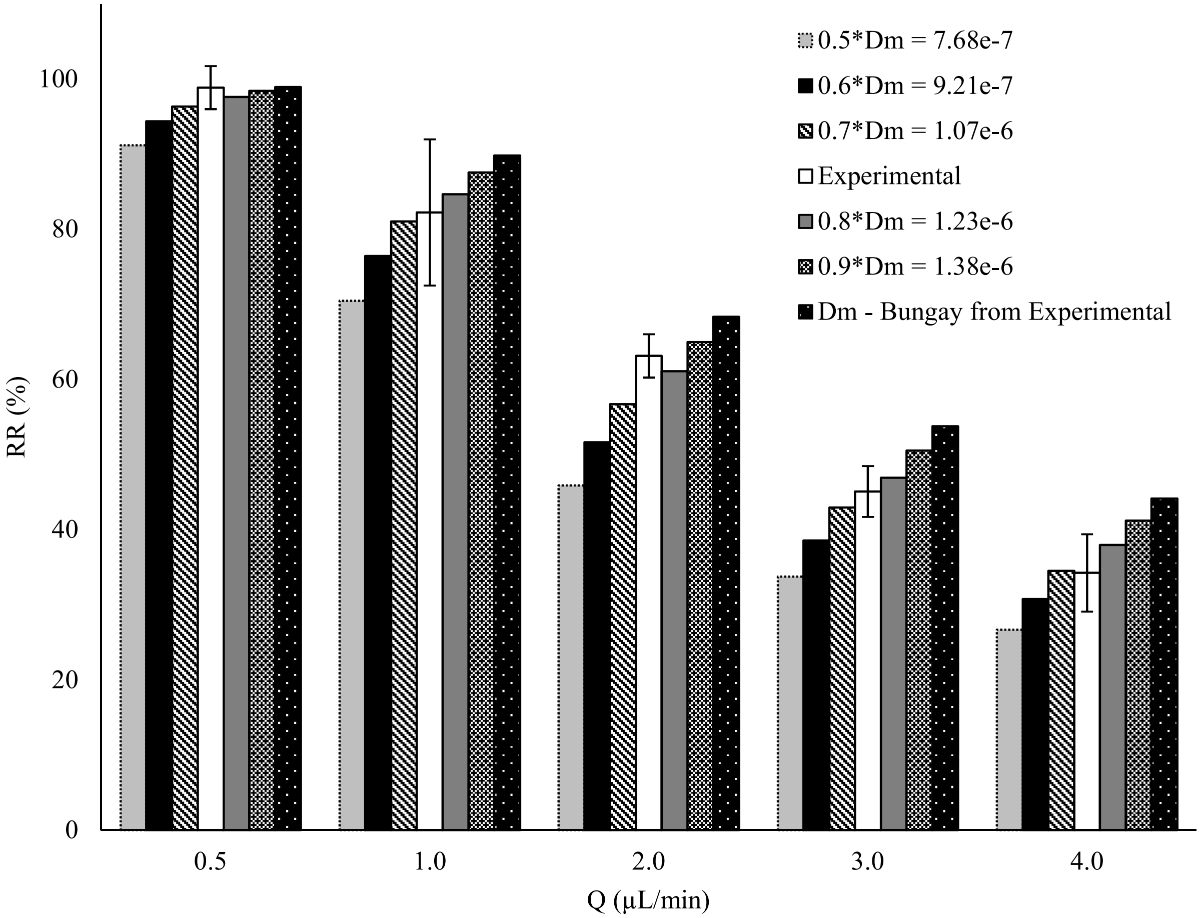

Figure 2.22. Caffeine COMSOL vs. experimental RR for different membrane diffusivities.

2.7 Conclusion

COMSOL Multiphysics FEM software was used to simulate and quantify the advection-diffusion driven microdialysis sampling process and compared to experimental data. Experimental data was used to derive the required aqueous and membrane diffusivity constants for use in simulations (Section 2.2). Different aspects of the modeling procedure were investigated to include the model definition, changes to the inner-cannula geometry, and the functionality of the inconsistent stabilization diffusion correction factor (Sections 2.3 and 2.3). It was demonstrated that COMSOL could be used effectively to model commercial CMA 20 and CMA 12 μD probes for a wide range of analytes to include FITC-10, FITC-20, C4-HSL, MCP-1, TNF-α, IFN-γ, IL-5, IL-4, IL-2, vitamin B-12, and caffeine (Section 2.5). The simulation was further expanded to include sweeping membrane diffusion coefficients and the effect of altering different FEM diffusion solver settings towards matching simulation with experimental data (2.6.3). This research has shown that commercial microdialysis devices can be simulated using COMSOL Multiphysics. This served as a strong foundation towards implementing new novel geometries as presented in Chapter 3 and Chapter 4 of this research (linear-looped channels and herringbone mixing, respectively).

Chapter 3. Design and Simulation of a Microfluidic Microdialysis Device

3.1 Introduction

The primary focus of this research was to improve extraction efficiency of microdialysis sampling while at the same time using the potential multifunctional capability of microfabricated (μF) planar devices. As previously discussed, only the microchannel geometry was considered; in the CMA 20 μD probe, the microchannel geometry was everything from the inner cannula to the annulus (lumen). For this research, the device was constructed using μF fabrication techniques and was limited to Cartesian (rectangular) channel geometries. In order to obtain performance greater than the previous cylindrical geometry, a full understanding of mass transport in the perfusate had to be understood. Properties of transport were analyzed over multiple dimensions from the simplest (1D) to the most complex (2D). An optimized geometry based on a linear-looped design was simulated using information covered in Chapter 2; and, subsequently, analyzed for improvements to include considerations for surface area to volume ratio.

3.2 1 and 2 Dimensional Properties

Specifically, for the perfusate (or a microchannel adjacent to a membrane), using a purely mass transport perspective under laminar flow conditions, μD can be simplified down to a competition of characteristic rates over a device geometry limited to a set of characteristic lengths over a period of time. At any point along the length L_m of a μD or microfluidic channel where diffusion is occurring, the following conditions apply. Any group of molecules of interest will move (random walk) with the concentration gradient according to its general diffusion coefficient (D). On average, these molecules will traverse a straight line known as the characteristic length (L) until the concentration of molecules on L is equal at all points. At steady state, this creates a 1-dimensional (1D) problem. The same is true for any fluid moving through the same channel where the characteristic rate is the average velocity (U) of all velocities along the same 1D line. The competition of these rates is defined by the Péclet number (Pe) in Equation 3.1.

$$Pe = \frac{UL}{D} \qquad \text{(Equation 3.1)}$$

Accordingly, the dominate rate is defined by this ratio, and for this research, a lower Pe was desired. The use of the Pe number can be explained as the distance a molecule can traverse over L during a specific time period and is limited by U. In the case of μD for any point along L_m, (any length point along the membrane) the diffusing particle is swept away by the fluid flow restricting the distance a diffusing molecule can traverse and, therefore, limiting any possible equilibrium with the external sample medium (ESM). Hence, a lower U or L (fluid velocity and channel thickness) is preferable in any device design where the goal is to reach equilibrium. The addition of time adds a second dimension (2D) on top of the physically 1D line. The entire process for a single point along L_m is depicted in Figure 3.1 2D. This diagram is a visual representation of the Pe number applied to a simple rectangular channel geometry starting at the lowest possible dimension.

In relation to RR, the primary goal was to allow all diffusing molecules to completely traverse L to allow the concentration along L to approximately equal the concentration external to the membrane. In other words, to reach equilibrium under the conditions in Figure 3.1, RR could be increased through combinations of decreasing U and L, or increasing D; where D was typically constant for this research due to a constant temperature (25 °C, 37 °C), and perfusate viscosity ($8.9 \cdot 10^{-4}$ Pa·s) and density (1000 kg·m^3). Decreasing U allowed a diffusing molecule to traverse more distance along L in a given time and decreasing L shortened the distance a diffusing particle was required to travel.

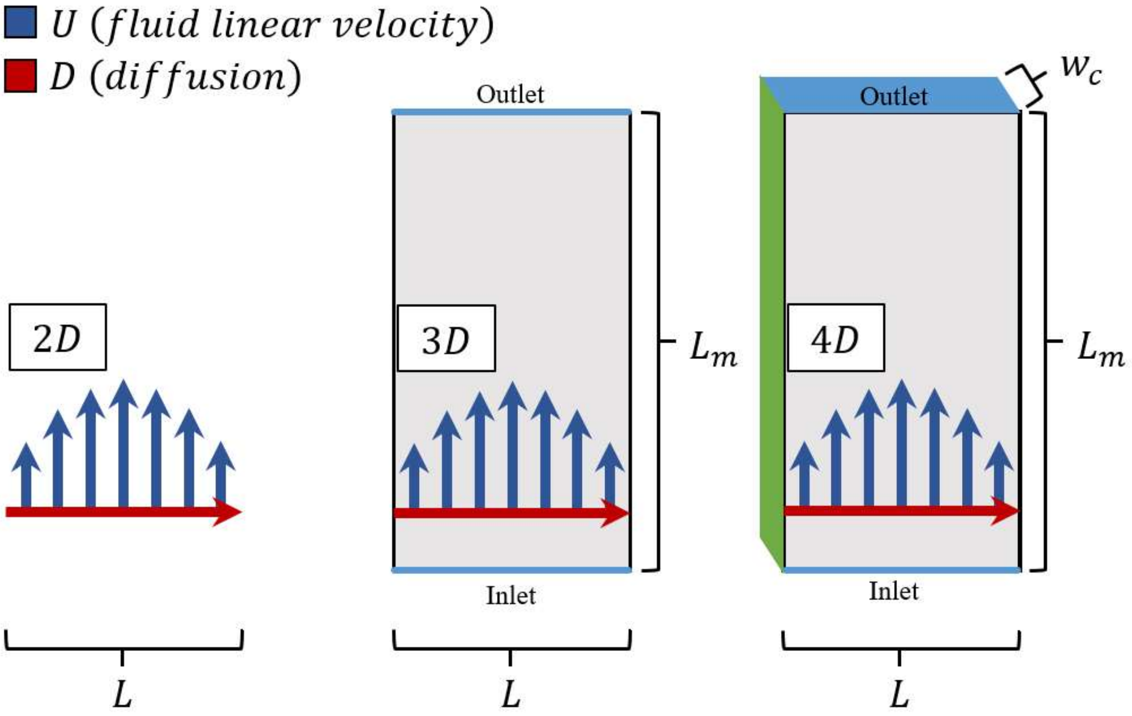

Figure 3.1. Depiction of a 1D line of length L, diffusivity D, and average linear velocity U under 2D, 3D, and 4D conditions.

3.3 3 and 4 Dimensional Properties

An additional 3rd dimension is added when the length of the device parallel to U is considered. If the previously mentioned 1D line is considered as a single line moving along L_m at sequential time points over time as shown in Figure 3.1 3D, then the distance traveled by the diffusing molecules by random walk will increase according to $x = \sqrt{2Dt}$, and RR will increase for longer L_m.[20] Diffusive and inlet/outlet boundaries in Figure 3.1 correspond with Figure 2.1.

The 4th dimension is added giving width (w_c) to the channel as shown in Figure 3.1 4D, and does not change RR under previously stated conditions of constant U, L, and D. Device volume should be considered when the sampling space is size restricted, or the detection method requires a specific volume and the time required to collect that volume. For example, an enzyme-linked immunosorbent assay (ELISA) requires a minimum of 50 µL sample volume. At a 1.0 µL/min inlet flow rate, it will take approximately 50 minutes to collect (the temporal resolution of the sample) using a CMA 20 µD probe. Therefore, the sample size, sampling space, and temporal resolution must be considered when determining channel width after determining the desired RR.

3.4 Application towards Device Design: Physical Size and Dimension Limitations

For this research, the initial device design had to be comparable to a CMA 20 µD probe, and there were respective size limitations to consider due to the size of target in vivo sampling space. The CMA 20 µD probe was chosen for design comparison as the Stenken lab has used it extensively over the last 15 years. The membrane length and device width (diameter for the CMA 20 µD probe) had to be approximately10 mm and 500 µm, respectively. The second limitation was the geometry based on the fabrication methods readily available. In this case, soft-lithography was used limiting the geometry to rectangular channels.[29] The cylindrical geometry of a CMA 20 µD probe could not be replicated using this method. With a fixed length (10 mm), the volume was derived from the cross-sectional area perpendicular to the length of the device (Figure 3.2). The distances of width, height, or diamneter, were representative of the area characteristic length, L from Figure 3.1.

There were additional device structures taking up space in the cross-sectional area such as the inner cannula in the CMA μD probe, support structures such as walls for a linear channel, and the membrane for both device types. Under those volume restricted conditions, minimizing the size of the inner cannula or channel walls allowed for changes in L and U. Accordingly, a constant cross-sectional area could be manipulated to increase RR by decreasing channel depth (increasing width). By keeping the cross-sectional area constant, the linear velocity was constant for any desired volumetric flow rate. This allowed the device design to be tuned to a specific RR.

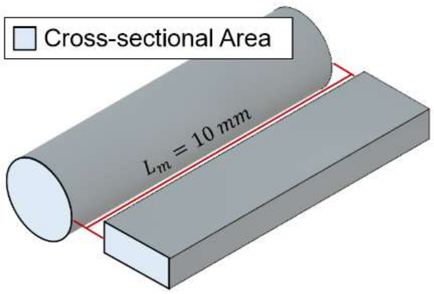

Figure 3.2. Depiction of cylindrical and Cartesian cross-sectional areas (blue).

3.5 Simulation and Optimization of a Linear Looped Microfluidic Microdialysis Device

The device was designed to maximize membrane surface area (for diffusive transport) in contact with the fluid, and cross-sectional area (for volumetric flow rate to control temporal resolution). Previous designs considered serpentine channels which decreased the membrane surface area in-order to allow for structural components (walls) needed to allow for each twist and turn.[46] These walls limited diffusive transport from the membrane and took up valuable device volume as discussed in Section 3.4. It can be shown in COMSOL that while not considering the resistances from the external sample medium (ESM), that maximizing surface area, minimizing membrane thickness (primary source of device diffusive restriction) and channel depth are key to increasing relative recovery (RR). This is due to shortening the diffusion lengths and reducing barriers which slow diffusion. In a perfect world, the entire device would be constructed of a thin, highly porous, durable membrane material. This would allow for concentration gradients to extend from all directions internally and externally to the probe. The closest functional example commercially available is a linear probe being a cylindrical membrane and no inner cannula restricting further diffusion. Figure 3.3 gives a basic physical representation of the proposed linear looped (LL) microfluidic (µF) µD device under its current design iteration in comparison to the commercially available CMA 20 100 kDa microdialysis probe.

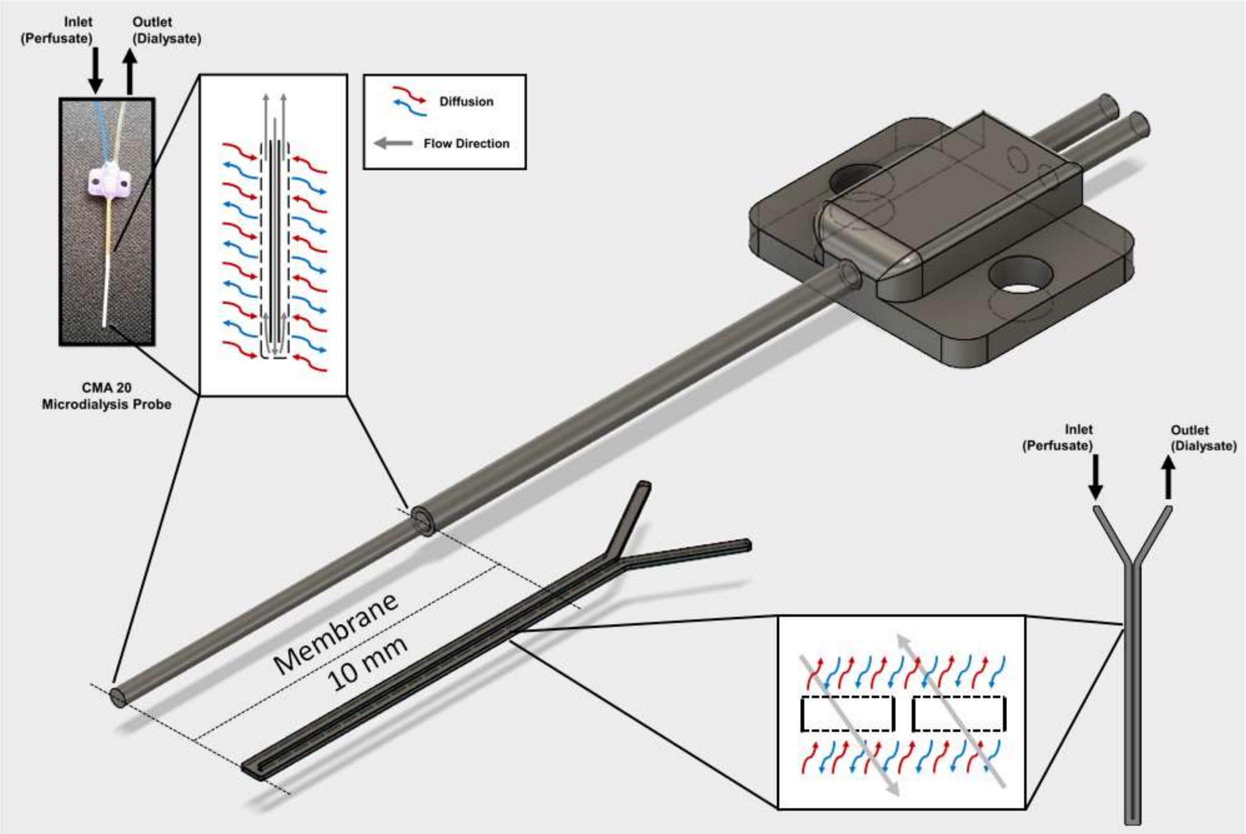

Figure 3.3. 2D and 3D graphical comparison of a CMA 20 100 kDa microdialysis probe and the proposed linear looped microfluidic microdialysis device.

The membrane length (L_m) was modeled at 10 mm to match the CMA 20 specifications. The CMA 20 (top left) depicts a 2D slice parallel to the flow direction whereas the linear looped probe (bottom right) is sliced perpendicularly. Devices are drawn to scale using Autodesk Fusion 360. Figure 3.4 shows cross-sectional slices perpendicular to flow. Two membrane configurations of LL µF µD devices were investigated in this research. The dual membrane LL (DLL) µF µD device implements a membrane on both the top and bottom of the channel as explicitly shown in Figure 3.4.

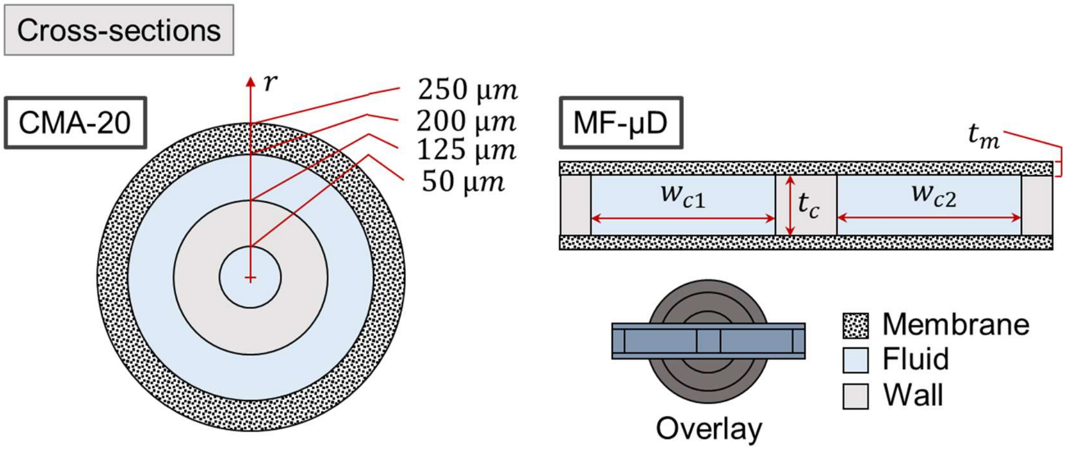

Figure 3.4. Cross-sectional comparison of a CMA 20 (left) and linear looped probe (right) (300 µm wide channels). An overlay is provided to give a more direct comparison of size.

The second device replaces a membrane with a channel wall resulting in only a single membrane LL (SLL) µF µD device. Table 3.1 quantifies the differences in dimensions by comparing LL µF µD device with channel widths of 250 µm (inlet) to 350 µm (outlet) (LL350), and 350 µm (inlet) to 450 µm (outlet) (LL450) to the CMA 20. Both LL350 and LL450 are assumed to have a DLL configuration unless otherwise specified; accordingly, Table 3.1 only considers the DLL µF µD devices, and values would be lower (not calculated) for SLL µF µD devices. The channel depth or thickness was chosen to be 100 µm due to fabrication limitations in material choice and availability given later in Section 3.8, and to maximize cross-sectional area for reasons described in Sections 3.2 and 3.3.

Table 3.1. Device dimensions comparison.

	250 (inlet) to 350 µm (outlet) Wide*		350 (inlet) to 450 µm (outlet) Wide*		CMA 20 100 kDa
	(mm^2)	Vs. CMA 20 (%)	(mm^2)	Vs. CMA 20 (%)	(mm^2)
Cross Sectional Area					
Fluid Total	0.060	71	0.080	95	0.084
Fluid in contact with Membrane	0.060	79	0.080	105	0.076
Fluid + Structural	0.106	76	0.134	97	0.196
Surface Area					
Membrane	12.1	76	16.1	101	15.90

* "Wide" refers to channel width.
* Fluid + structural cross-sectional area includes 50 µm wide outer wall, and 100 µm wide inner wall.

3.6 Linear-Looped Device Simulation Results and Discussion

Initially, simulations consisted of symmetric inlet/outlets of 300/300 and 400/400 µm wide channel devices. A change to the listed 250/350 and 350/450 µm devices (Table 3.1) was made to preemptively prevent back pressure problems with a wider outlet. This also kept the design consistent with previous preliminary work done by Randy Espinal Cabrera in the Stenken group, where the inlet and outlet was varied from 50 to 100 µm, respectively.[46] There was no difference performance-wise mathematically as the total sum of cross-sectional areas from inlet to outlet is the same, the membrane length was the same, and therefore the linear velocities, subsequent residence times, and resulting RRs were identical in simulations (Figure 3.5). Figure 3.6 shows a summarized RR for all LL devices using a fine mesh vs. the CMA 20 simulation for

FITC-10. Figure 3.7 to Figure 3.11 give FITC-10 RR for channel thicknesses of 70, 100, and 130 µm with both SLL and DLL configurations.

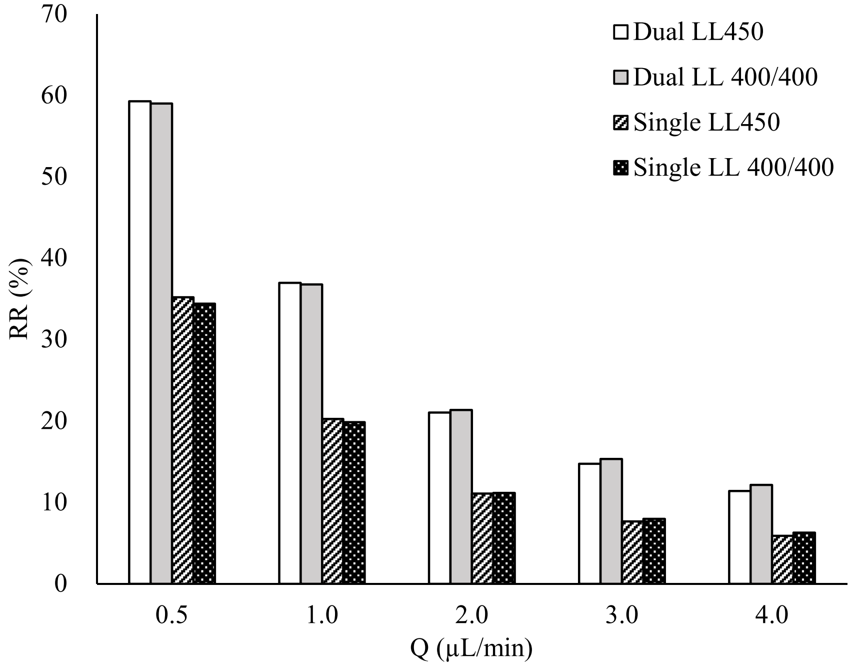

Figure 3.5. Comparison of asymmetric vs. symmetric linear looped µD device RR.

The RR comparisons made in Figure 3.5 and Figure 3.6 were limited to 100 µm channel depth and a fine mesh density. Mesh densities using COMSOL's physics controlled presets of coarse, normal, and fine were compared for differences in RR over all models. All devices used the same FITC-10 effective membrane diffusivity as determined experimentally using a CMA 20. It is expected that membranes of comparable or better can be fabricated in-lab using immersion precipitation (phase inversion) technique.[26] This process will be required to produce membranes of lower membrane restriction (R_m). A combination of optimizing three variables will be required as the perfect replication of the CMA 20 hollow fiber as a flat-sheet membrane is not realistic.

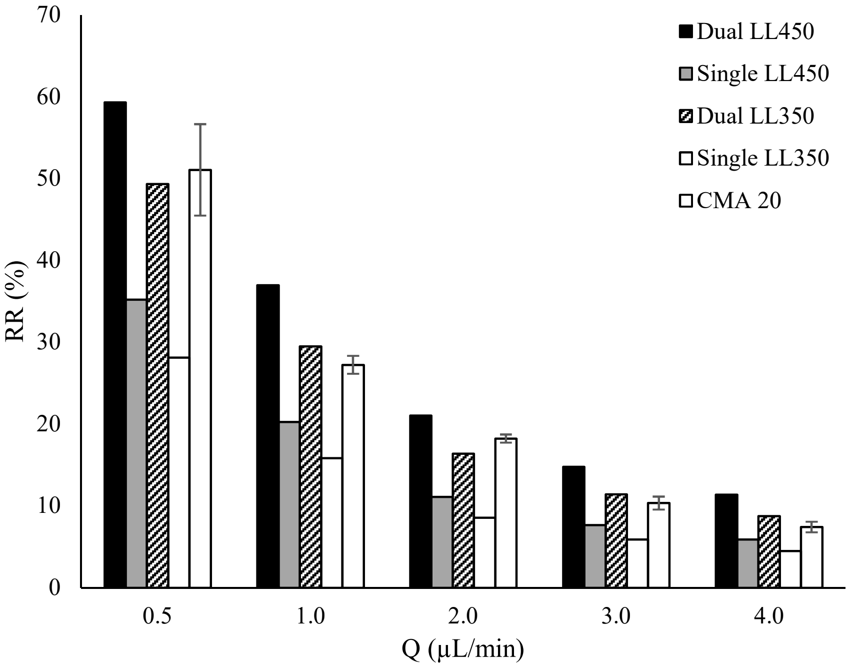

Figure 3.6. FITC-10 *RR*% results for a 3D CMA 20 for 100 μm channel depth.

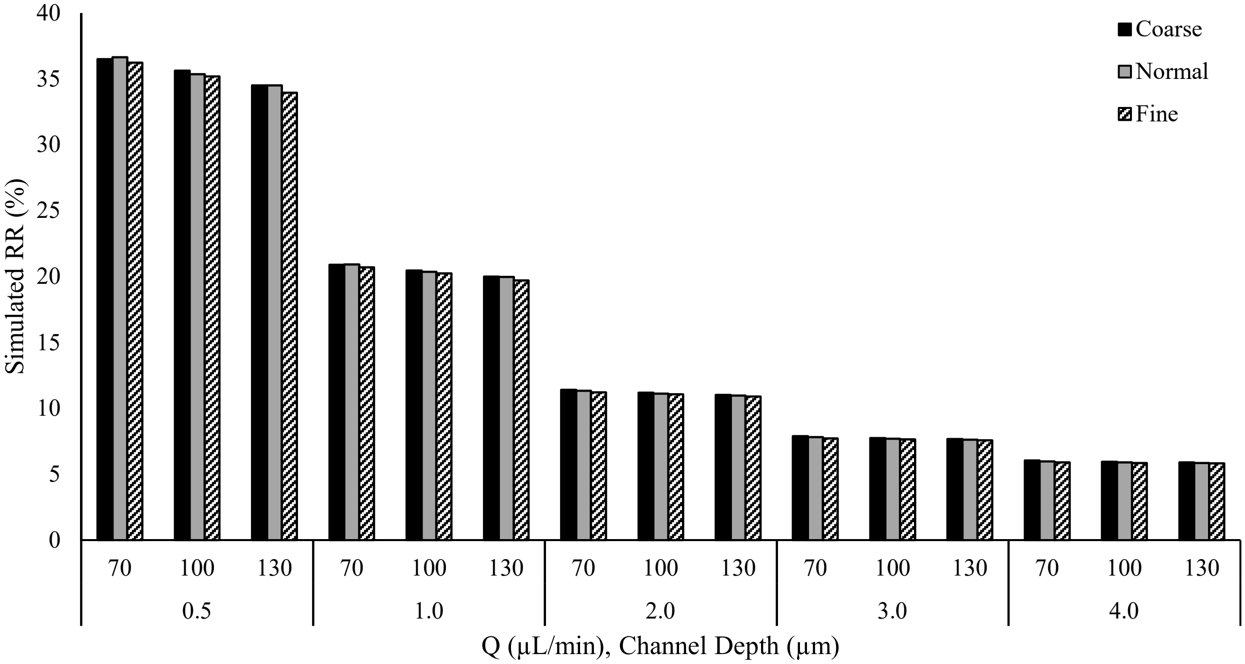

Figure 3.7. FITC-10 *RR* at multiple flow rates and channel thicknesses for a SLL450 device at COMSOL mesh density settings of coarse, normal, and fine.

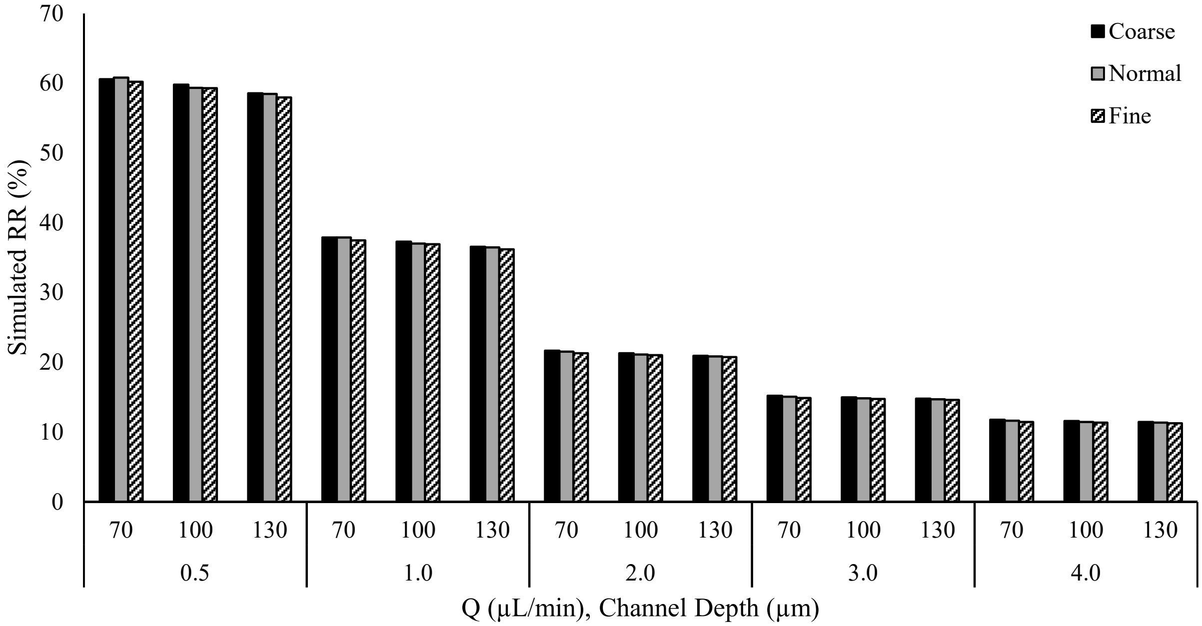

Figure 3.8. FITC-10 *RR* at multiple flow rates and channel thicknesses for a DLL450 device at COMSOL mesh density settings of coarse, normal, and fine.

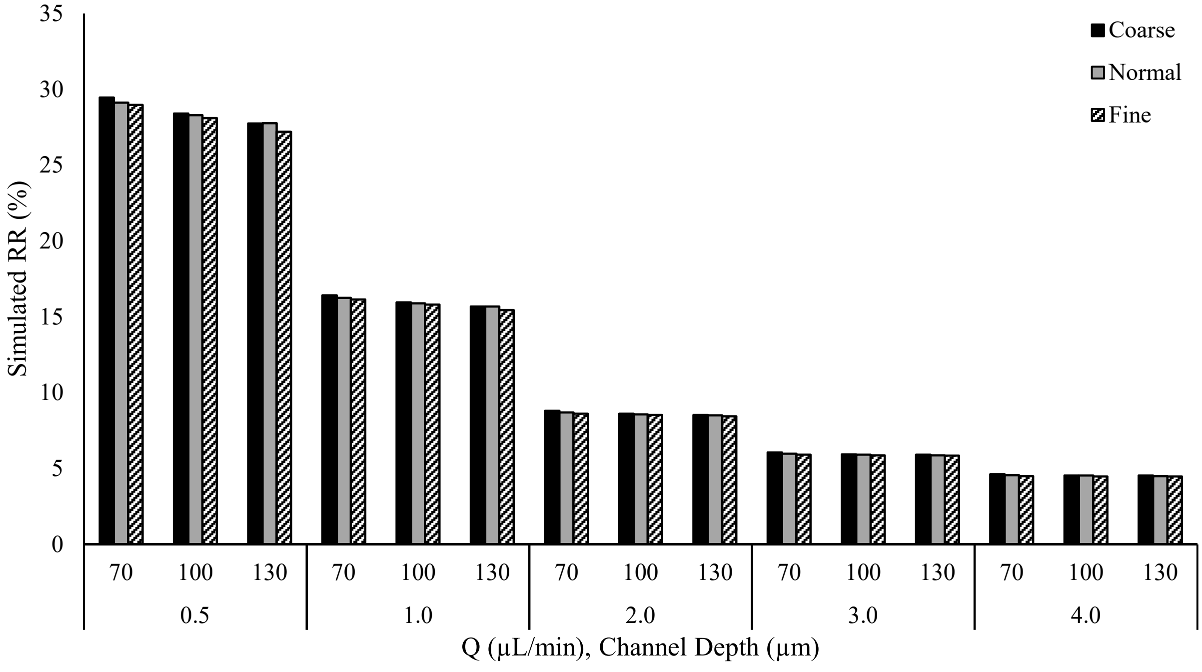

Figure 3.9. FITC-10 *RR* at multiple flow rates and channel thicknesses for a SLL350 device at COMSOL mesh density settings of coarse, normal, and fine.

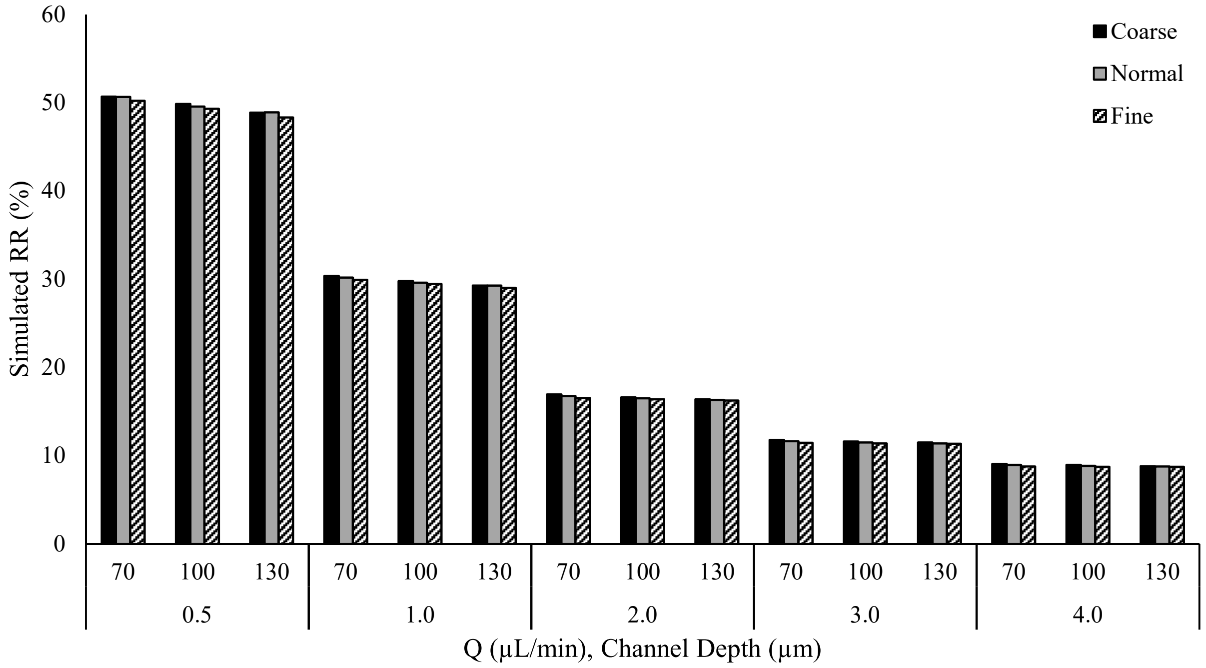

Figure 3.10. FITC-10 *RR* at multiple flow rates and channel thicknesses for a DLL350 device at COMSOL mesh density settings of coarse, normal, and fine.

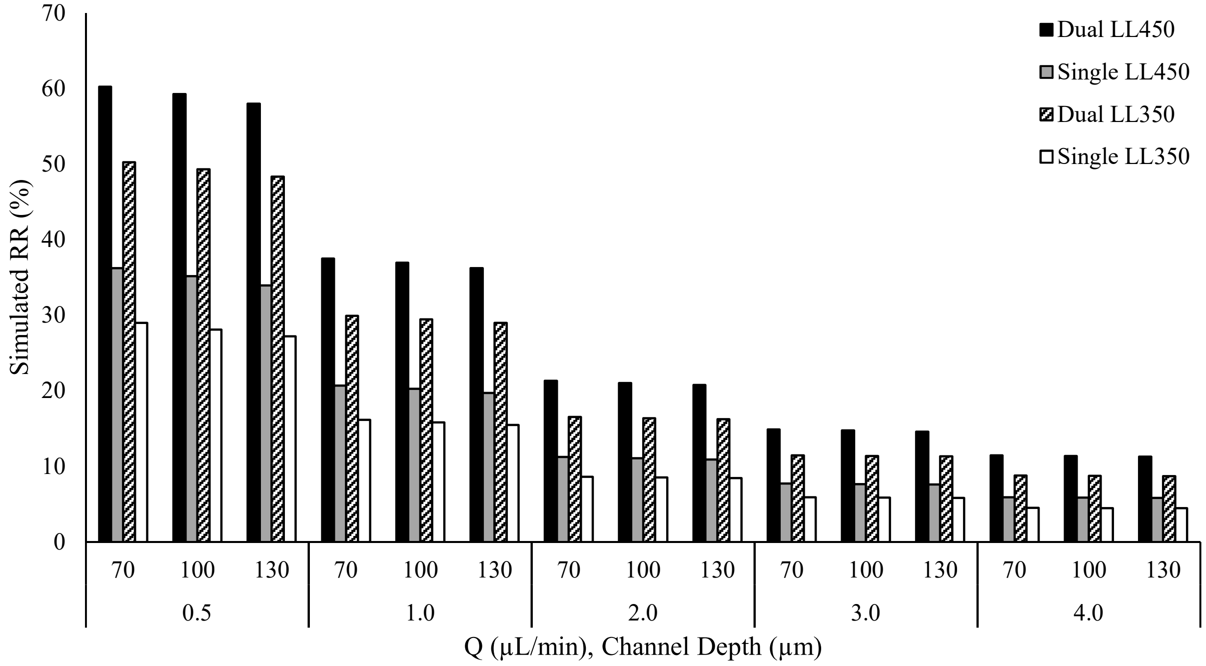

Figure 3.11. FITC-10 *RR* comparing single and dual membrane configurations for LL350 and LL450 devices using a fine mesh density.

Figure 3.6 gives the comparison of the LL devices presented in Table 3.1 and Figure 3.4. The LL450 design was shown to have a simulated relative RR increase compared to the CMA 20 ranging from of 16.1% at 0.5 µL/min to 54.7% at 4.0 µL/min (32.8 ± 16.8%); and an absolute RR increase of 8.2% to 3.9%, respectively at the same flow rates (5.8 ± 2.9%).

The maximum absolute difference in RR when comparing coarse to fine meshes was 0.57% at 130 µm channel depth, and 0.5 µL/min Flow rate. This was considered to be negligible and, therefore, showed no improvement in accuracy when using a denser mesh for this geometry type. An inconsistent stabilization factor of 0.0025 was used for all models to prevent solution failures as discussed in Section 2.5.1. Channel thicknesses were based off of a novel geometry to be presented in Chapter 4, where total channel depth varied from 70 to 130 µm and 100 µm. The 100 µm channel depth was the standard fabrication thickness as previously investigated by Randy Espinal Cabrera, and the maximum thickness of SU-8 3050 photopolymer used in both Randy's work and this research as described later in Section 3.8.

3.6.1 Linear Channel Mesh Density

The mesh density of the LL µF µD devices were considered to ensure COMSOL was calculating advection and diffusion outside of an experimental comparison of model vs. a fabricated device. The problem considered was that the mesh might not be sufficiently dense to properly calculate the changes in flow vectors between any two points on a mesh. This was not a problem for the CMA 20 device except for in the inner-cannula. The LL devices also used an inconsistent stabilization factor (c_{art}) of 0.0025 in-order to solve without the simulation failing; which was only 1/100 of the default c_{art} of 0.25. It is common practice to decrease the mesh density in situations where the change (slope) between two points is large, and not doing so can cause the solution to fail. If the flow is not properly being calculated, then diffusion will also not be calculated correctly and, subsequently, RR will be incorrect. Figure 3.7 to Figure 3.11 highlight a verification that increasing the mesh density from coarse to fine had no impact on RR for simple LL type geometries for multiple flow rates, channel thicknesses, diffusion sources, and channel widths.

3.6.2 Reynolds and Péclet Number Comparison for Linear Looped Devices

In fluid dynamics, the hydraulic diameter D_H is used as the characteristic length for calculations when the channel geometry is not cylindrical. For pipe flow, the characteristic length is given by the diameter of the pipe.[49] Due to limitations presented by soft-lithography fabrication, most channels are rectangular, and a different method of calculating the characteristic length was required.[21,28] The Re and Pe numbers were calculated using both hydraulic diameter D_H and channel thickness t_m as the characteristic length L for comparison purposes. D_H is defined as a ratio of fluid cross-sectional area A, and fluid perimeter P in Equation 3.2.[21,50] A visual depiction of these parameters is given in Figure 3.12 for different geometries. The calculations for area and perimeter are done using normal geometric shape equations for areas and perimeters.

$$D_H = \frac{4A}{P} \qquad \text{(Equation 3.2)}$$

For LL devices, D_H is not equal to the channel thickness of 100 µm and was calculated to be 142.8, 155.5, and 163.6 µm for channel widths of 250, 350, and 450 µm, respectively. Table 3.2 and Table 3.3 give Re and Pe numbers for $L = D_H$. Table 3.5 and Table 3.6 use $L = t_m$. Table 3.7 gives the average linear velocity and residence times, respectively.

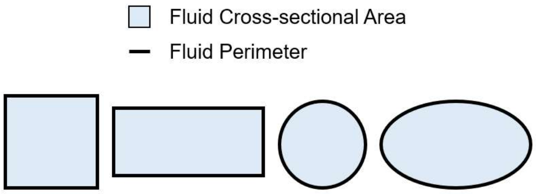

Figure 3.12. Fluid cross-sectional area and fluid perimeter for different geometries (square, rectangle, circle, and oval).

For this research, the use of D_H for L was thought to be incorrect, or not account for all properties of diffusion in a 3D domain when calculating Pe (Section 3.7 discusses the reasons for this implication). In the case of the CMA 20, D_H was equivalent to the channel (annulus) thickness. However, this was not the case for any of the LL devices as previously calculated. Accordingly, RR for CMA 20, LL350, and LL450 was 51.04%, 49.32%, and 59.29%, respectively; while the Pe numbers were 331, 491, and 401 using D_H, and 331, 315, and 245 using the channel thickness, respectively for both. Neither using D_H or channel thickness fully accounted for relating Pe to RR even though RR is primarily a function of residence time. This could be seen as the Pe was lower for the LL350 (315) while having lower slightly lower RR (49.32%) vs. the CMA 20 (331, and 51.04%, respectively) when using the channel thickness. It could also be seen when using the D_H for both the LL350 and LL450 devices with higher Pe numbers of 491 and 401, respectively; and each having RR close to or greater than the CMA 20.

Table 3.2. Calculated Reynolds numbers using hydraulic diameter.

	CMA 20	LL250	LL350	LL450
Q (µL/min)		Re		
0.5	0.021	0.054	0.042	0.034
1	0.041	0.107	0.083	0.068
2	0.083	0.214	0.166	0.136
3	0.124	0.321	0.250	0.204
4	0.165	0.428	0.333	0.272

Table 3.3. Calculated Péclet numbers using hydraulic diameter.

	CMA 20	LL250	LL350	LL450
Q (µL/min)		Pe		
0.5	331.1	631	491	401
1	662.3	1261	981	803
2	1324.5	2523	1962	1605
3	1986.8	3784	2943	2408
4	2649.0	5046	3924	3211

Table 3.4. Calculated Reynolds numbers using channel thickness

	CMA 20	LL250	LL350	LL450
Q (µL/min)		Re		
0.5	0.021	0.037	0.027	0.021
1	0.041	0.075	0.054	0.042
2	0.083	0.150	0.107	0.083
3	0.124	0.225	0.161	0.125
4	0.165	0.300	0.214	0.166

Table 3.5. Calculated Peclet numbers using channel thickness

	CMA 20	LL250	LL350	LL450
Q (µL/min)		Pe		
0.5	331.1	442	315	245
1	662.3	883	631	491
2	1324.5	1766	1261	981
3	1986.8	2649	1892	1472
4	2649.0	3532	2523	1962

Table 3.6. Calculated fluid residence times.

	CMA 20	LL 250	LL 350	LL 450
Q (µL/min)		Residence Time (s)		
0.5	91.9	60.0	84.0	108.0
1	46.0	30.0	42.0	54.0
2	23.0	15.0	21.0	27.0
3	15.3	10.0	14.0	18.0
4	11.5	7.5	10.5	13.5

Table 3.7. Calculated fluid average linear velocity

	CMA 20	LL 250	LL 350	LL 450
Q (μL/min)	U (mm/s)			
0.5	0.11	0.33	0.24	0.19
1	0.22	0.67	0.48	0.37
2	0.44	1.33	0.95	0.74
3	0.65	2.00	1.43	1.11
4	0.87	2.67	1.90	1.48

3.7 Surface Area to Volume and Perimeter to Cross-sectional Area Ratios

The simplification of RR cannot always be reduced to a 2D problem in cases where the membrane surface in contact with the fluid contains additional vectors. The Pe number only compares the characteristic rates (average fluid velocity, diffusivity) over a characteristic length. It does not account for the change in diffusive flux as the channel geometry was static and replaced the walls with membranes (diffusion sources). In this case, there are multiple characteristic lengths for a single point in the fluid pertaining to diffusion only. This would effectively reduce the Pe as additional characteristic diffusion lengths reduce the overall restriction to diffusive mass transport in a channel; if the Pe number was sufficient to describe the additional diffusion sources. A reduced Pe will yield an increase in RR as diffusion is more dominant.

Membrane surface area to volume ratio was investigated in order to determine the effect of additional characteristic diffusion lengths have on RR. Surface area to volume ratio was reduced to perimeter to cross-sectional area as this is constant for the full length of the channel. Accordingly, four device geometries were simulated with the primary restriction being the membrane perimeter to fluid cross-sectional area (M_P/C_A) was restricted to 0.01, 0.02, 0.03, and 0.04. All models used a 0.5 mm channel length and the FITC-10 aqueous ($7.55 \cdot 10^{-7}$ cm^2/s) and

CMA 20 membrane ($2.55 \cdot 10^{-7}$ cm^2/s) diffusion coefficients. All membranes were 50 µm thick to match the 2015-2018 CMA 20 dimensions. The inlet boundary condition was set to an average velocity of 0.109 mm/s (equivalent to the annulus average velocity of a CMA 20 at Q = 0.5 µL/min. The application of a constant fluid velocity allowed for the comparison of diffusion and channel geometry without having to consider the effects of changing fluid velocities. Figure 3.13 A to D shows a linear channel with 100 µm depth and width and increasing the membrane surface area by adding a membrane on each side one at a time (1-side on A to 4-sides on D).

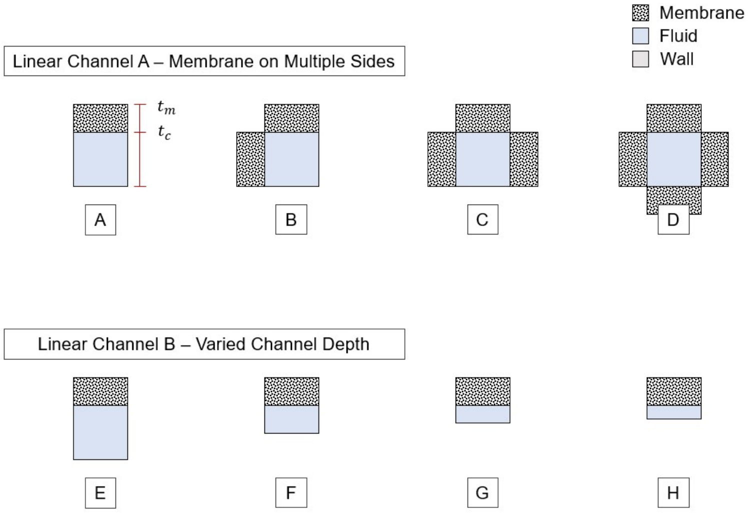

Figure 3.13. Linear channel cross-sections and membrane surface area.

This initial simulation served as the starting point for restricting all of the following simulations to the aforementioned M_P/C_A ratios. Figure 3.13 E to H shows reducing channel depths from 100 µm (E), 50 µm (F), 33.33 µm (G), and 25 µm (H) to match the M_P/C_A ratios from A to D. Figure 3.14 I to L shows a simple cylindrical geometry with no inner cannula. This is representative of linear probes available from Harvard Apparatus (CMA 30, CMA 31) where the membrane acts as the fluid channel. Channel depths are equivalent to the diameter at 400 µm (I), 200 µm (J), 133.34 µm (K), and 100 µm (L). Figure 3.14 M to P uses the same geometry form factor as the CMA 20 where there is an inner cannula. Channel depths are equivalent to the annulus depth ($r_a - r_c$) of 160 µm (M), 72 µm (N), 46 µm (O), and 32 µm (P). All device dimensions and M_P/C_A ratio for Figure 3.13 and Figure 3.14 are summarized in Table 3.8.

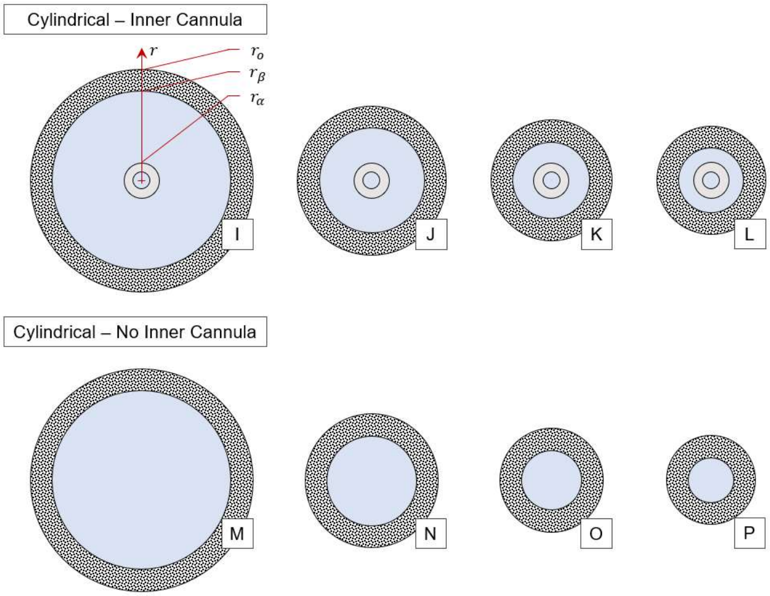

Figure 3.14. Cylindrical channel cross-sections and membrane surface area.

Figure 3.15 depicts a simplified example of increasing overlapped diffusion lengths using linear channel A from Figure 3.13 A to C. It should be noted that overlapping diffusion lengths do not increase RR by a multiple of the lengths due to RR being driven by a concentration gradient and flux decreases as gradient decreases (Equation 2.3 in Section 2.1). Figure 3.16 and Figure 3.17 show RR vs. M_P/C_A. Linear channel A represents the constant channel dimensions as shown in Figure 3.1 A to D where a membrane was added to each side. Linear channel B represents a decreasing channel depth as shown in Figure 3.1 E to H.

Table 3.8. Membrane surface area to fluid perimeter device dimensions.

			Channel		Membrane	Fluid	Membrane + Fluid
Model	Figure Index	Membrane Sides	Depth (μm)	Width (μm)	Surface Perimeter (μm)	Area (μm^2)	Area (μm^2)
Linear Channel A	A	1	100	100	100	10000	40000
	B	2			200		
	C	3			300		
	D	4			400		
Linear Channel B	E	1	100		100	10000	15000
	F	1	50		100	5000	10000
	G	1	33.33		100	3333	8333
	H	1	25		100	2500	7500
			r_b (µm)				
Cylindrical (No Inner Canula)	I	1	200		1257	125664	196350
	J	1	100		628	31416	70686
	K	1	66.67		419	13963	42761
	L	1	50		314	7854	31416
			$r_a - r_c$ (µm)	r_c (µm)			
Cylindrical (Inner Canula)	M	1	160	40	1257	120637	196350
	N	1	76	40	729	37247	86570
	O	1	46	40	540	18209	58107
	P	1	32	40	452	11259	46759

Linear channel A had higher RR ranging from 3.0% to 10.5% vs. linear channel B with 3.0% to 8.8% for M_P/C_A increasing from 0.01 to 0.04, respectively. This was due to the additional diffusion vectors which overlap ratio. Each side of linear channel A had an additional surface diffusion source overlapping the same volume. linear channel B only decreased the channel depth; shortening diffusion lengths. In other words, there was more mass flux from the channel walls due to increased surface area on linear channel A compared to B. This is shown by comparing linear channel A and B with RR of 10.5% and 8.8% for a M_P/C_A of 0.04, respectively. However, the increase in RR for linear channel A with a membrane on 1-side vs. 4-sides was 3.0% to 10.5%, or approximately a 3.5x increase. A decrease in diffusion lengths (linear channel B) from 100 µm to 25 µm (3.0% to 8.0% RR) resulted in approximately a 2.9x increase.

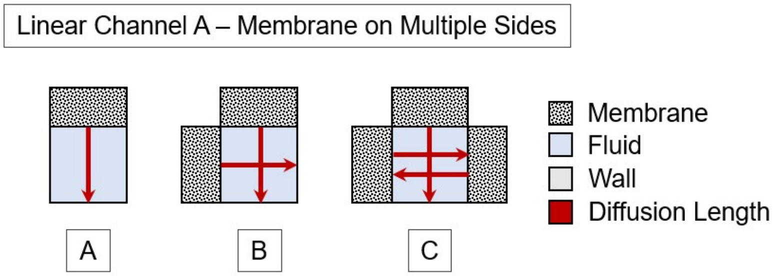

Figure 3.15. Overlapping diffusion lengths in linear channel A.

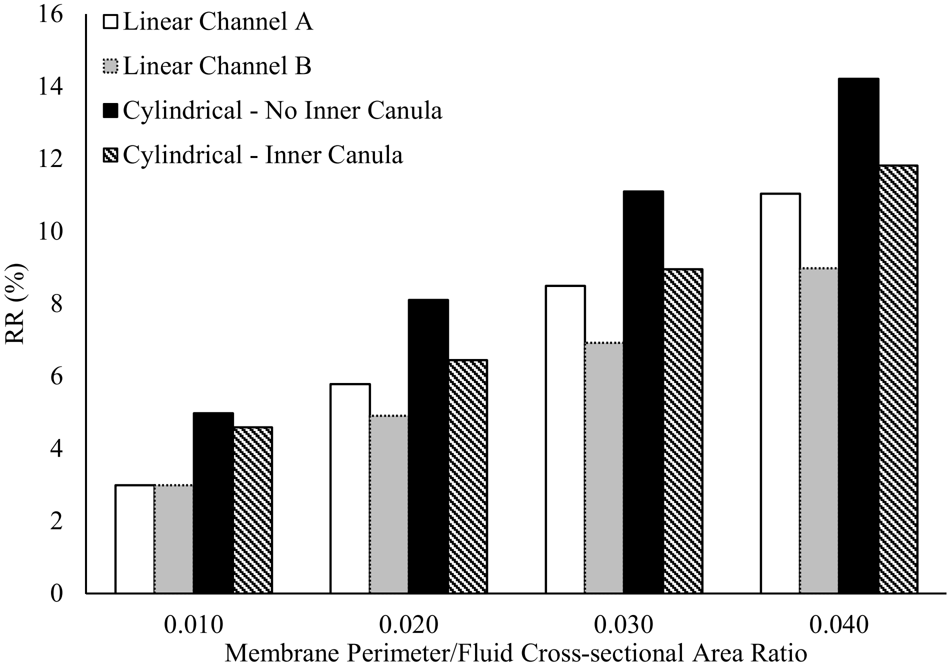

Figure 3.16. Comparison of reduced diffusion lengths through increasing membrane surface area (as perimeter) vs. decreasing channel depth with a fixed membrane surface area at constant average linear velocity.

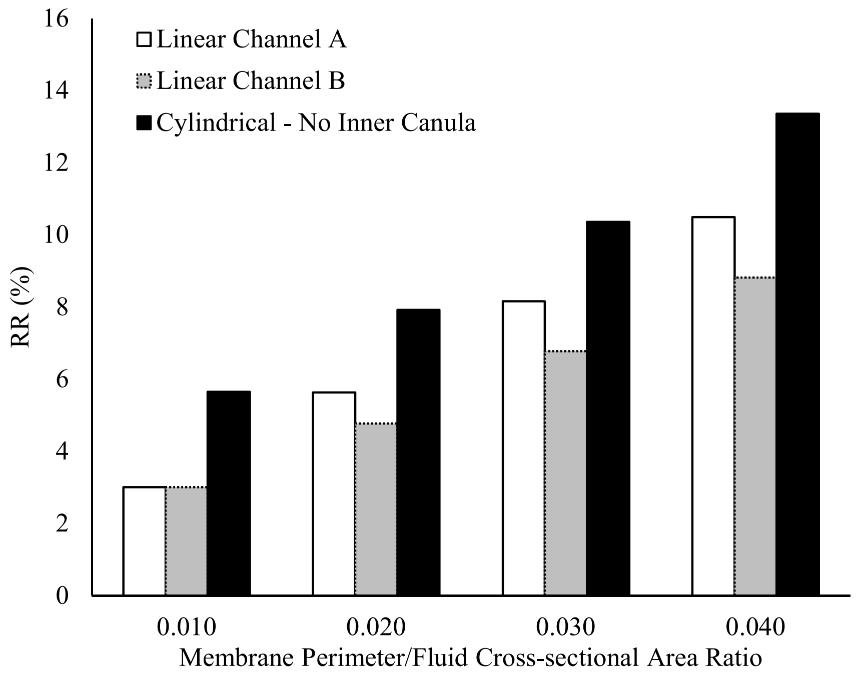

Figure 3.17. Zoom of data from Figure 3.16 excluding cylindrical with inner cannula geometry.

All RR vs M_P/C_A ratio comparisons in this section should only be considered for comparing diffusion. Some of these geometries would not be appropriate for increasing RR due to the sample volume and resulting flow rate requirement which would alter the linear velocities depending on the cross-sectional area of the channel. A smaller cross-section at a constant flow rate would increase the overall linear velocity as defined by $Q = UA$. This is why the linear channels as described previously in Section 3.5 outperformed the cylindrical geometry with 59.29% vs. 51.04% RR at 0.5 µL/min, respectively. The addition of overlapping diffusion vectors is also shown when comparing the RR for a LL450 in DLL vs SLL configurations with 59.29% vs. 35.18% at the same 0.5 µL/min. A ~1.69x increase similar to the 1.59x increase shown in linear channel A. The reason for this difference was the concentration gradient was different at the walls of the channels (Figure 3.18). In a pseudo infinitely wide channel, the concentration gradient near the wall becomes negligible.

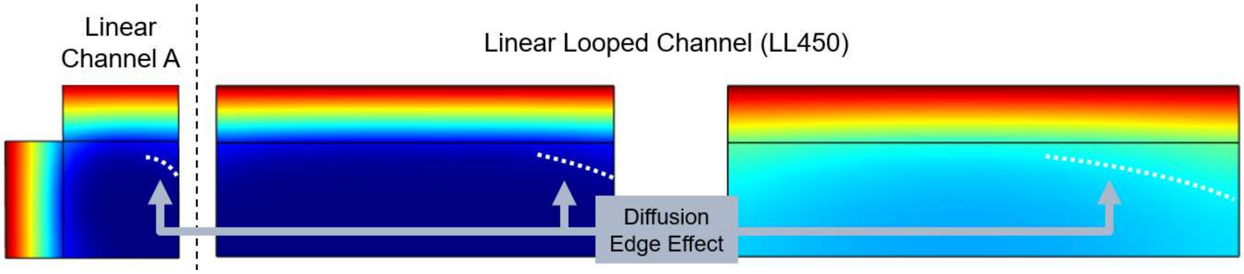

Figure 3.18. Diffusion edge effect in Cartesian linear channels.

Continuing, for any channel under experimental, the cross-sectional area at a constant flow rate alters the linear velocity of the fluid, and subsequently, RR. Using this information, and Table 3.8, while holding the M_P/C_A constant and finding the geometry with the highest fluid cross-sectional area, the highest RR could be obtained for a constant flow rate. This, in turn, makes the linear channel with no inner-cannula or other possible structures the most space efficient geometry while producing the highest RR. The advantages of the overlapping diffusion vectors and short diffusion lengths produced by the cylindrical geometry with the inner cannula are gone because the linear velocity at the same flow rate is significantly higher due to lower cross-sectional area for the fluid to traverse (reducing fluid residence time). Figure 3.19 gives RR for linear channel and cylindrical geometries at different M_P/C_A ratios and a constant inlet flow rate of 0.5 µL/min. The only difference in the simulation as shown previously in Figure 3.16 was the volumetric flow rate as an inlet boundary condition. All models in Figure 3.19 show decreasing RR as channel depth was decreased and fluid linear velocity increased.

It was unclear whether or not the cylindrical model with no inner cannula would outperform the linear channel A model given the same fluid cross-sectional area and ignoring the constraints as they were similar with the exception of the cross-section geometry and resulting velocity gradient.

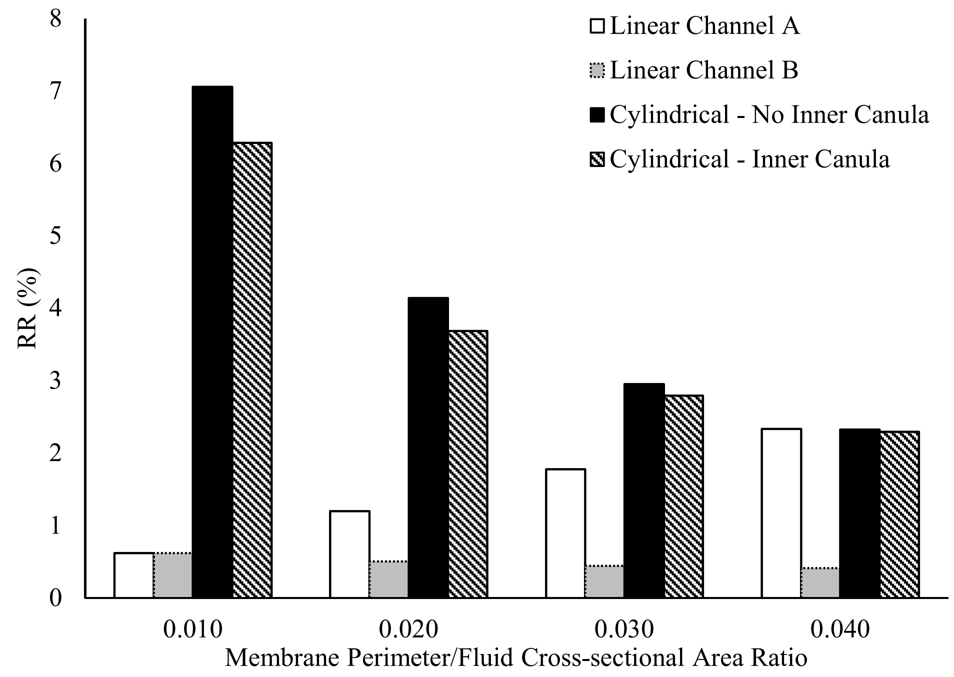

Figure 3.19. Comparison of reduced diffusion lengths through increasing membrane surface area (as perimeter) vs. decreasing channel depth with a fixed membrane surface area at constant inlet flow rate.

3.8 Fabrication and Characterization of Linear Looped Microfluidic Microdialysis Device

A microfluidic microdialysis device was fabricated using soft-lithography and characterized based on the linear looped design shown in Chapter 3. Soft-lithography presents the opportunity for rapid development of new design options for MF devices.[29] Commonly available photolithographic tools were used to create a physical template (SU-8 master) of a microfluidic channel. A silicone-based polymer was molded on the channel, removed, and a membrane was attached to create a microfluidic microdialysis device.

3.9 Device Fabrication

Standard soft-lithography was used to fabricate polydimethylsiloxane (PDMS) channel replicas. 100 µm thick SU-8 3050 (MicroChem) was spin coated onto a silicon wafer and exposed to UV-light under a photomask according to the manufacturer's guidelines.[51] Photomasks (Fineline Imaging, Colorado Springs, CO) were designed in Autodesk Fusion 360 and Autodesk AutoCad. The same files were used for linear-looped devices when generating geometry in COMSOL using the dxf file import option.

Membranes were fabricated using the phase inversion method. Polyethersulfone (PES) (Ultrason E 6020 P) was dried in an oven at 70 °C for 24 hours. Then the PES was added to 40,000 g/mol polyvinylpyrrolidone (PVP) (Tokyo Chemical Industry) and both were dissolved in N,N-dimethylacetamide (DMAc) (Alfa Aesar) using a 16/16/68 w% ratio, respectively. Membranes were cast to 30 µm using a micrometer adjustable film applicator (doctor blade, MTI Corp) on a glass plate. The glass plate was submerged in a deionized water bath. The membrane was removed after 1 hour and stored in a separate deionized water container. Membranes were measured to be 60 µm at the edge when wet using a digital caliper.

Membranes were removed from storage completely dried prior to attachment to the PDMS channel replica. Both PDMS replicas and membranes were bonded together using plasma oxygen ashing and 3-aminopropyltriethoxysilane (APTES) chemistry as described by Aran et al.[52]

3.10 Device Characterization and Comparison with CMA 20

The linear-looped microdialysis device fabricated in Section 3.9 was used to collect caffeine as shown in Figure 3.20 below. RR decreased from 40.7% at 0.5 µL/min to 8.4% at 4.0 µL/min. It is important to note that the fabricated device performance does not match the CMA 20 RR for either caffeine or vitamin B-12 due to the membrane used for fabrication. It could be considered impossible to perfectly replicate the membrane on the commercial CMA 20 μD probe for a direct comparison between devices and simulation data for the following reasons.

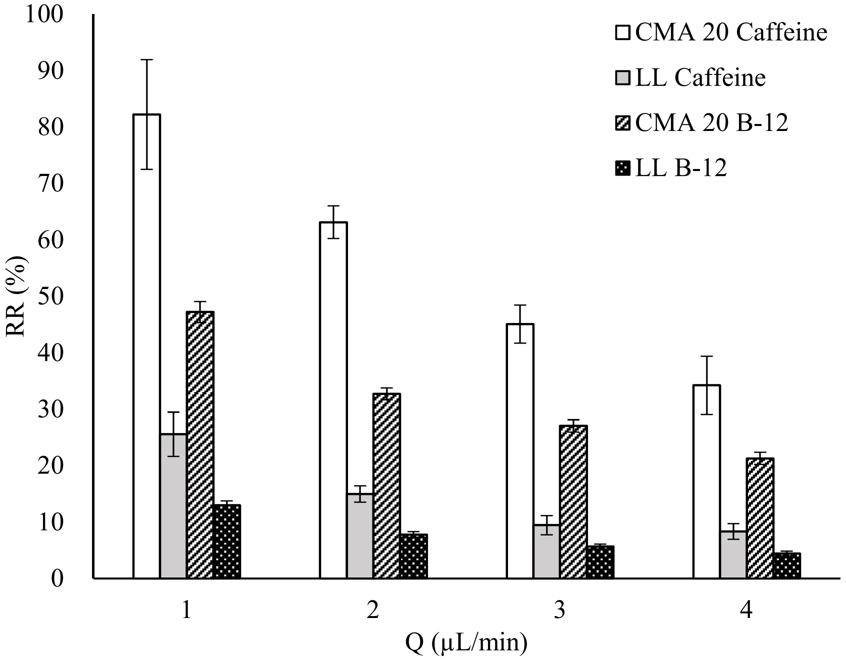

Figure 3.20. Experimental *RR* for an in-house fabricated linear looped microdialysis device with 350 μm inlet and 450 μm outlet, and in-house made polyethersulfone flat-sheet membrane.

There was a significant difference in membrane geometry and fabrication techniques. The membrane used on the LL device as tested in Figure 3.20 was a flat-sheet membrane placed on top of a μF channel, and the CMA 20 membrane was cylindrical. This basic difference in geometry requires very different fabrication tools with similar functions. The flat-sheet membrane was formed initially in open air using a thin-film applicator (also known as a doctor's blade) which set the pre-phase inversion thickness of the membrane. The flat-sheet membrane was then placed in a coagulation bath where the phase separation occurred to form the final membrane. In a cylindrical device, the polymer-solvent mixture exits an annulus shaped nozzle extruding as a continuous cylinder or ring. The external and internal conditions of this extruded ring can be varied with different non-solvents to achieve different phase separation effects above and beyond that of just varying the ratio of polymer, solvent, and pore-forming agents. The ability to control the phase inversion process on the internal and external membrane surfaces allowed for different optimizations to be formulated. This was difficult to achieve for flat-sheet membrane fabrication and was outside of the capabilities of this lab for this research. Finally, the finer details for the method used to fabricate the commercial CMA 20 membrane were proprietary information at the time of this research. The primary challenge going forward is to investigate different flat-sheet membrane fabrication variables to improve the membrane diffusion coefficient without any fluid-loss through the membrane pores.

3.11 Conclusion

A linear-looped channel geometry was designed and simulated using the research presented in Chapter 2 where a model was created using a commercial microdialysis probe as the baseline. Important concepts for understanding advection diffusion in different dimensions (1D-4D) and the relationship with the Pe number were defined and discussed (Sections 3.1, 3.2, and 3.3). These concepts were then applied toward designing a linear-looped device geometry in similar dimensions to a CMA 20 microdialysis probe and then simulated for comparison (Section 3.6). The linear-looped device geometry was investigated for RR and the effects of different mesh densities (coarse, normal, and fine) used in COMSOL. The linear-looped device with a 350 μm inlet, 450 μm outlet, 100 μm channel depth, and 97% of the total device cross-sectional area was able to achieve a 16.1% relative increase in RR compared to the CMA 20 microdialysis probe at 0.5 μL/min. This increase showed that a microfluidic-based microdialysis device could be designed to exceed the commercial CMA 20 performance. The dimensional-based variables discussed in Sections 3.1, 3.2, and 3.3 were further investigated toward understanding multiple diffusion vectors or membrane perimeter to fluid cross-sectional area (Section 3.7). It was found that increasing the ratio of membrane perimeter to fluid cross-sectional area increased overlapping diffusion vectors and, therefore, increased RR beyond that of what the Pe number described based on a single 1D vector.

A linear-looped device was fabricated using soft-lithography, and an in-house fabricated PES membrane using phase inversion (Sections 3.8, 3.9, and 3.10). It was found that the fabricated device was not currently competitive with the CMA 20 and did not match simulation data. This was due to the differences between the in-house fabricated membrane and the CMA 20 membrane. Further work needs to be competed toward increasing membrane diffusivity for in-house fabricated membranes. Overall, the parameters for designing a microfluidic microdialysis device with maximum diffusive transport based on length scales and geometry without affecting fluid flow was successfully defined.

Chapter 4. Microdialysis Microfluidic Herringbone Mixer

4.1 Introduction to Microfluidic Mixing

Previously, in Chapter 3, optimizing surface area to volume ratio and characteristic diffusion lengths was discussed as a method to improve microdialysis RR by changing the basic channel geometry. While successful, these optimizations were ultimately limited by the diffusivity of the molecule and the fluid velocity as described by the Pe number (Equation 3.1). While it was possible to mitigate some limitations presented by the diffusion coefficient by increasing the membrane surface area to fluid volume ratio, the fact remained that diffusion was still limited by the linear velocity (or residence time) of the fluid. Fick's law (Equation 4.1) describes the random walk of a molecule through a fluid, and how that direction is on average in the direction of the concentration gradient. In Equation 4.1, J is the flux, D is the diffusion coefficient, and C is the concentration of the diffusing analyte over a characteristic length x.

$$J = -D\frac{dC}{dx} = -\frac{D}{x}(C_0 - C_1) \qquad \text{(Equation 4.1)}$$

The right-hand side of Equation 4.1 is a simplification defining the flux over a short distance where C_0 and C_1 are the concentrations at each end of the gradient along x. Accordingly, the path of diffusion is continuous and does not jump from one point to another to accelerate the diffusion process. In other words, there is turbulent flow in microfluidic devices, and all processes are diffusion limited.

This diffusion problem is well known in the microfluidics community and the lack of turbulences is due to the length scale at which the fluid is being manipulated. The microfluidic flow regime, or laminar flow, is described by the Reynolds number (Equation 4.2) as the ratio of fluid density (ρ), average linear velocity (U), and characteristic length (L), over the dynamic viscosity (μ). It is essentially a ratio of fluid momentum ρUL in comparison to fluid viscosity (μ) (or molecular diffusion). This ratio defines the strength of two forces in comparison with each other and is a cornerstone of how microfluidics works. Laminar flow is limited to $Re < 2000$ and anything greater is considered turbulent flow. Other values ranging from 1900 to 2300 have been reported depending on the source.

$$Re = \frac{\rho UL}{\mu} \qquad \text{(Equation 4.2)}$$

The reason flow is laminar at microfluidic length scales (< 1 mm) is due to the amount of mass moving through the channel, and the rate at which it is moving. Density and viscosity are constant unless there is a temperature change. For this research, the temperature ranges of interest were from 25 °C (room temperature, μ = 0.89 mPa·s) to 37 °C (body temperature, μ = 0.69 mPa·s) in water.[40,45] In the case of µD and many other related µF applications, Re is commonly less than 1 as previously shown in Section 3.6.2, and is a review on passive mixing in microfluidics by Lee et al.[33] Under these conditions, fluid will conform to the shape of the channel, and movement of molecules within the fluid dominantly depends on diffusion (viscous or molecular). Again, in other words, there is no mixing or turbulence. At Re greater than 10, the effects of momentum start to appear in what are known as Dean flows where the fluid will twist around turns as the result of higher momentum.[33] The higher momentum is required to get the fluid to self-mix. The twisting of fluid is one of the most common ways to induce fluid mixing as it alters diffusion lengths within the fluid. This twisting motion can result in the folding of the fluid in the same way as a towel or blanket are folded.

For over 20 years, microfluidic mixing methods have been widely used a fluid twisting and folding method known as passive mixing.[31–33,53] The focus of this research was to implement passive mixing by altering channel geometry only (no moving parts or extra components as needed with active pump-based or electroosmotic mixers). Passive mixer geometries incorporate t-channel, serpentine, grooves, splits and recombination, and intersections in 2D and 3D formations to induce this folding effect.

The most basic underlying mechanism of the fluid folding is known as a Baker's transformation (Figure 4.1) as derived mathematically and conceptually by Wiggins and Ottino.[30] Every mixer alters the length scales at which diffusion occurs by altering the flow of the fluid. This is advantageous as the fluid linear velocity in a microfluidic channel was on the order of approximately mm/s at the Re in this research; whereas, the diffusion coefficient ranged three orders of magnitude slower and more ($\leq 10^{-6}$ cm^2/s). Figure 4.1 steps 1-5 depict the Baker's transformation, which is a repetitive stretching and folding of two different adjacent domains.

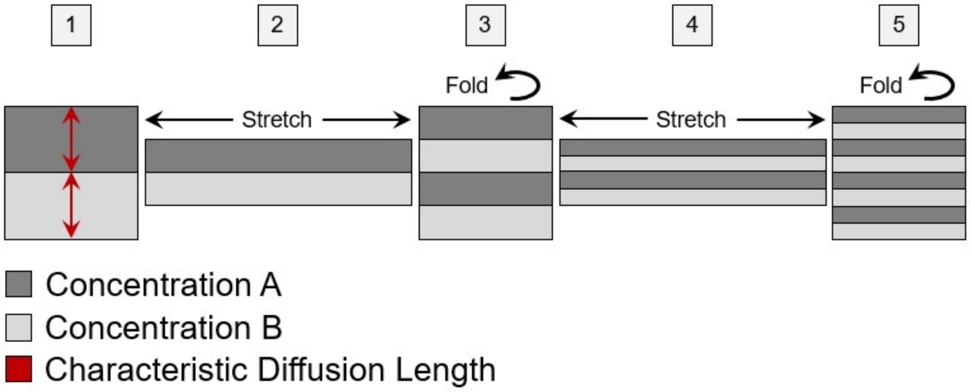

Figure 4.1. Baker's transformation flow diagram.

As each domain is stretched, it becomes thinner. The folding of each domain creates a sandwich-like structure with increasing alternating domains as more folding and stretching occurs. In microfluidic mixing, the domains are two fluids of different concentrations (A and B, Figure 4.1). The previously listed methods of passive microfluidic mixing incorporate different geometries to induce this stretching and folding effect as the fluid moves through the channel. Each fold reduces the diffusion distance and, subsequently, time required for an analyte to diffuse from one fluid region to another by a factor of one half. The entire process is analogous to kneading dough. The repeated stretching and folding of the dough as more ingredients are added, such as flour, is the only way to get the components to mix.

Microdialysis, and all other mass transport phenomena, contain what are called boundary layers. These layers exist as mathematically defined interfaces at which a specific condition changes such as the distance a concentration of molecules has diffused and, after this distance, there is zero concentration. Many different boundary layers exist such as pressure, density, velocity, and temperature.[19–21] This research focuses on the concentration boundary layer (CBL) that develops inside a microfluidic channel in a fluid moving tangential to concentration source at a membrane surface. Figure 4.2 depicts a representative CBL in a microfluidic channel at different linear velocities (v). The left side depicts a comparison of the CBL for two different parabolic velocity profiles for different linear velocities where $v_1 < v_2$. The distance the CBL extends into the microchannel is shorter at higher linear velocities. The right side shows the decreasing thickness of the CBL as fluid linear velocities increase. For all sides, the red line represents the maximum distance a diffusing analyte has traveled into the microchannel. The CBL becomes smaller as linear velocity increases since the fluid is carrying away diffusing analyte, and not allowing it to diffuse further into the fluid. Microdialysis RR is limited by the

CBL according to the advection-diffusion equation (Equation 2.3), which is a modification of the diffusive flux equation (Equation 4.2), to include a fluid velocity term. Flux will increase at the interface as the CBL collapses (C_1 in Equation 4.2 decreases, or the gradient increases).

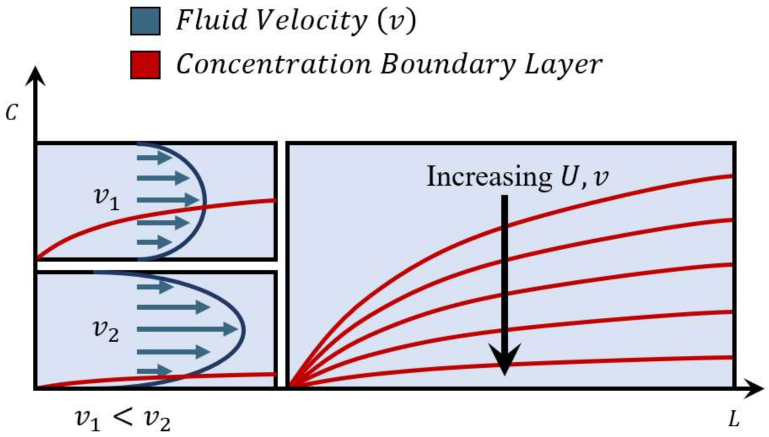

Figure 4.2. Depictions of the concentration boundary layer collapsing for different linear velocities (v_1, v_2). Increased average linear velocities U result in a thinner concentration boundary layer.

This is important as it shows that increased fluid velocity can increase diffusive flux at the membrane fluid interface; however, the limitation becomes a sample concentration problem as RR will decrease. Figure 4.3 depicts increasing mass recovery (MR) for caffeine due to the higher diffusive flux caused by the higher concentration gradient. While more analyte was collected, the total volume collected increased as well; therefore, decreasing the RR. Ideally, collapsing the CBL and increasing the concentration gradient at a constant fluid velocity would allow for increased RR. Microfluidic mixing methods present the ability to increase RR though additional velocity vectors not found in standard microfluidic channels. Laminar flow has a characteristic parabolic velocity profile where fluid moves in a straight line and does not deform with $v = 0$ (no slip) at the wall, and the highest v is at the center of the channel (Figure 4.2).

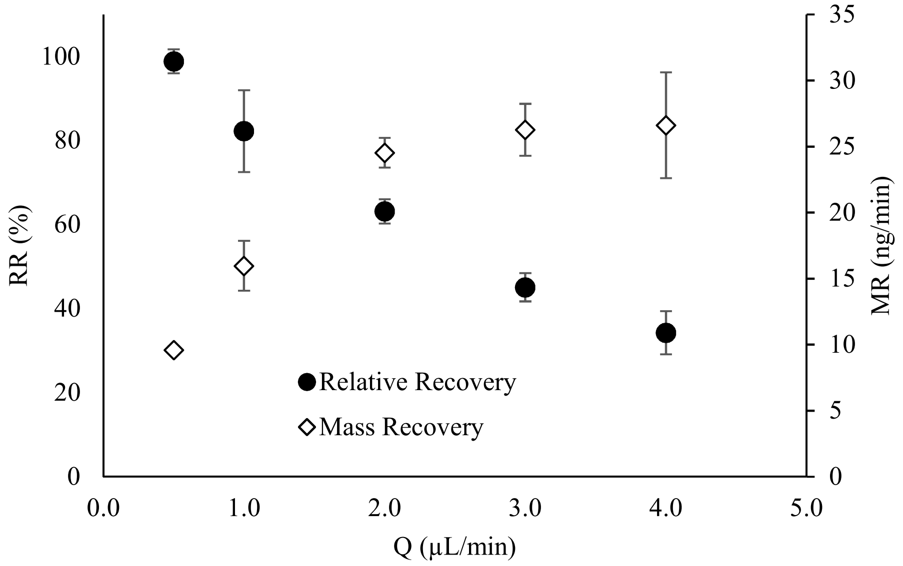

Figure 4.3. Caffeine relative recovery vs. mass recovery at different flow rates.

If fluid containing analyte diffusing in from a membrane surface can be folded or swept away from the surface in a direction not parallel to the flow; then diffusive flux can be increased while keeping the volumetric flow rate constant. This combines the benefits of MR with RR, simultaneously.

4.2 The Herringbone Mixer

In order to sweep diffusing analyte away from the membrane surface, the microfluidic mixer geometry known as a herringbone (HB) was investigated. The herringbone mixer (HBM) presents a channel geometry that continuously folds fluid in a twisting motion as it moves down the channel. Figure 4.4 shows a representative fluid streamline moving from the channel inlet and as it enters an HBM groove. The fluid rotates and subsequently folds over on itself repeatedly as depicted by the Baker's transformation (Figure 4.1). The HBM has been thoroughly investigated as far back as its inception in 2002 by Stroock in the Whitesides' group where it was described how grooves in the floor of a microchannel introduces transverse flows.[54,55] Transverse refers to flow not in the direction of the flow through the microchannel which is also referred to as tangent to the normal flow vector. Figure 4.5 extends on Figure 4.4 by defining additional fluid flow vectors for flows that are transverse or tangent (x and z) to the normal laminar flow vector (y). Representatively, vectors x and z correspond with the channel width and depth, respectively, while y corresponds to the channel length from inlet to outlet.

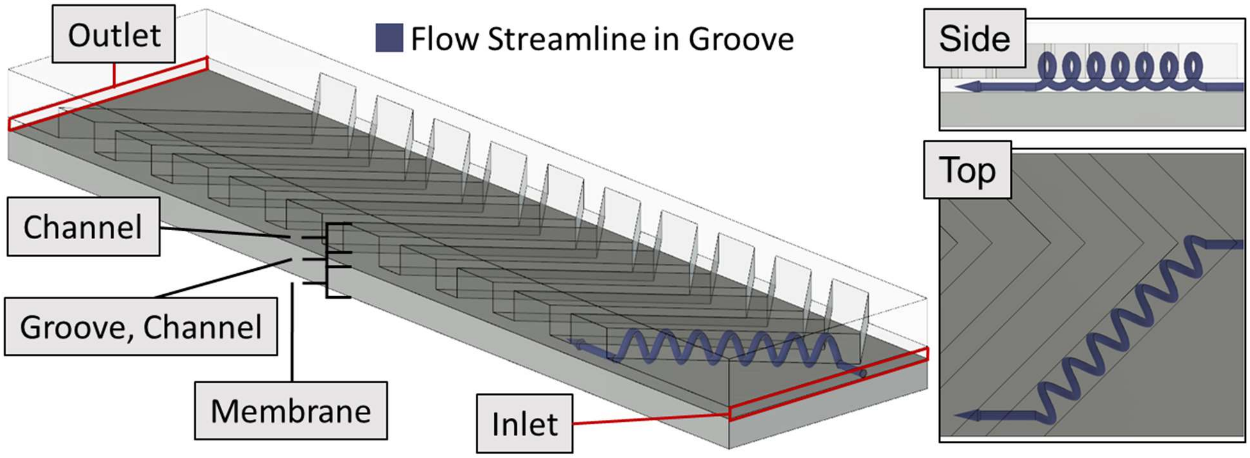

Figure 4.4. The herringbone microfluidic mixer geometry and fluid streamline. The right side illustrates the fluid folding over itself (side) and following along the chevron (top view)

Many other groups have investigated HB mixing from purely a performance and design standpoint. Bennet et al. used particle tracking in ANSYS, a fluid mechanics and chemical engineering simulation program, to evaluate mixing with different groove geometries and depths.[56] Stroock et al. developed an analytical model for HB mixing using lid-driven flow.[57] Hassell et al. expanded on Stroock's initial design by investigating flow patterns at low Re ($\leq$

15) using COMSOL; although no diffusion was accounted for in this model.

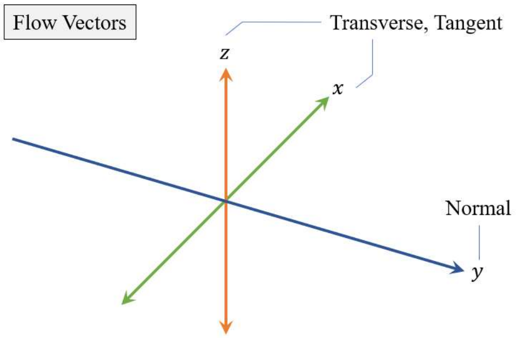

Figure 4.5. Fluid flow vectors for transverse/tangent and normal laminar flow.

Kee et al. used COMSOL and particle tracking at Re from 0.001 to 10 based upon Stroock's work.[58] Williams et al. from the Yager lab created a HBM guide used in the initial work of this research.[59] Multiple other groups investigated HB design simplifications, optimizations, convex groove geometries, further research into low Re mixing, and variations to groove dimensions.[35,36,38,60,61]

The particle tracking or tracing is a common method for evaluating mixing efficiency for micromixers such as the HBM. COMSOL implements a module dedicated to particle tracking to highlight its importance as a mixing evaluation method. Multiple authors cited the difficulties involved with numerically calculating diffusion. The problem is due to the mesh element size not being sufficiently small enough to resolve the true concentration gradient when the fluid folds repeatedly and the diffusion distance decreases as previously shown in Figure 4.2. Figure 4.6 depicts how insufficient mesh size and the diffusion distances can lead to discontinuity (inaccuracy) in the solution in the form of not resolving the correct concentration (C) from one point on the model to another (along a distance z). This figure is not part of any given model, but only representative of a pseudo mesh of triangular elements overlaying a pseudo concentration gradient. This depicts when the mesh resolution is not increased, the fluid folding can create small sharp concentration gradients that cannot be resolved accurately as the triangular elements which COMSOL calculates over exceed the size of the gradient. Figure 4.6 A1 and B1 are the concentration gradients overlaid with a representative triangular mesh commonly used in COMSOL. Figure 4.6 A2 and B2 are 2D line plots along the green lines on A1 and B1, respectively; whereas, the blue line is the simulated and the red line is the actual concentration. Figure 4.6 A1 has sufficient mesh size to resolve the concentration gradient as shown in A2 where the difference between the actual and simulated concentration is negligible.

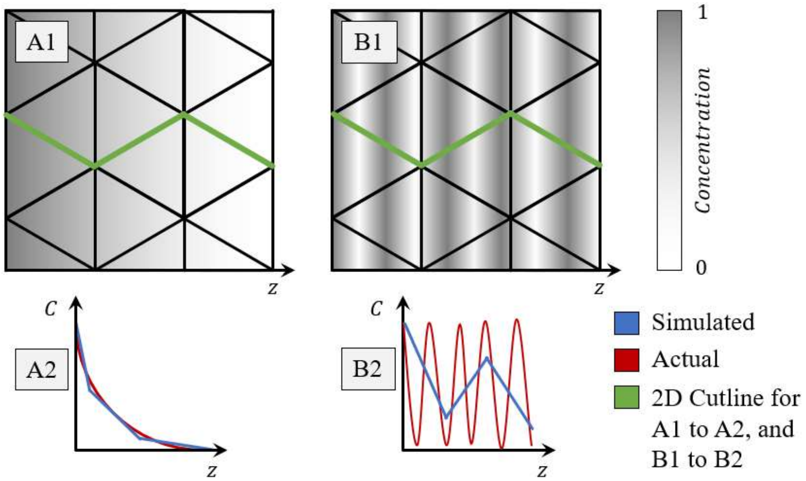

Figure 4.6. Mesh density vs. different concentration gradients. A1 is a single gradient. B1 is multiple gradients which cannot be computationally resolved due to being smaller than the mesh density.

Figure 4.6 B1 and B2 shows the same fluid as in A1 and A2, but after several Baker's transformation steps which make the concentration gradient smaller than the mesh element size. In that case, the gradient cannot be resolved accurately from one point on the mesh to another.

The simulated concentration (blue line) in Figure 4.6 B2 shows how the calculated concentration over and undershoots the actual concentration (red line). Section 4.5 will discuss simulation result comparisons in mesh quality for the HBM. Williams et al. showed the simulation deviating after 5.1 mm length vs. laser scanning fluorescent confocal data when using the diffusion module at Pe = 625.[59] It was also shown that the lower Pe made the model more inaccurate as models at Pe = 6250 and 62500 maintained accuracy with confocal results up to 8.5 mm, and the maximum shown of 11.9 mm channel length, respectively. All CMA and LL devices used in this research fall in the Pe to 3200 range.

Particle tracking alleviates this problem by allowing simulated particles to flow along the fluid stream lines and, therefore, reduces computational requirements used to model diffusion. The position of the particles in the fluid allows for mixing to be quantified using to inlet fluids containing tagged particles. This method assumes diffusion is negligible due to the difference in just rate alone (10x) between fluid velocity and diffusivity previously mentioned (v = mm/s and D = 10^{-6} cm^2/s) without accounting for the length scales involved using the Pe number (~30x minimum). There is a large difference between using diffusion between two inlet fluids or even particle tracing when a membrane is involved. The concentration boundary condition changes along the channel wall as a function of diffusive flux. Under unmixed laminar flows, diffusive flux changes along the length of the channel. When mixing using HB grooves, the flux is not the same at any point (all directions) on the membrane-channel interface due to the fluid rotation and HBM groove geometry.

4.3 Examples of Enhanced Mass Transfer through Mixing

Ultimately, the goal of this chapter is to show how mixing can disrupt the CBL, and increase RR beyond optimizing device dimensions as previously shown in Chapter 3. Mixing has previously been shown to enhance mass transport for both diffusion and heat transfer. There have been several examples that enhance mass transport in a membrane or fluid surface interface system. Those examples include the use of sinusoidal hollow fibers, and implementations of the HBM for heat transfer and a gas-fluid interface. Luelf et al. developed a custom extrusion method for making hollow fiber membranes for dialysis applications with varied extrusion diameters through phase inversion.[62] Repeating hollow fiber diameter sinusoidal variations of 1.0 mm to 1.1 mm, and 0.9 to 1.2 mm were compared to a 1.0 mm diameter fiber with approximate oxygen fluxes (mmol/m^2h) of 8 and 15 vs. 4, respectively. The differences in fluid flow path allowed for a 3x increase in flux vs. a standard continuous diameter hollow fiber. Zhang et al. simulated herringbone-like structures referred to as transverse vortex generators to enhance heat transfer in ANSYS FLUENT (a finite difference method numerical simulation software similar to COMSOL).[63] While the paper discussed the changes in heat transfer for different geometries; there was no comparison given with a groove-less channel.

Marschewski et al. used different herringbone and herringbone inspired geometries to study the effects of heat transfer at $Re \geq 190$ ($\gg Re \cong 1$ for this research).[64] Both linear channels of different depths and three separate herringbone-type structures were fabricated and characterized. Heat transfer in terms of flux was increased by 220% vs. the linear channel at the same Re. Finally, Femmer et al. used an array of herringbone mixers in contact with a gas permeable membrane to enhance the transfer of oxygen into the channel fluid. The device was tested at Re of 1, 2.3, and 10 quantifying oxygen transfer in a mg/min flux and compared to a linear channel-based geometry. Increasing Re showed increased oxygen transfer for both the herringbone and linear channel devices with the difference in oxygen transfer increasing by 10%

to 66% at Re = 1 and 10, respectively. After reviewing the paper, it is suspected that the flux increase at higher Re was due to higher mass recovery from more fluid with lower oxygen concentration coming in contact with the membrane surface. The process was likely limited by an air-liquid partition coefficient (K_H), Henry's law constant, not discussed in the paper. The diffusion coefficient of oxygen in air and water is 0.357 cm^2/s and 0.210 cm^2/s, respectively.[19,20] Oxygen has a K_H = 769 atm/M, or 1 mmol/L of oxygen in water at steady-state.

4.4 Herringbone Model Description

The practical guide published by Williams et al. was used as the basis for the HB model in this research.[59] As originally depicted in 3D (Figure 4.4), the HBM model was designed according to the geometry as defined in Figure 4.7. A standard HBM model half-cycle (Figure 4.7 A and B) was described as a 1.7 mm long channel (H_c and L_c) that was 410 µm wide (w_c) and 70 µm in total depth ($t_c + t_g$). The channel depth t_c was 20 µm and groove depth t_g was 50 µm. The channel length L_c could be varied by additional H_c segments. A single groove g was spaced by the groove index g_i of 145 µm from the center of one groove to the next. The groove offset g_o was typically alternated between 1/3 to 2/3 of the channel width w_c for every subsequent half-cycle. The design shown added a membrane of thickness t_m (50 µm) to match all previous simulations that held all membrane properties constant for comparison purposes. The design deviated by not alternating the groove offset g_o and having a continuous stream of grooves along the length of the channel. This decision was reached as the original HB design was made to mix two inlet fluids on a chip. This was advantageous as the shifting of g_o causes the fluid from one side of the channel to shift to the other for every subsequent half-cycle. In this research, the goal was to increase the concentration gradient at the membrane surface by pulling diffusing analyte away via the induced vortex flow. Alternating g_0 would create a gap with no grooves and any channel surface area without grooves would create a region without rotational flow next to the membrane. Accordingly, grooves were continuous with a single g_o value for all of L_c, The total groove count is defined as $floor(L_c/g_i) - 2$; where $floor()$ is a rounding function and allows for grooves to populate the full length of the channel without extending past the channel outlet. Setting L_c to 20.4 mm gave 138 total grooves for two ~10 mm inlet and outlet lengths when applying grooves to the LL models from Chapter 3.

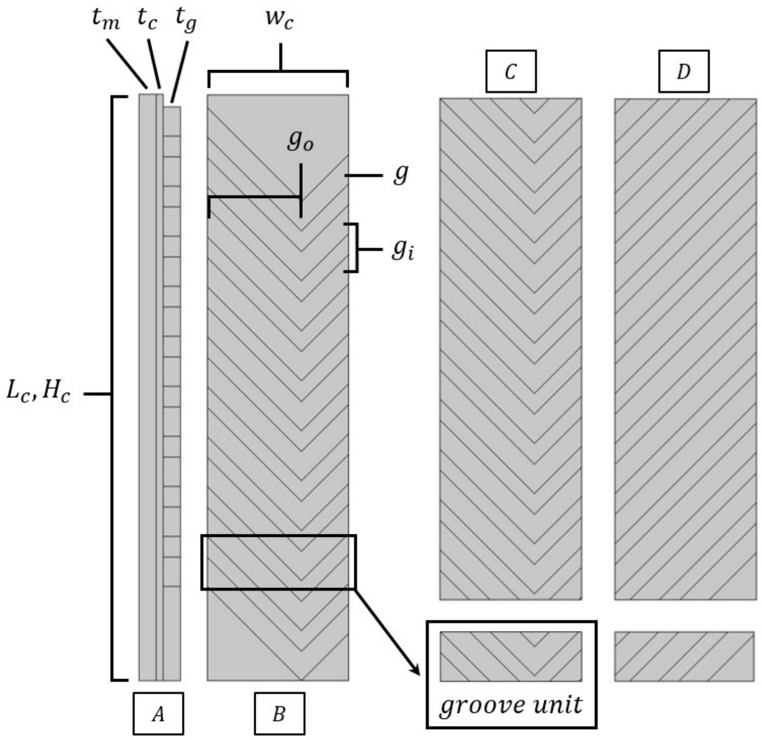

Figure 4.7. Herringbone half-cycle and single groove model.

In Figure 4.7, panels C and D show a further modified half-cycle model that was reduced to 145 μm channel length sections (equal to g_i) known as the single groove unit model (SGM). Part D also introduced a model with g_0 = 0 to form a fully diagonal groove from one wall to another. The reasons for the development of the SGM based model will be discussed in Section 4.5.

4.5 Herringbone and Linear Channel Mesh Quality Comparison

Mesh quality was compared for five mesh sizes to quantify the impact of mesh density (also referred to as resolution or quality) on RR. COMSOL comes with predefined mesh quality settings that geometry and physics dependent but go from an extremely coarse (low mesh density) to extremely fine (high mesh density). There is also the option of defining your mesh manually very specifically at different edges, boundaries, and domains to include element sizes, geometry types, and growth changes in geometry sizes over an interval). Comparing different mesh qualities is important due to the continuous folding of fluid and reduced diffusion distances as discussed in Section 4.1 as particle tracking is not applicable. Mesh densities for simulated COMSOL presets and custom meshes are given in Table 4.1.

Table 4.1. Mesh element count for different channel geometries.

		Linear Channel, Depth (μm)			
Mesh	HBM*	20	49.3	50	70
Coarse	163708	76799	69771	69887	64722
Normal	310602	139029	132362	131748	120503
Fine	821757	369557	340889	339819	316326
Extremely Fine	11196119	5854019	5650674	5617629	5442936
Custom 2	9532435	3548075	599786	583335	308195

*Herringbone Mixer (HBM)

For this research, all models were limited to one SGM due to computational resource limitations. The computer used to simulate this research used an Intel i7-6820HQ Quad-Core CPU with hyper threading and a base clock of 2.7 GHz. The system had 64 GB of DDR4 memory with approximately 60 GB available for simulations after basic Windows 10 resources were allocated. As mentioned in Section 2.5.2, the memory requirements increased quadratically with mesh density. So, if it was possible to simulate the model using a predefined coarse or coarser mesh, then it was advantageous in both time to computer and lower computational resource requirements. For example, using the highest mesh density simulated (custom mesh 2), simulating an SGM for seven different flow rates took 7 hours and 31 minutes; while the coarse mesh took 14 minutes 31 seconds. Figure 4.8 gives the RR at 0.5 μL/min for coarse, normal, fine, custom, and custom 2 meshes.

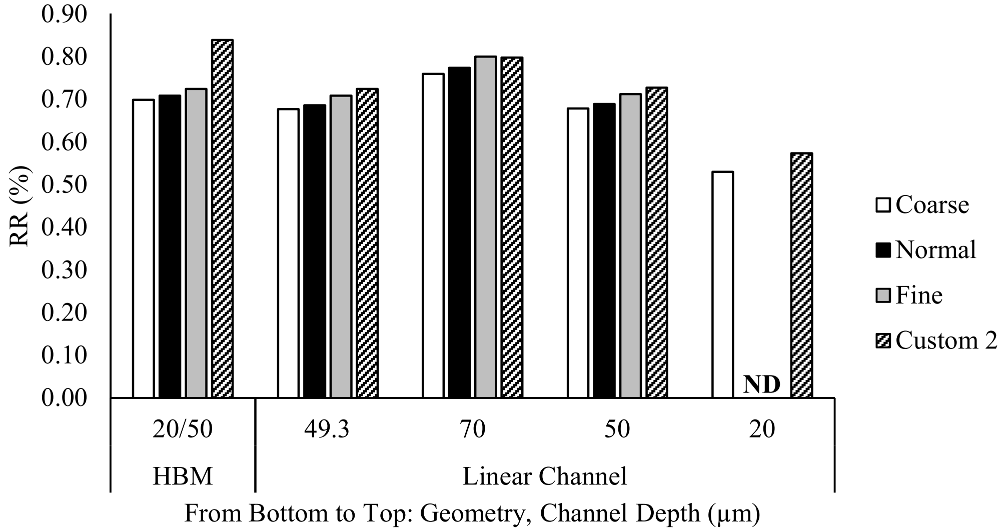

Figure 4.8. Single groove model mesh comparison of RR at Q = 0.5 μL/min.

The custom meshes were iterations based on visually inspecting the default mesh. The HBM model showed a 14% relative difference in RR compared to the fine mesh. In comparison, the 49.3 μm, 70 μm, and 50 μm channels showed a maximum of 3% relative difference in RR. The 20 μm channel did not simulate with anything but the lowest quality (coarse) mesh and the custom 2 mesh. This was due to the high aspect ratio of the channel (7% relative difference) which required a higher mesh density to properly resolve the parabolic velocity gradient. The 20 µm channel failed to simulate at the normal and fine mesh settings.

A custom mesh was developed, and the settings were used for all models unless specified. The mesh physics was defined as fluid dynamics and modified. All default mesh properties were deleted and replaced with a free tetrahedral mesh of extremely fine quality. This mesh was then modified to have a minimum and maximum element size of $t_c/20$ and $t_c/10$, respectively. For the HBM model, the maximum element size was 2 µm This was done as leaving the default automatic settings would result in mesh densities decreasing parabolically across the width and depth of the channel to match the expected laminar flow profile assumed due to the physics settings.

The goal of the custom meshes was to remove the parabolic profile and increase mesh density, but not exceed the computational resources available. Figure 4.9 shows the difference between the extremely fine and the custom 2 mesh in an HBM channel groove at the device inlet. The extremely fine mesh had triangular elements that increased in size towards the center of the channel (top mesh). The custom 2 mesh (bottom mesh) did not do this due to the minimum and maximum element size restrictions previously stated. The parabolic profile would normally be acceptable without rotational and folding flow, but there was the problem of mesh resolution vs. concentration gradient as previously shown in Figure 4.6. Increasing the mesh element size toward the center of the channel would yield inaccurate results due to the fluid folding and increasing the concentration gradient between each subsequent fold. Table 4.1 gives the sum of all elements for the different geometries and corresponding mesh sizes simulated for RR in Figure 4.8. The extremely fine mesh element count is given, but no simulations were done using this mesh due to increasing mesh element size toward the center of the channel where the fluid was being folded into would result in inaccurate results. The extremely fine mesh also includes a corner refinement setting that increased mesh density at the channel walls where it was not needed and increased simulation time and complexity.

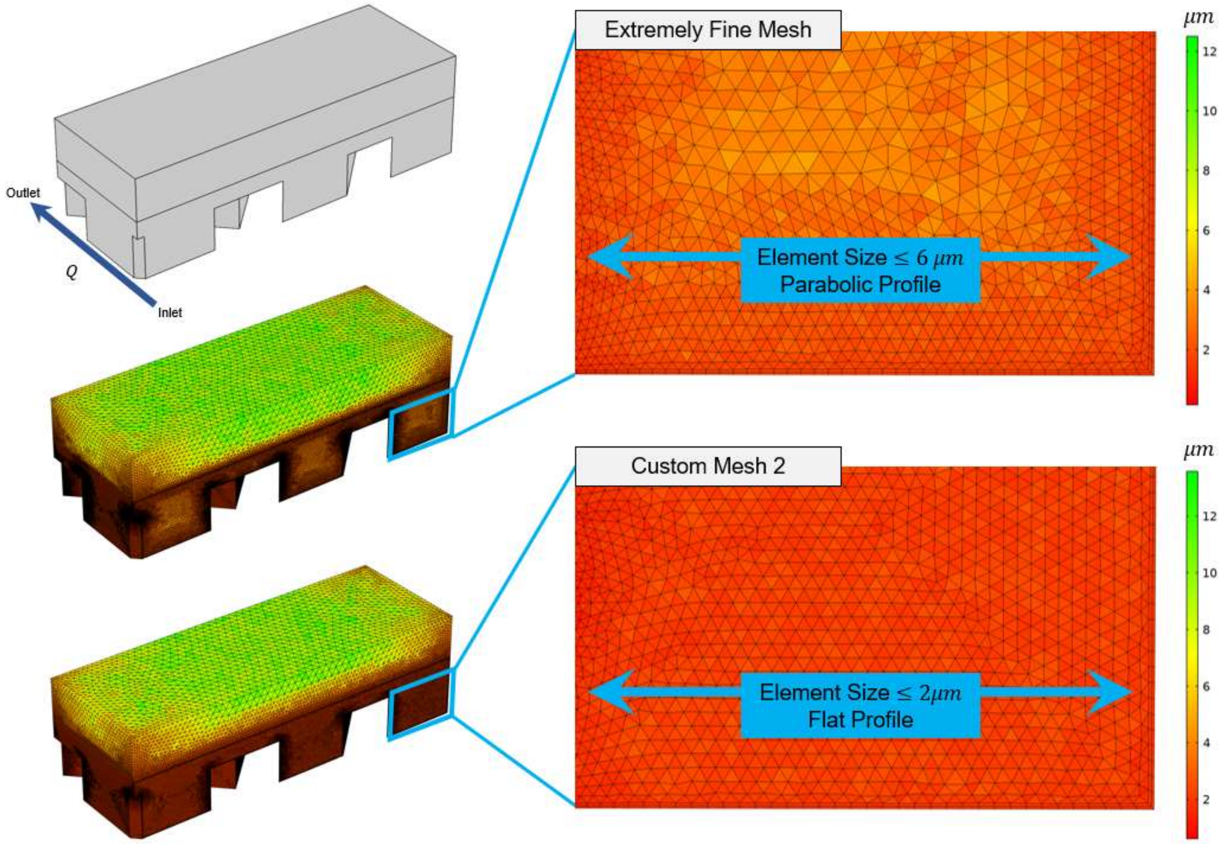

Figure 4.9. Mesh density plot comparison for extremely fine mesh and custom mesh 2.

4.6 Herringbone Single Groove Unit Model

The HBM model was simplified from a single half-cycle to a single groove unit model (SGM) consisting of a single HBM groove in distance (145 μm channel length), but with an inlet offset of ~273 μm ($2/3 \cdot w_c$) so that in inlet and outlet cross-sectional dimensions were mirror images. The SGM geometry was chosen as it uses the same groove area as a single groove, and was repeatable along L_c without any channel area under the membrane going without a groove structure (Figure 4.7 C). All linear channels (LC) followed the same SGM structure with 145 µm channel length units as a limitation for comparison purposes. All models were limited by computational resources as discussed in Section 4.5.

Initially, two SGM models based on inlet boundary conditions of average linear velocity U and flow rate Q were developed to observe the difference in RR. The models included HBM geometry with 20 µm channel depth and 50 µm groove depth along LCs with depths of 20, 50, and 70 µm. Starting with the average linear velocity of fluid in a CMA 20 lumen (U = 0.109 mm/s), velocities were parametrically swept as fractions of U (1/4, 2/4, 3/4, 1, 2, 3, and 4) to determine RR (Figure 4.10).

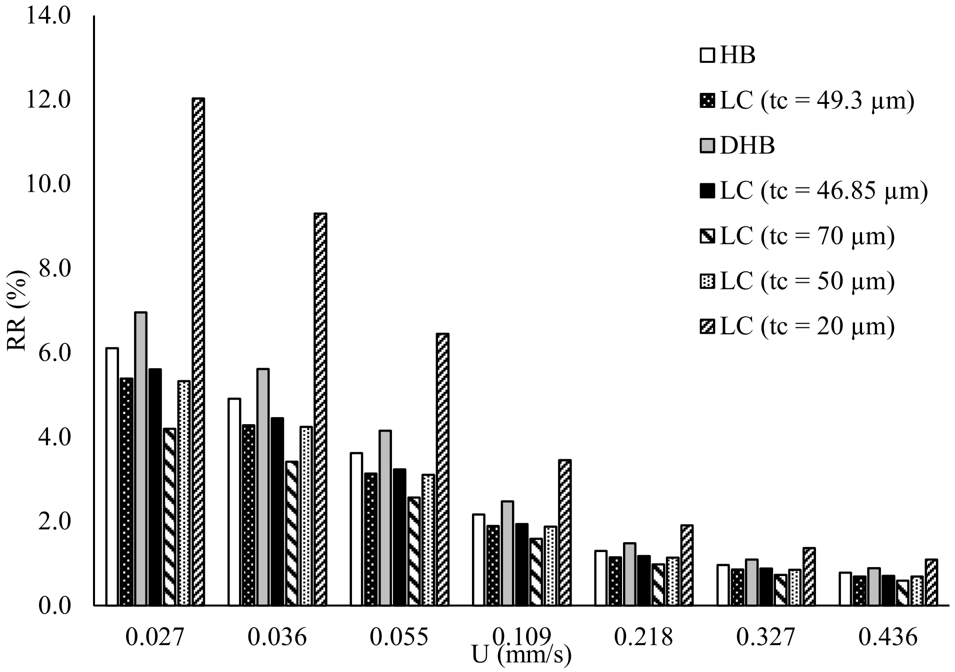

Figure 4.10. FITC-10 RR% vs. U for different microfluidic microdialysis geometries.

When a constant inlet U was set, the 20 μm LC gave the highest RR of 12.04% at U = 0.027 mm/s as expected since the small channel depth gave a shorter characteristic diffusion length. The short diffusion length allowed the fluid to reach equilibrium with the sample medium in less time and, therefore, increased RR. In comparison, the HBM geometry resulted in 6.15% RR with a varied 20 μm to 50 μm channel depth due to the channel floor grooves. The mixing effect could not compete with shorter diffusion lengths and longer residence times at the same linear velocities. However, it could compete at different average linear velocities when a constant inlet flow rate was set (Figure 4.11).

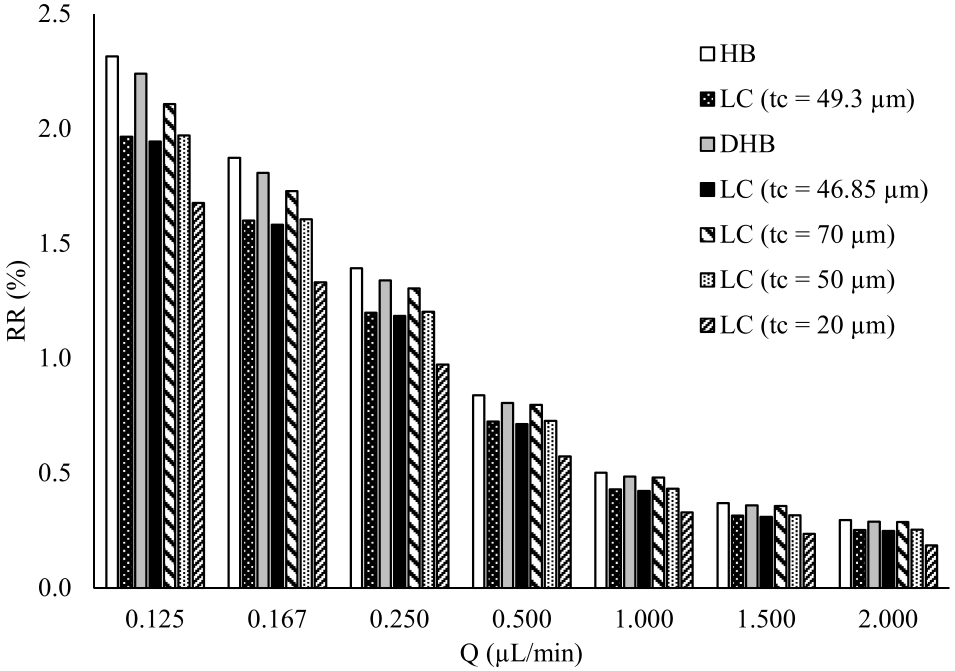

Figure 4.11. FITC-10 $RR\%$ vs. Q for different microfluidic microdialysis geometries..

That being said, Figure 4.10 highlights that it is important to understand whether or not RR was increasing due to shorter diffusion lengths at (holding U constant), or due to the mixing effect of the HBM geometry. This was due to the fact that the 20 μm LC gave the highest RR at constant inlet U, and the HBM geometry contained varied 20 µm to 70 µm depth segments. The constant inlet U model showed the expected trend of decreased diffusion distance equals higher RR.

When looking at the 20 µm LC and HBM, there was a problem of determining whether the RR increased from the mixing effects of HBM geometry, or due to the periodically decreased diffusion distance from 70 µm to 20 µm. To solve this problem, an additional model was created with equal channel volume to the HB geometry with a channel depth of 49.3 µm. Equalizing the volume between the HBM and the 49.3 µm LC model allowed for the average characteristic diffusion length between the HBM and LC models to be the same. This removed the effects of volume differences between each channel causing differences in diffusion lengths. The 49.3 µm LC depth had equal total diffusion lengths as a 20 µm channel and 50 µm grooves. So, if the fluid flow was volumetric, it would have the same residence time in the channel and should yield the same RR. In other words, keeping all things equal (channel volume, diffusion lengths, and membrane surface area/geometry) would allow for the same RR barring differences in fluid flow affecting the CBL.

Figure 4.10 and Figure 4.11 both show that RR for the HBM geometry was relatively higher than the 49.3 µm LC at all simulated U and Q by up to 18%. The relative difference in RR remained at $16.9\% \pm 0.7\%$ for all flow rates (Figure 4.11); while the absolute difference in RR decreased from 0.27% to 0.04% from Q = 0.125 to 2.0 µL/min. This showed that the normal flow vector collapsed the CBL at higher flow rates to the point where the change due to mixing became negligible. Completely collapsing the CBL sets C_1 = 0 in Equation 4.1 and maximizes flux. Further verification that the RR increase was due to mixing is shown by the concentration gradient slice plots in Figure 4.12, Figure 4.13, and Figure 4.14 for flow rates of Q = 0.125, 0.5, and 2.0 μL/min. Each plot contains 10 slices of the concentration gradient in perpendicular to the normal flow vector in showing the effects of tangential flows.

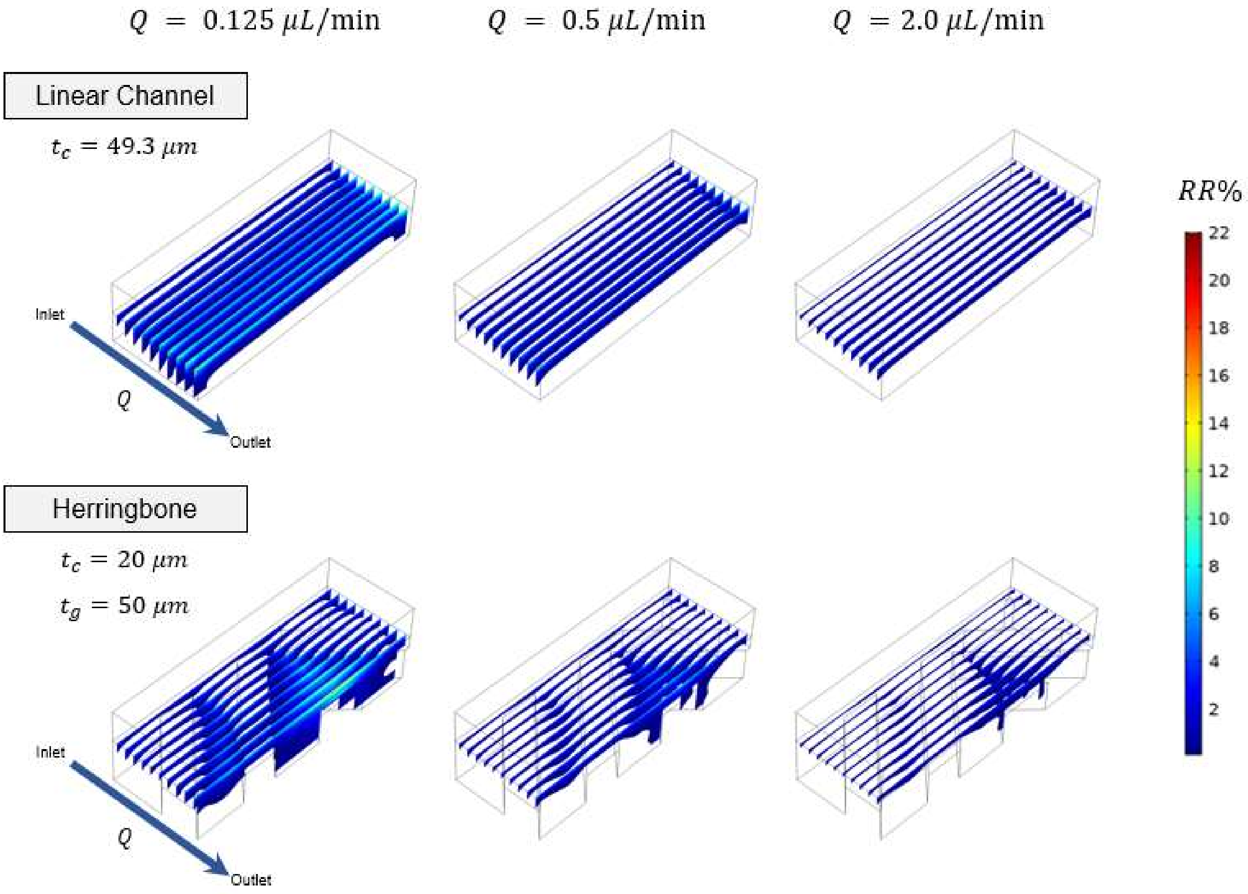

Figure 4.12. Herringbone and linear channel groove unit concentration gradients across 10 slices perpendicular to flow.

All figures are normalized from 0 to 22% RR for comparison. The graphed concentration gradients are limited in COMSOL by a slice filter that only plots concentration greater that 0.1% RR and only within the channel geometry. The membrane concentration gradient is not plotted in order to better visualize the effects of fluid flow on analyte diffusion in the channel. The plots effectively show the CBL as fluid moves through the channel with each subsequent slice from inlet to outlet. The HBM clearly shows the sweeping of analyte into the grooves in comparison with the volume equivalent LC (t_c = 49.3 µm).

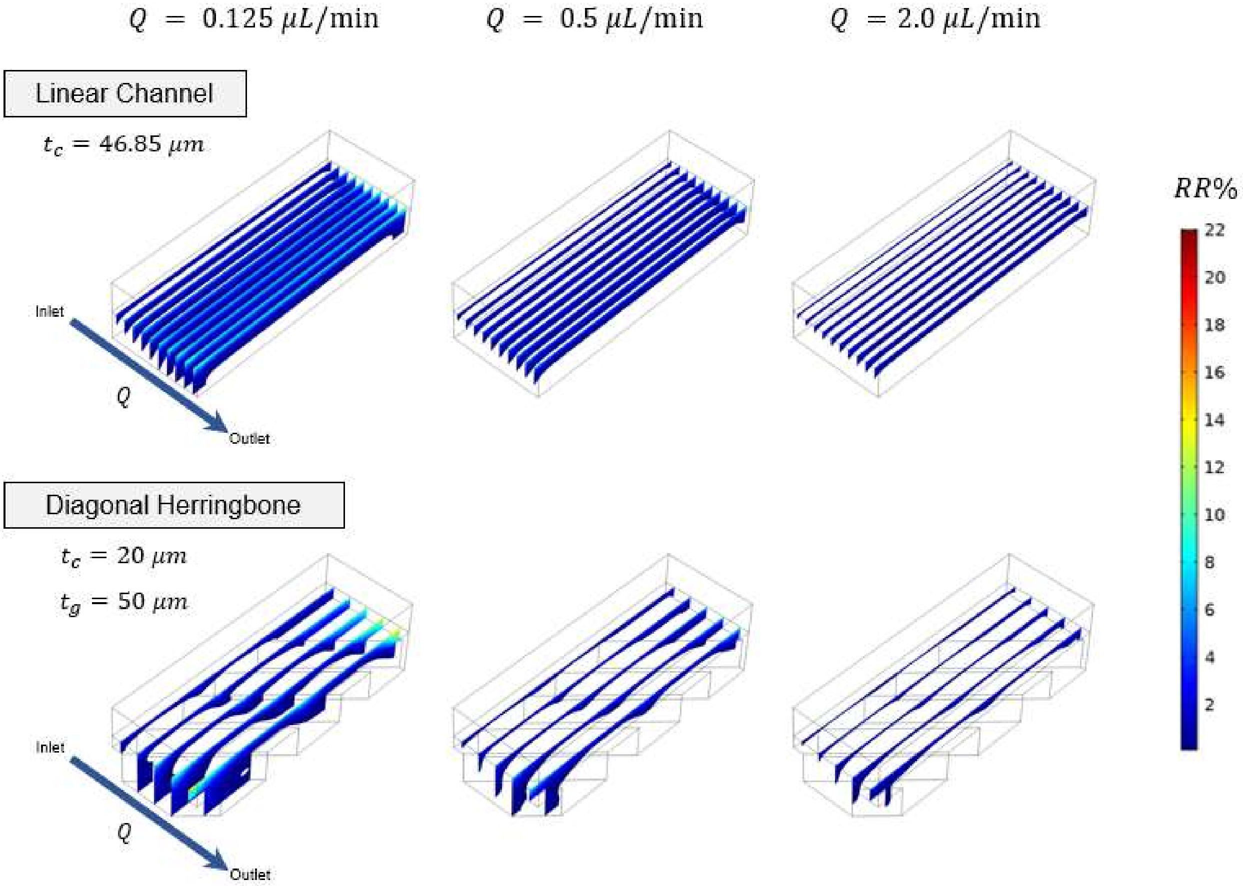

Figure 4.13. Diagonal herringbone and linear channel groove unit concentration gradients across 10 slices perpendicular to flow.

4.7 Conclusion

The focus of this chapter was to improve upon the length scale and diffusion vector limitations presented as membrane perimeter to fluid cross-sectional area ratio in Chapter 3. Previously, it was found that maximizing this ratio is needed to maximize RR. This improvement presented in this chapter was the implementation of microfluidic mixing in the channel fluid next to the membrane surface. An introduction to mixing on the basis of the Baker's transformation was described (Section 4.1) following by the introduction of the herringbone micromixer geometry and its functionality (Section 4.1).

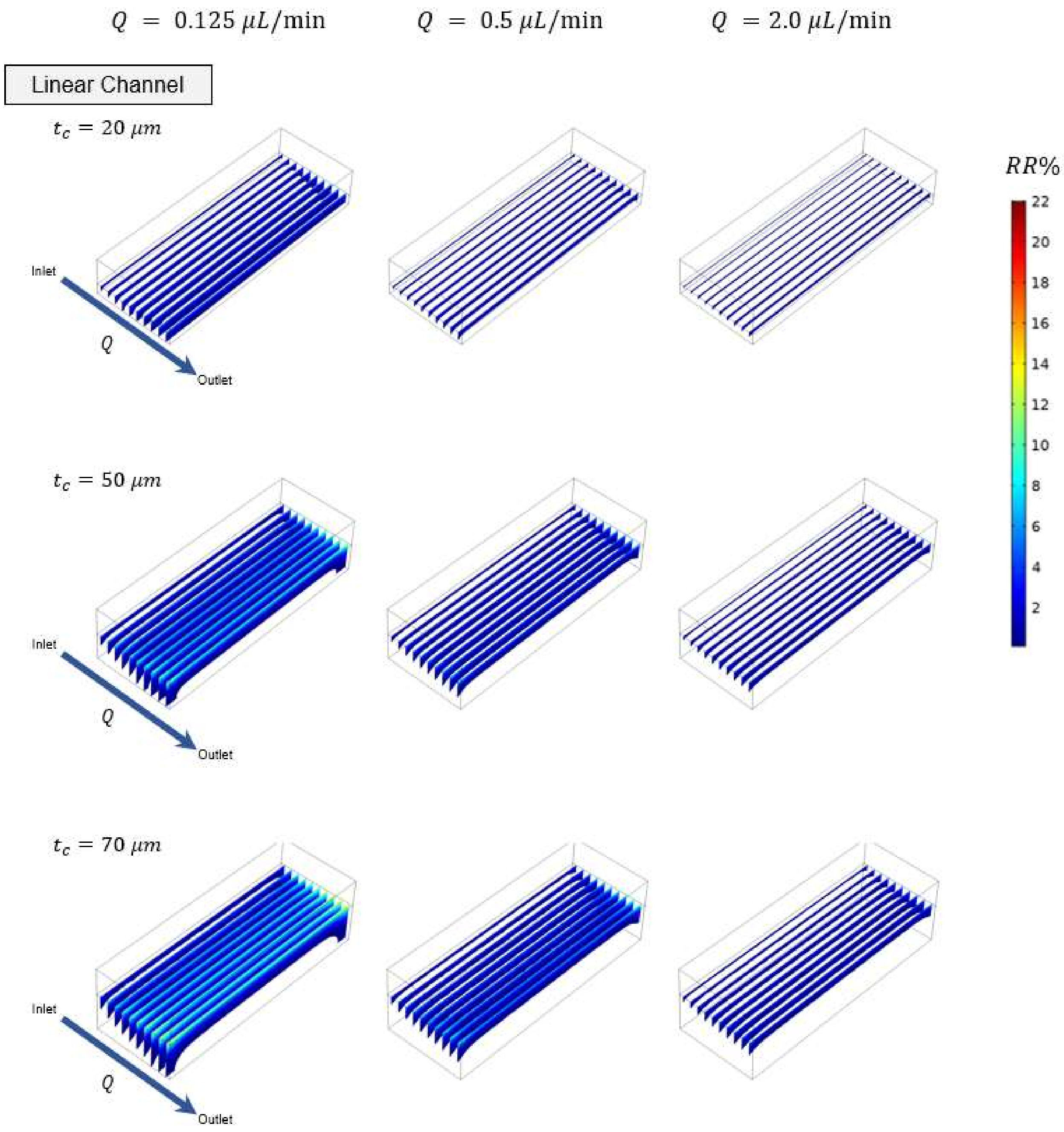

Figure 4.14. Linear channel groove unit concentration gradients across 10 slices perpendicular to flow.

Examples of herringbone mixer implementations were given (Section 4.3). A microfluidic microdialysis herringbone mixer model was developed and described as the single-groove model (Section 4.4). The importance of mesh density for proper simulation of diffusion in fluid with chaotic fluid flow vectors was described and simulated (Section 4.5). The single groove unit model with a 0.145 μm channel length and over 9 million mesh elements with a maximum 2 μm in size were simulated and compared to different linear channel depths (Section 4.6). A volume equivalent model was presented for comparison with the herringbone geometry to ensure that RR increases were due to the effects of mixing and not differences in diffusion lengths. It was shown that single groove model herringbone geometry is capable of shifting the concentration boundary layer for increased diffusive transport. This resulted in a 16.9 ± 0.7% RR for 7 flow rates from 0.125 to 2.0 μL/min vs. the volume equivalent linear channel. This improvement in RR shows that microfluidic mixing is an excellent tool for altering diffusive length scales and bypassing the limitations discussed previously in Chapter 3. Further research into how effective this geometry at longer channel lengths is required. Different geometries such as ultra-wide channels, but shorter channel lengths can be investigated to keep the mixing advantage.

Chapter 5. Conclusions and Future Work

This work has shown that COMSOL is a powerful tool for predicting RR from a device geometry standpoint. COMSOL provides the ability to model commercial CMA 20 devices and transfer that model to novel microfluidic channel-based geometries in the effort to improve device performance in terms of RR. COMSOL allows the user to visualize and quantify the physics on a gradient level not observable in benchtop experiments.

Linear looped microfluidic microdialysis devices were designed and simulated to exceed the CMA 20 device RR while only using 67% of the total fluid cross-sectional area, and 105% of the membrane-fluid interface. Key concepts relating to the membrane perimeter and fluid cross-sectional area ratio were developed. The effect of overlapping diffusion lengths as this ratio increases was simulated and quantified. A full understanding of how reducing structural components not contributing to analyte diffusion or fluid flow and increasing membrane surface area to fluid volume ratio is key for maximizing overlapping diffusion lengths and subsequently RR. A linear looped device was fabricated and characterized for small molecule recovery (caffeine and vitamin B-12). The device used an in-house fabricated membrane. The membrane did not give comparable RR to the CMA 20 devices and further research is needed into optimizing the fabrication of membranes for use on microfluidic microdialysis devices. Specifically, there needs to be improvements to the analyte membrane diffusivity without the membrane exhibiting fluid loss during collection as observed with commercial membranes.

Microfluidic mixing was investigated toward improving RR beyond the limits placed by surface area to volume ratio, characteristic diffusion lengths, diffusivities, and fluid velocities. A linear channel microdialysis model was developed to include herringbone grooves. These grooves allow the fluid to rotate and fold concentration gradients over repeatedly developing what is called a Baker's transformation. This folding of fluid adds additional flow vectors not typical of low $Re \leq 10$ laminar flows. The fluid vectors pull fluid containing analyte diffusion away from the membrane increasing the concentration gradient at the membrane surface and maximizing flux without increasing flow rate or fluid linear velocity down the channel. It was shown an ~18% relative improvement in RR is possible over a 145 μm long channel. The absolute difference in RR was shown to decrease at higher flow rate due to the effect of the normal flow vector collapsing the concentration boundary layer and minimizing the flux increases due to fluid folding.

Future work includes the fabrication and optimization of polyethersylfone membranes for use on fabricated linear looped devices with and without herringbone grooves. Different membrane polymers and fabrication methods can be researched and tested.

COMSOL is a powerful tool that can decrease time for design iterations by cutting down on fabrication cycles that can be time consuming. It can take up to a week waiting for new soft-lithography photo masks and greater than 20 hours to fabricate a group of test devices prior to characterization and comparison with simulated results. The ability to scale the model and use 3D printing fabrication techniques is advantageous. Printing a single device takes less than 30 minutes bringing down the design to test time considerably. 3D printing is already well documented for use in microfluidics across multiple papers.[65–83] Each year new advances bring 3D printing closer to the microfluidic length scales. Recently in 2017, the Nordin group demonstrated a custom stereolithography 3D printer and resin formulation for fabricating 18 μm by 20 μm channels.[78] Such a printer would be sufficient for continuing this work without the time consuming clean room fabrication steps.

References

(1) Kehr, J. Handbook of Microdialysis - Methods, Applications and Perspectives. *Handb. Behav. Neurosci.* **2006**, *16* (06), 111–129. https://doi.org/10.1016/S1569-7339(06)16007-5.

(2) Stenken, J. A. Methods and Issues in Microdialysis Calibration. *Anal. Chim. Acta* **1999**, *379* (3), 337–358. https://doi.org/10.1016/S0003-2670(98)00598-4.

(3) Bungay, P. M.; Morrison, P. F.; Dedrick, R. L. Steady-State Theory for Quantitative Microdialysis of Solutes and Water in Vivo and in Vitro. *Life Sci.* **1990**, *46* (2), 105–119. https://doi.org/10.1016/0024-3205(90)90043-Q.

(4) Bungay, P. M.; Morrison, P. F.; Dedrick, R. L. Steady-State Theory for Quantitative Microdialysis of Solutes and Water in Vivo and in Vitro. *Life Sci.* **1990**, *46* (2), 105–119. https://doi.org/10.1016/0024-3205(90)90043-Q.

(5) Stenken, J. A.; Poschenrieder, A. J. Bioanalytical Chemistry of Cytokines – A Review. *Anal. Chim. Acta* **2015**, *853* (1), 95–115. https://doi.org/10.1016/j.aca.2014.10.009.

(6) Muramatsu, T.; Muramatsu, H. Glycosaminoglycan-Binding Cytokines as Tumor Markers. *Proteomics* **2008**, *8* (16), 3350–3359. https://doi.org/10.1002/pmic.200800042.

(7) Bottenus, D.; Jubery, T. Z.; Ouyang, Y.; Dong, W.-J.; Dutta, P.; Ivory, C. F. 10 000-Fold Concentration Increase of the Biomarker Cardiac Troponin I in a Reducing Union Microfluidic Chip Using Cationic Isotachophoresis. *Lab Chip* **2011**, *11* (5), 890. https://doi.org/10.1039/c0lc00490a.

(8) Rosenfeld, T.; Bercovici, M. 1000-Fold Sample Focusing on Paper-Based Microfluidic Devices. *Lab Chip* **2014**, *14* (23), 4465–4474. https://doi.org/10.1039/C4LC00734D.

(9) Larsson, C. I. The Use of an “Internal Standard” for Control of the Recovery in Microdialysis. *Life Sci.* **1991**, *49* (13), PL73–PL78. https://doi.org/10.1016/0024-3205(91)90082-M.

(10) Mou, X.; Lennartz, M. R.; Loegering, D. J.; Stenken, J. A. Modulation of the Foreign Body Reaction for Implants in the Subcutaneous Space: Microdialysis Probes as Localized Drug Delivery/Sampling Devices. *J. Diabetes Sci. Technol.* **2011**, *5* (3), 619–631.

(11) Duo, J.; Fletcher, H.; Stenken, J. A. Natural and Synthetic Affinity Agents as Microdialysis Sampling Mass Transport Enhancers: Current Progress and Future Perspectives. *Biosens. Bioelectron.* **2006**, *22* (3), 449–457. https://doi.org/10.1016/j.bios.2006.05.004.

(12) Duo, J.; Stenken, J. A. In Vitro and in Vivo Affinity Microdialysis Sampling of Cytokines Using Heparin-Immobilized Microspheres. *Anal. Bioanal. Chem.* **2011**, *399* (2), 783–793. https://doi.org/10.1007/s00216-010-4333-0.

(13) Ao, X.; Sellati, T. J.; Stenken, J. A. Enhanced Microdialysis Relative Recovery of

Inflammatory Cytokines Using Antibody-Coated Microspheres Analyzed by Flow Cytometry. *Anal. Chem.* **2004**, *76* (13), 3777–3784. https://doi.org/10.1021/ac035536s.

(14) Khramov, a N.; Stenken, J. a. Enhanced Microdialysis Recovery of Some Tricyclic Antidepressants and Structurally Related Drugs by Cyclodextrin-Mediated Transport. *Analyst* **1999**, *124* (7), 1027–1033. https://doi.org/10.1039/a901236b.

(15) Phillips, S. J.; Stenken, J. A. In Situ Inner Lumen Attachment of Heparin to Poly(Ether Sulfone) Hollow Fiber Membranes Used for Microdialysis Sampling. *Anal. Chem.* **2018**, *90* (8), 4955–4960. https://doi.org/10.1021/acs.analchem.7b03927.

(16) Kottegoda, S.; Shaik, I.; Shippy, S. A. Demonstration of Low Flow Push Á Pull Perfusion. **2002**, *121*, 93–101.

(17) Cabay, M. R.; McRay, A.; Featherstone, D. E.; Shippy, S. A. Development of M-Low-Flow-Push−Pull Perfusion Probes for Ex Vivo Sampling from Mouse Hippocampal Tissue Slices. https://doi.org/10.1021/acschemneuro.7b00277.

(18) Lee, W. H.; Slaney, T. R.; Hower, R. W.; Kennedy, R. T. Microfabricated Sampling Probes for in Vivo Monitoring of Neurotransmitters. *Anal. Chem.* **2013**, *85* (8), 3828–3831. https://doi.org/10.1021/ac400579x.

(19) Deen, W. M. *Analysis of Transport Phenomena*, 1st ed.; Oxford University Press: New York, 1998. p. 245.

(20) Cussler, E. L. *Diffusion: Mass Transfer in Fluid Systems*, 3rd ed.; Cambridge University Press: Cambridge, New York, 2009. p. 598.

(21) Bird, R. B.; Stewart, W. E.; Lightfoot, E. N. *Transport Phenomena*, 2nd ed.; Wiley: New York, 1960. p. 41.

(22) Manz, A.; Graber, N.; Widmer, H. M. Miniaturized Total Chemical Analysis Systems: A Novel Concept for Chemical Sensing. *Sensors Actuators B. Chem.* **1990**, *1* (1–6), 244–248. https://doi.org/10.1016/0925-4005(90)80209-I.

(23) Mark, D.; Haeberle, S.; Roth, G.; von Stetten, F.; Zengerle, R. Microfluidic Lab-on-a-Chip Platforms: Requirements, Characteristics and Applications. *Chem. Soc. Rev.* **2010**, *39* (3), 1153. https://doi.org/10.1039/b820557b.

(24) Sackmann, E. K.; Fulton, A. L.; Beebe, D. J. The Present and Future Role of Microfluidics in Biomedical Research. *Nature*. 2014. https://doi.org/10.1038/nature13118.

(25) Whitesides, G. M. The Origins and the Future of Microfluidics. *Nature*. July 27, 2006, pp 368–373. https://doi.org/10.1016/j.agee.2012.07.026.

(26) Lalia, B. S.; Kochkodan, V.; Hashaikeh, R.; Hilal, N. A Review on Membrane Fabrication: Structure, Properties and Performance Relationship. *Desalination* **2013**, *326*, 77–95. https://doi.org/10.1016/j.desal.2013.06.016.

(27) Desai, S. P.; Freeman, D. M.; Voldman, J. Plastic Masters-Rigid Templates for Soft Lithography. *Lab Chip* **2009**, *9* (11), 1631–1637. https://doi.org/10.1039/b822081f.

(28) Abdelgawad, M.; Watson, M. W. L.; Young, E. W. K.; Mudrik, J. M.; Ungrin, M. D.;

Wheeler, A. R. Soft Lithography: Masters on Demand. *Lab Chip* **2008**, *8* (8), 1379. https://doi.org/10.1039/b804050h.

(29) Kim, P.; Kwon, K. W.; Park, M. C.; Lee, S. H.; Kim, S. M. Soft Lithography for Microfluidics : A Review. **2008**, *2* (1), 1–11.

(30) Wiggins, S.; Ottino, J. M. Foundations of Chaotic Mixing. *Philos. Trans. A. Math. Phys. Eng. Sci.* **2004**, *362* (1818), 937–970. https://doi.org/10.1098/rsta.2003.1356.

(31) Lee, C. Y.; Chang, C. L.; Wang, Y. N.; Fu, L. M. Microfluidic Mixing: A Review. *Int. J. Mol. Sci.* **2011**, *12* (5), 3263–3287. https://doi.org/10.3390/ijms12053263.

(32) Suh, Y. K.; Kang, S. A Review on Mixing in Microfluidics. *Micromachines* **2010**, *1* (3), 82–111. https://doi.org/10.3390/mi1030082.

(33) Lee, C. Y.; Wang, W. T.; Liu, C. C.; Fu, L. M. Passive Mixers in Microfluidic Systems: A Review. *Chem. Eng. J.* **2016**, *288*, 146–160. https://doi.org/10.1016/j.cej.2015.10.122.

(34) Kee, S. P.; Gavriilidis, A. Design and Characterisation of the Staggered Herringbone Mixer. *Chem. Eng. J.* **2008**, *142* (1), 109–121. https://doi.org/10.1016/j.cej.2008.02.001.

(35) Kim, C. K.; Yoon, J. Y. Optimal Design of Groove Shape on Passive Micromixer Using Design of Experiment Technique. *Proc. Inst. Mech. Eng. Part E J. Process Mech. Eng.* **2017**, *231* (4), 880–887. https://doi.org/10.1177/0954408916640663.

(36) Kwak, T. J.; Nam, Y. G.; Najera, M. A.; Lee, S. W.; Strickler, J. R.; Chang, W.-J. Convex Grooves in Staggered Herringbone Mixer Improve Mixing Efficiency of Laminar Flow in Microchannel. *PLoS One* **2016**, *11* (11), e0166068. https://doi.org/10.1371/journal.pone.0166068.

(37) Du, Y.; Zhang, Z.; Yim, C.; Lin, M.; Cao, X. Evaluation of Floor-Grooved Micromixers Using Concentration-Channel Length Profiles. *Micromachines* **2010**, *1* (1), 19–33. https://doi.org/10.3390/mi1010019.

(38) Wang, D.; Ba, D.; Liu, K.; Hao, M.; Gao, Y.; Wu, Z.; Mei, Q. A Numerical Research of Herringbone Passive Mixer at Low Reynold Number Regime. *Micromachines* **2017**, *8* (11), 325. https://doi.org/10.3390/mi8110325.

(39) Application Builder - COMSOL Multiphysics 5.1 https://www.comsol.com/release/5.1/application-builder (accessed Feb 26, 2018).

(40) Niesner, R.; Heintz, A. Diffusion Coefficients of Aromatics in Aqueous Solution. *J. Chem. Eng. Data* **2000**, *45* (6), 1121–1124. https://doi.org/10.1021/je0000569.

(41) Miyabe, K.; Isogai, R. Estimation of Molecular Diffusivity in Liquid Phase Systems by the Wilke–Chang Equation. *J. Chromatogr. A* **2011**, *1218* (38), 6639–6645. https://doi.org/10.1016/J.CHROMA.2011.07.018.

(42) Snyder, K. L.; Nathan, C. E.; Yee, A.; Stenken, J. a. Diffusion and Calibration Properties of Microdialysis Sampling Membranes in Biological Media. *Analyst* **2001**, *126* (8), 1261–1268. https://doi.org/10.1039/b102488b.

(43) Ao, X.; Stenken, J. A. Microdialysis Sampling of Cytokines. *Methods* **2006**, *38* (4), 331–

341. https://doi.org/10.1016/j.ymeth.2005.11.012.

(44) Arrio-Dupont, M.; Cribier, S.; Foucault, G.; Devaux, P. F.; D ’albis, A. Diffusion of Fluorescently Labeled Macromolecules in Cultured Muscle Cells. *Biophys. J.* **1996**, *70*, 2327–2332. https://doi.org/10.1016/S0006-3495(96)79798-9.

(45) Ross, A. E.; Pompano, R. R. Diffusion of Cytokines in Live Lymph Node Tissue Using Microfluidic Integrated Optical Imaging. *Anal. Chim. Acta* **2018**, *1000*, 205–213. https://doi.org/10.1016/J.ACA.2017.11.048.

(46) Cabrera, R. E. Development of Microdialysis Probes in Series Approach Toward Eliminating Microdialysis Sampling Calibration: Miniaturization into a PDMS Microfluidic Device, University of Arkansas, Fayetteville, 2018. pp. 75-113.

(47) Fabrice Schlegel. Understanding Stabilization Methods | COMSOL Blog https://www.comsol.com/blogs/understanding-stabilization-methods/ (accessed May 1, 2018).

(48) Walter Fei. How Much Memory Is Needed to Solve Large COMSOL Models? | COMSOL Blog https://www.comsol.com/blogs/much-memory-needed-solve-large-comsol-models/ (accessed Feb 26, 2018).

(49) Zhang, J.; Yan, S.; Yuan, D.; Alici, G.; Nguyen, N.-T.; Ebrahimi Warkiani, M.; Li, W. Fundamentals and Applications of Inertial Microfluidics: A Review. *Lab Chip* **2016**, *16* (1), 10–34. https://doi.org/10.1039/C5LC01159K.

(50) Song, Y.; Cheng, D.; Zhao, L. Microfluidics: Fundamental, Devices and Applications . Wiley-VCH : Weinheim, Germany 2018. p. 377.

(51) SU-8 3000 Permanent Epoxy http://www.microchem.com/pdf/SU-8 3000 Data Sheet.pdf (accessed Jan 6, 2016).

(52) Aran, K.; Sasso, L. A.; Kamdar, N.; Zahn, J. D. Irreversible, Direct Bonding of Nanoporous Polymer Membranes to PDMS or Glass Microdevices. **2015**, *33* (4), 395–401. https://doi.org/10.1038/nbt.3121.ChIP-nexus.

(53) Lee, C.-Y.; Fu, L.-M. Recent Advances and Applications of Micromixers. *Sensors Actuators B Chem.* **2018**, *259*, 677–702. https://doi.org/10.1016/j.snb.2017.12.034.

(54) Stroock, A. D.; Dertinger, S. K.; Whitesides, G. M.; Ajdari, A. Patterning Flows Using Grooved Surfaces. *Anal. Chem.* **2002**, *74* (20), 5306–5312. https://doi.org/10.1021/ac0257389.

(55) Stroock, A. D.; Dertinger, S. K. W.; Ajdari, A.; Mezic, I.; Stone, H. a; Whitesides, G. M. Chaotic Mixer for Microchannels. *Science* **2002**, *295* (2002), 647–651. https://doi.org/10.1126/science.1066238.

(56) Bennett, J.; Wiggins, C. A Computational Study of Mixing Microchannel Flows. *arXiv* **2003**, 3–7.

(57) Stroock, A. D.; McGraw, G. J. Investigation of the Staggered Herringbone Mixer with a Simple Analytical Model. *Philos. Trans. R. Soc. London A Math. Phys. Eng. Sci.* **2004**,

362 (1818), 971–986. https://doi.org/10.1098/rsta.2003.1357.

(58) Hassell, D. G.; Zimmerman, W. B. Investigation of the Convective Motion through a Staggered Herringbone Micromixer at Low Reynolds Number Flow. *Chem. Eng. Sci.* **2006**, *61* (9), 2977–2985. https://doi.org/10.1016/j.ces.2005.10.068.

(59) Williams, M. S.; Longmuir, K. J.; Yager, P. A Practical Guide to the Staggered Herringbone Mixer. *Lab Chip* **2008**. https://doi.org/10.1039/b802562b.

(60) Du, Y.; Zhang, Z.; Yim, C.; Lin, M.; Cao, X. A Simplified Design of the Staggered Herringbone Micromixer for Practical Applications. *Biomicrofluidics* **2010**, *4* (2), 1–13. https://doi.org/10.1063/1.3427240.

(61) Tóth, E.; Holczer, E.; Iván, K.; Fürjes, P. Optimized Simulation and Validation of Particle Advection in Asymmetric Staggered Herringbone Type Micromixers. *Micromachines* **2014**, *6* (1), 136–150. https://doi.org/10.3390/mi6010136.

(62) Luelf, T.; Tepper, M.; Breisig, H.; Wessling, M. Sinusoidal Shaped Hollow Fibers for Enhanced Mass Transfer. *J. Memb. Sci.* **2017**, *533*, 302–308. https://doi.org/10.1016/j.memsci.2017.03.030.

(63) Zhang, J. F.; Joshi, Y. K.; Tao, W. Q. Single Phase Laminar Flow and Heat Transfer Characteristics of Microgaps with Longitudinal Vortex Generator Array. *Int. J. Heat Mass Transf.* **2017**, *111*, 484–494. https://doi.org/10.1016/j.ijheatmasstransfer.2017.03.036.

(64) Marschewski, J.; Brechbühler, R.; Jung, S.; Ruch, P.; Michel, B.; Poulikakos, D. Significant Heat Transfer Enhancement in Microchannels with Herringbone-Inspired Microstructures. *Int. J. Heat Mass Transf.* **2016**, *95*, 755–764. https://doi.org/10.1016/j.ijheatmasstransfer.2015.12.039.

(65) Saggiomo, V.; Velders, A. H. Simple 3D Printed Scaffold-Removal Method for the Fabrication of Intricate Microfluidic Devices. *Adv. Sci.* **2015**, *2* (9), 1500125. https://doi.org/10.1002/advs.201500125.

(66) Belka, M.; Ulenberg, S.; Bączek, T. Fused Deposition Modeling Enables the Low-Cost Fabrication of Porous, Customized-Shape Sorbents for Small-Molecule Extraction. *Anal. Chem.* **2017**, *89* (8), 4373–4376. https://doi.org/10.1021/acs.analchem.6b04390.

(67) Comina, G.; Suska, A.; Filippini, D. PDMS Lab-on-a-Chip Fabrication Using 3D Printed Templates. *Lab Chip* **2014**, *14* (2), 424–430. https://doi.org/10.1039/c3lc50956g.

(68) Kang, K.; Oh, S.; Yi, H.; Han, S.; Hwang, Y. Fabrication of Truly 3D Microfluidic Channel Using 3D-Printed Soluble Mold. *Biomicrofluidics* **2018**, *12* (1), 014105. https://doi.org/10.1063/1.5012548.

(69) Bhattacharjee, N.; Urrios, A.; Kang, S.; Folch, A. The Upcoming 3D-Printing Revolution in Microfluidics. *Lab Chip* **2016**, *16* (10), 1720–1742. https://doi.org/10.1039/c6lc00163g.

(70) Kitson, P. J.; Rosnes, M. H.; Sans, V.; Dragone, V.; Cronin, L. Configurable 3D-Printed Millifluidic and Microfluidic "lab on a Chip" Reactionware Devices. *Lab Chip* **2012**, *12* (18), 3267–3271. https://doi.org/10.1039/c2lc40761b.

(71) Chen, C.; Mehl, B. T.; Munshi, A. S.; Townsend, A. D.; Spence, D. M.; Martin, R. S. 3D-Printed Microfluidic Devices: Fabrication, Advantages and Limitations - a Mini Review. *Anal. Methods* **2016**, *8* (31), 6005–6012. https://doi.org/10.1039/c6ay01671e.

(72) Gaal, G.; Mendes, M.; de Almeida, T. P.; Piazzetta, M. H. O.; Gobbi, Â. L.; Riul, A.; Rodrigues, V. Simplified Fabrication of Integrated Microfluidic Devices Using Fused Deposition Modeling 3D Printing. *Sensors Actuators, B Chem.* **2017**, *242*, 35–40. https://doi.org/10.1016/j.snb.2016.10.110.

(73) Salentijn, G. I. J.; Oomen, P. E.; Grajewski, M.; Verpoorte, E. Fused Deposition Modeling 3D Printing for (Bio)Analytical Device Fabrication: Procedures, Materials, and Applications. *Anal. Chem.* **2017**, *89* (13), 7053–7061. https://doi.org/10.1021/acs.analchem.7b00828.

(74) Bertana, V.; Potrich, C.; Scordo, G.; Scaltrito, L.; Ferrero, S.; Lamberti, A.; Perrucci, F.; Pirri, C. F.; Pederzolli, C.; Cocuzza, M.; et al. 3D-Printed Microfluidics on Thin Poly(Methyl Methacrylate) Substrates for Genetic Applications. *J. Vac. Sci. Technol. B, Nanotechnol. Microelectron. Mater. Process. Meas. Phenom.* **2017**, *36* (1), 01A106. https://doi.org/10.1116/1.5003203.

(75) Rimington, R. P.; Capel, A. J.; Christie, S. D. R.; Lewis, M. P. Biocompatible 3D Printed Polymers: Via Fused Deposition Modelling Direct C2C12 Cellular Phenotype in Vitro. *Lab Chip* **2017**, *17* (17), 2982–2993. https://doi.org/10.1039/c7lc00577f.

(76) Kong, D. S.; Thorsen, T. A.; Babb, J.; Wick, S. T.; Gam, J. J.; Weiss, R.; Carr, P. A. Open-Source, Community-Driven Microfluidics with Metafluidics. *Nature Biotechnology*. 2017, pp 523–529. https://doi.org/10.1038/nbt.3873.

(77) Tsai, H. Y.; Huang, A.; soesanto, J. F.; Luo, Y. L.; Hsu, T. Y.; Chen, C. H.; Hwang, K. J.; Ho, C. D.; Tung, K. L. 3D Printing Design of Turbulence Promoters in a Cross-Flow Microfiltration System for Fine Particles Removal. *J. Memb. Sci.* **2019**, *573*, 647–656. https://doi.org/10.1016/j.memsci.2018.11.081.

(78) Gong, H.; Bickham, B. P.; Woolley, A. T.; Nordin, G. P. Custom 3D Printer and Resin for 18 Mm × 20 Mm Microfluidic Flow Channels. *Lab Chip* **2017**, *17* (17), 2899–2909. https://doi.org/10.1039/c7lc00644f.

(79) Duong, L. H.; Chen, P.-C. Simple and Low-Cost Production of Hybrid 3D-Printed Microfluidic Devices. *Biomicrofluidics* **2019**, *13* (2), 024108. https://doi.org/10.1063/1.5092529.

(80) Anderson, K. B.; Lockwood, S. Y.; Martin, R. S.; Spence, D. M. A 3D Printed Fluidic Device That Enables Integrated Features. *Anal. Chem.* **2013**, *85* (12), 5622–5626. https://doi.org/10.1021/ac4009594.

(81) Hwang, Y.; Paydar, O. H.; Candler, R. N. 3D Printed Molds for Non-Planar PDMS Microfluidic Channels. *Sensors Actuators, A Phys.* **2015**, *226*, 137–142. https://doi.org/10.1016/j.sna.2015.02.028.

(82) Rogers, C. I.; Qaderi, K.; Woolley, A. T.; Nordin, G. P. 3D Printed Microfluidic Devices with Integrated Valves. *Biomicrofluidics* **2015**, *9* (1), 016501.

https://doi.org/10.1063/1.4905840.

(83) Chan, H. N.; Chen, Y.; Shu, Y.; Chen, Y.; Tian, Q.; Wu, H. Direct, One-Step Molding of 3D-Printed Structures for Convenient Fabrication of Truly 3D PDMS Microfluidic Chips. *Microfluid. Nanofluidics* **2015**, *19* (1), 9–18. https://doi.org/10.1007/s10404-014-1542-4.

Appendix A. Description of Research for Popular Publication

There is a tremendous interest in understanding and controlling the human immune system and subsequent inflammatory response. Many, if not all diseases have some form of inflammatory response involved and understanding this response could be key to treating the disease successfully. There is a specific signaling class of proteins linked to inflammatory response known as cytokines. These cytokines exist in extremely small concentrations and do not exist at all times. These signaling proteins help coordinate the body's immune system whenever there are events such as bacterial and viral infections, injury, or even autoimmune diseases where the body attacks itself. It is important to be able to know when, where, and how many signaling proteins exist when one of these events occurs. Doing so will save many lives and billions of dollars in medical expenses.

Microdialysis, a sampling method, can be used to collect these cytokines for study in a lab. Microdialysis is non-destructive to the cytokine, and minimally-invasive to the sampling site such as tissue. This means microdialysis can collect cytokines directly from the site of the disease state of interest such as near a bacterial infection. Microdialysis collection is driven by diffusion of the cytokine from outside of the microdialysis probe through a membrane to the inside where a fluid carries the protein away for analysis. Diffusion is limited by how long it takes the cytokine to move through the sample space, membrane, and internal fluid. This time period directly affects how many cytokines can be collected.

This research focuses on improving the design of a microdialysis device by using microfluidics. Microfluidics is a field where fluid channels similar in size to a computer chip are fabricated for different scientific uses that are limited in fluid volume such as microdialysis.

Currently, microdialysis is limited to the commercially available cylindrical designs. These designs have not changed in over 35 years. Microfluidics presents the opportunity to implement specialized fluid mixing geometries in the microchannels of a microdialysis device that will help the diffusing cytokine move faster through the internal fluid and increase the number of cytokines collected in a period of time. Increasing the number of cytokines collected and the rate at which they are collected will allow for scientists to further the understanding of different disease states to save money and more importantly lives.

Appendix B. Executive Summary of Newly Created Intellectual Property

The following new intellectual property was created: method of increasing diffusive transport in microfluidic microdialysis devices.

Appendix C. Potential Patent and Commercialization Aspects of Listed Intellectual Property Items

C.1. Patentability of Intellectual Property

In the future, a final device design could be patented, but the current geometry is free to use by all.

C.2. Commercialization Prospects

New microfluidic microdialysis devices can be produced with increased mass transport and sold to individuals in the biomedical or research fields interested in increasing the quantity of molecules collects in a given time.

C.3. Possible Prior Disclosure of IP

None.

Appendix D. Broader Impact of Research

D.1. Applicability of Research Method to Other Problems.

Research fields where diffusion is limited will benefit from the method of increased mass transfer developed in this research. It has already been shown that the device geometry in this research can be used to increase heat transfer. This research has shown how it can be used to improve diffusive transport as well. This research can be applied toward other fields of study which require the non-destructive collection of different molecules. This research also presents a way of thinking about different gradients that can be applied to other diffusion limited problems.

D.2. Impact of Research on U.S. and Global Society.

The microfluidic microdialysis device geometry shown in this research can be used to improve the understanding of different disease states in the human body by improving the microdialysis sampling process. Understanding these disease states will help develop new treatments and improve the quality of human life along with decrease medical expenses that number in the trillions of dollars per year in the United States alone.

D.3. Impact of Research Results on the Environment.

COMSOL simulations of microdialysis devices decrease the research waste by lowering the amount of time and resources used in the fabrication and testing said devices. The simulations can also predict future experimental outcomes and reduce the number of experiments needed to achieve a research goal.

Appendix E. Microsoft Project for MS MicroEP Degree Plan

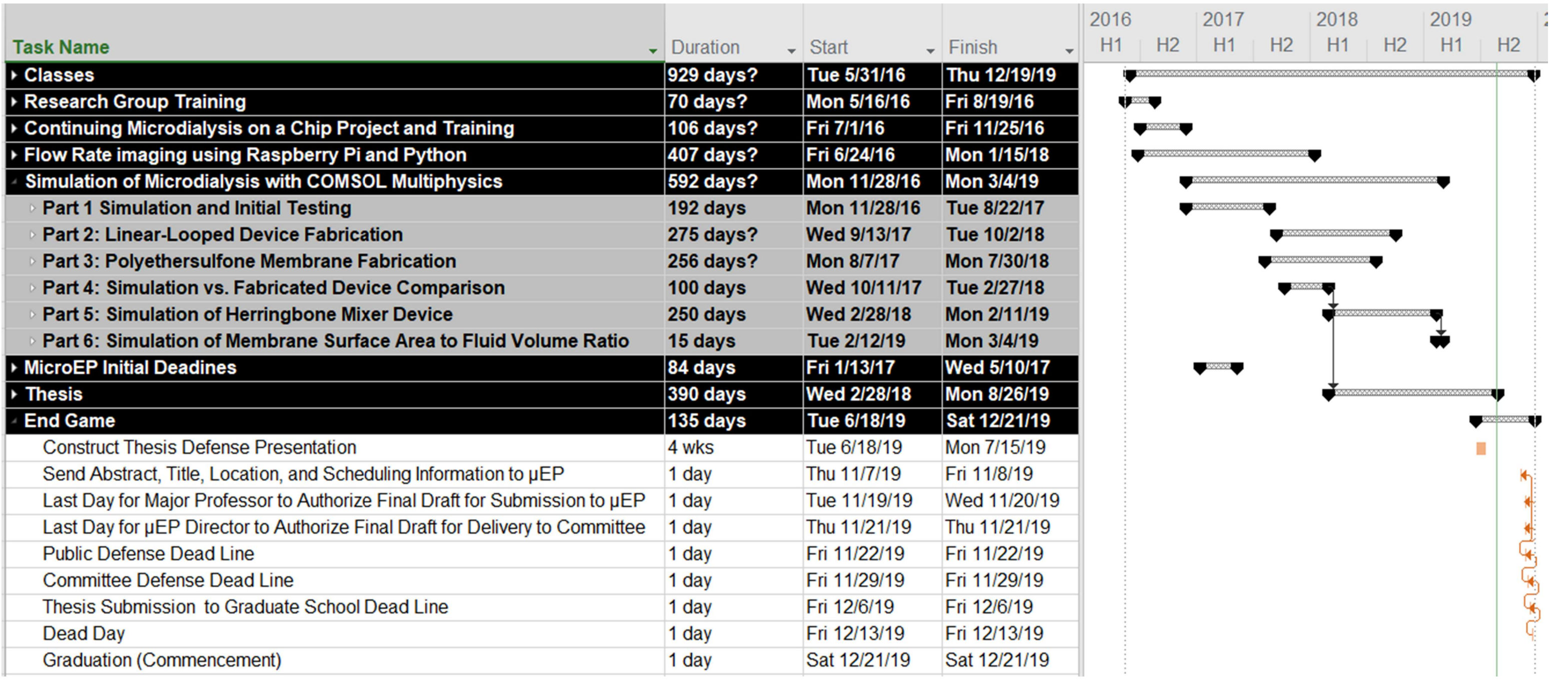

Task Name	Duration	Start	Finish
Classes	**929 days?**	**Tue 5/31/16**	**Thu 12/19/19**
Research Group Training	**70 days?**	**Mon 5/16/16**	**Fri 8/19/16**
Continuing Microdialysis on a Chip Project and Training	**106 days?**	**Fri 7/1/16**	**Fri 11/25/16**
Flow Rate imaging using Raspberry Pi and Python	**407 days?**	**Fri 6/24/16**	**Mon 1/15/18**
Simulation of Microdialysis with COMSOL Multiphysics	**592 days?**	**Mon 11/28/16**	**Mon 3/4/19**
Part 1 Simulation and Initial Testing	**192 days**	**Mon 11/28/16**	**Tue 8/22/17**
Part 2: Linear-Looped Device Fabrication	**275 days?**	**Wed 9/13/17**	**Tue 10/2/18**
Part 3: Polyethersulfone Membrane Fabrication	**256 days?**	**Mon 8/7/17**	**Mon 7/30/18**
Part 4: Simulation vs. Fabricated Device Comparison	**100 days**	**Wed 10/11/17**	**Tue 2/27/18**
Part 5: Simulation of Herringbone Mixer Device	**250 days**	**Wed 2/28/18**	**Mon 2/11/19**
Part 6: Simulation of Membrane Surface Area to Fluid Volume Ratio	**15 days**	**Tue 2/12/19**	**Mon 3/4/19**
MicroEP Initial Deadines	**84 days**	**Fri 1/13/17**	**Wed 5/10/17**
Thesis	**390 days**	**Wed 2/28/18**	**Mon 8/26/19**
End Game	**135 days**	**Tue 6/18/19**	**Sat 12/21/19**
Construct Thesis Defense Presentation	4 wks	Tue 6/18/19	Mon 7/15/19
Send Abstract, Title, Location, and Scheduling Information to µEP	1 day	Thu 11/7/19	Fri 11/8/19
Last Day for Major Professor to Authorize Final Draft for Submission to µEP	1 day	Tue 11/19/19	Wed 11/20/19
Last Day for µEP Director to Authorize Final Draft for Delivery to Committee	1 day	Thu 11/21/19	Thu 11/21/19
Public Defense Dead Line	1 day	Fri 11/22/19	Fri 11/22/19
Committee Defense Dead Line	1 day	Fri 11/29/19	Fri 11/29/19
Thesis Submission to Graduate School Dead Line	1 day	Fri 12/6/19	Fri 12/6/19
Dead Day	1 day	Fri 12/13/19	Fri 12/13/19
Graduation (Commencement)	1 day	Sat 12/21/19	Sat 12/21/19

Appendix F. Identification of All Software Used in Research

Computer #1:

Model: Dell Precision 15 7510 Laptop
Windows Product ID: 00329-00000-00003-AA726
Location: Mobile and CHBC 204/206
Owner: Stenken Lab, University of Arkansas

Computer #2:

Model: Dell OptiPlex 7040 MT Desktop
Windows Product ID: 00329-00000-00003-AA407
Location: Mobile and CHBC 204/206
Owner: Stenken Lab, University of Arkansas

Computer #3:

Model: Home built Windows PC
Windows Product ID: Not Available
Location: Personal
Owner: Patrick M. Pysz

Software #1:

Name: Microsoft Office 365
Purchased by: Patrick M. Pysz

Software #2:

Name: Matlab R2017a
Purchased by: University of Arkansas

Software #3:

Name: COMSOL 5.4
Purchased by: Stenken Lab, University of Arkansas

Software #4:

Name: Autodesk Fusion 360
Purchased by: University of Arkansas

Software #4:

Name: Autodesk AutoCAD 2018

Purchased by: University of Arkansas

Software #5:

Name: Simplify 3D 4.0

Purchased by: Patrick M. Pysz

Software #6:

Name: LinkCAD 9

Purchased by: Patrick M. Pysz

Appendix G. All Publications Published, Submitted, and Planned

Publications submitted and planned:

P.M. Pysz, R.E. Cabrera, J.A. Stenken. “Microdialysis Device Design Considerations.” submitted to RCS Analyst and is under review.

P.M. Pysz, J.A. Stenken. “FDM 3D Printed Microdialysis Devices.” is planned for submission to a yet undetermined journal.